Title
Attenuation and scattering structure in southern California and tidal triggering of earthquakes

Author
Wang, Wei

Publication Date
2019

UNIVERSITY OF CALIFORNIA SAN DIEGO

Attenuation and scattering structure in southern California and tidal triggering of earthquakes

A dissertation submitted in partial satisfaction of the
requirements for the degree
Doctor of Philosophy

in

Earth Sciences

by

Wei Wang

Committee in charge:

Professor Peter M. Shearer, Chair
Professor Adrian A. Borsa
Professor Joel P. Conte
Professor Jeffrey S. Gee
Professor Gabi Laske
Professor David T. Sandwell

2019

The dissertation of Wei Wang is approved, and it is acceptable in quality and form for publication on microfilm and electronically:

Chair

University of California San Diego

2019

DEDICATION

To my advisor Peter for his enlightenment on both my life and research.

To my parents Dilin and Xiaoyou for their love and support ever since I was born.

EPIGRAPH

"Good Good Study, Day Day Up." —Someone Unknown

TABLE OF CONTENTS

LIST OF FIGURES

LIST OF TABLES

ACKNOWLEDGEMENTS

First of all, I would like to own my sincere gratitude to my advisor and mentor Peter Shearer. His critical thinking, insight into science, and special sense to seismic data teach me to how to become a scientist. Peter always gives me freedom, encourages me to explore and allows me to make mistakes. Even if the results prove me wrong, he is always patient and supportive, and helps me solve problems. His door is always open, his responses to emails are always quick and efficient. He is open-minded and his suggestions and comments are always constructive. His skills in how to explain the complicate physics in a simple way and how to think of the geophysical problems in a big picture guide me the way to be a real scientist. The most valuable thing I learned from him is the concentration and enthusiasm in science. No matter how hard my PhD life is, he is always and always supportive. It is really a whole-life wealth to have you as my mentor and lead my love to science.

I thank my thesis committee members for their great mentorships and guidance through the last three years. I thank Gabi Laske also to be the committee member for my first-year study. She is rigorous to the geophysical problems and shared me a lot during an amazing cruise around San Diego Trough. Professor Adrian Borsa provides a lot of constructive suggestions to my research projects and helps me to improve my presentation and communication strategies. I thank Professor David Sandwell for introducing the geodesy to me. I also thank Professor Jeffery Gee, who taught me 'Marine Geology' and also brought his geological knowledges into every discussion. I own my gratitude to Professor Joel Conte for his kindly suggestions and comments. I am grateful to Professor Duncan Agnew and Yuri Fialko. Their constructive suggestions, open minds, and rigorous attitudes to science improve my understanding in geophysics from multiple disciplines. Collaboration with Debi Kilb and Frank Vernon improves my understanding of seismology, especially on strong ground motion and seismic instruments. Besides, it is my fortunate to part of IGPP. I own my sincere gratitude to all the professors and research scientists in IGPP and thank you all for your kindly support, I am really happy to meet you in IGPP and learn how to be a scientist and how to collaborate with the best scientists in the world. Special thanks are given to IGPP NetOps team and administrative staffs, many thanks to your patient help and support.

I would like to thank Professor Xiaofei Chen at Southern University of Science and Technology, who brought me into the seismology community. He kindly introduced seismology to me with great patience after the giant M7.9 Wenchuan earthquake in 2008 and guided my bachelor and master theses. My supervisor Professor Lianxing Wen brought me on the track of being a seismologist during my master degree study at University of Science and Technology of China (USTC). I thank Dr. Yuehua Zeng at USGS for his support, help and constructive discussion on the scattering topic during my PhD study. I would like to thank Dr. Tatsuhiko Saito and Professor Haruo Sato for offering a valuable of opportunity to visit National Research Institute for Earth Science and Disaster Resilience (NIED) in Japan to improve my understanding on strong ground motion and hazard prediction. Professor Chen Ji at UC Santa Barbara helps me a lot in understanding the physics of earthquake ruptures. Also, I appreciate Zachary Ross and Egil Hauksson at Caltech providing me with the support and discussion on the new techniques in seismology. At last, I would like to thank Professor Fang Huang at USTC for the one-decade friendship and continuous encouragement to me.

I appreciate the communication and collaboration with all the members of Peter's group, Janine Buehler, Nick Mancinelli, Songqiao (Shawn) Wei, Wenyuan Fan, Robin Matoza, Zhongwen Zhan, Daniel Trugman, Qiong Zhang, Marine Denolle, and Beineng Zhang, Xiaowei Chen. This great team is always helpful and open-minded. Especially, Professor Zhongwen Zhan at Caltech is always helpful and supportive to my academic career and life. He has been a great friend in my life and a smart guide in science since my bachelor at USTC for almost one decade.

Shawn, Daniel, and Wenyuan are great collaborators in life and science. Discussion with them benefits me a lot. I would like to thank my colleagues, Adrian Doran, Matthew Cook, Dara Goldberg, Jessie Saunders, John Desanto, Yongfei Wang, Laura Howell for the company and support since the hard-time first year. I also thank my office mates, Maggie Avery, Peter Kannberg, and Roz King and my friends in SIO, Xiaohua Xu, Zhao Chen, Kang Wang, Yuxiang Zhang, Qian Yao, Junle Jiang, Bin Cao, Yao Yu, Shunguo Wang, Michael Murphy, Xiaopeng Tong, Diego Melgar, Eric Lindsey, Katia Tymofyeyeva, Ignacio Sepulveda Oyarzun, Pieter Share, Zeyu Jin, etc. I appreciate Xiaoua Xu and Shunguo Wang offering kindly help on every discussion about science and comments to improve this thesis. Thank you, all my friend, for sharing the great and happy time at Scripps. Also, I would like to thank my friends outside Scripps, Zheng Xing, Yiyao Hu, Ke Ma, Chu Yu, Jiayuan Yao, Yi Hu, Dongdong Tian, Li Sun, Guanning Pang, etc.

Finally, I thank my dad Dilin, my mom Xiaoyou for your love.

Chapter 2, in full, is a reprint of the material as it appears in Journal of Geophysical Research: Solid Earth: Wang W. and Shearer P., 2015., “No clear evidence for localized tidal periodicities in earthquakes in the central Japan region”, *Journal of Geophysical Research: Solid Earth*, 120 (9), 6317-6328. The dissertation author is the primary investigator and author of this paper.

Chapter 3, in full, is currently under review for publication as Wang, W., Shearer P., and Xu X., “The spatial dislocation of tidal triggering and remote triggering at the Coso geothermal region”. The dissertation author was the primary investigator and author of the paper.

Chapter 4, in full, is a reprint of the material as it appears in Journal of Geophysical Research: Solid Earth: Wang W. and Shearer P., 2017, “Using direct and coda wave envelopes to resolve the scattering and intrinsic attenuation structure of Southern California", *Journal of Geophysical Research: Solid Earth*, 120(9), 7236-7251. The dissertation author is the primary investigator and author of this paper.

Chapter 5, in full, is a reprint of the material as it appears in Journal of Geophysical Research: Solid Earth: Wang W.and Shearer P., 2019, "An improved method to determine coda-Q, earthquake magnitude and site amplification: theory and application to southern California",*Journal of Geophysical Research: Solid Earth*, 124(1), 578-598. The dissertation author is the primary investigator and author of this paper.

Chapter 6, in full, is currently under revision for publication as Wang W.,Buehler J., Shearer P., Kilb D., and Vernon F., "Focal mechanism effects on S/P amplitude ratio in San Bernardino region, southern California". The dissertation author was the primary investigator and author of the paper.

VITA

Jul 30, 1988	Born, Tongling, Anhui, China
2006–2010	Bachelor of Science in Geophysics, University of Science and Technology of China, Hefei, China
2010–2013	Master of Science in Geophysics, University of Science and Technology of China, Hefei, China
2013-2019	Graduate Student Researcher, Scripps Institution of Oceanography, University of California San Diego, U.S.A.
2019	Doctor of Philosophy in Earth Sciences, Scripps Institution of Oceanography, University of California San Diego, U.S.A.

PUBLICATIONS

Wang W. and Shearer P., “A new station-based maximum likelihood algorithm to detect the clipped seismograms”, *in prep.*

Wang W. and Shearer P., “Limitation of multiple lapse time window approach (MLTWA) and case study in southern California”, *in prep.*

Wang W. and Shearer P., “Exploring the spectral converging coefficient spatial variation in southern California”, *to be submitted.*

Wang W. and Shearer P., “Spatial variation of stress drops of the aftershock sequences of M6.4 and M7.1 Ridgecrest Earthquakes”, *to be submitted.*

Wang, W., Shearer P., and Xu X., “The spatial decorrelation of tidal triggering and remote triggering at Coso geothermal region”, *to be submitted.*

Wang W., Buehler J., Shearer P., Kilb D., and Vernon F., “Focal mechanism effects on S/P amplitude ratio in San Bernardino region, southern California”, *submitted.*

Shearer P., Abercrombie R., Trugman D., **Wang W.**, “Comparing EGF Methods for Estimating Corner Frequency and Stress Drop from P-wave Spectra”, *Journal of Geophysical Research: Solid Earth*, doi: 10.1029/2018JB016957, 2019.

Wang W. and Shearer P., “An improved method to determine coda-Q, earthquake magnitude and site amplification: theory and application to southern California”, *Journal of Geophysical Research: Solid Earth*, 124(1), 578-598, 2019.

Wang W. and Shearer P., "Using direct and coda wave envelopes to resolve the scattering and intrinsic attenuation structure of Southern California", *Journal of Geophysical Research: Solid Earth*, 120(9), 7236-7251, 2017.

Wang W. and Shearer P., "No clear evidence for localized tidal periodicities in earthquakes in the central Japan region", *Journal of Geophysical Research: Solid Earth*, 120 (9), 6317-6328, 2015.

Huang F., Chen L., Wu Z., **Wang W.**, "First-principles investments of equilibrium Mg isotope fractionations in garnet,cpx,opx, andol: implications for Mg isotope thermometry", *Earth and Planetary Science Letters*, 367, pp. 61-70, 2013.

Dai, Z.*, **Wang, W.***, Wen, L., "Irregular topography at the Earth's inner core boundary", *Proceedings of the National Academy of Sciences*, 109(20), pp.7654-7658, 2012. (* equal contribution)

ABSTRACT OF THE DISSERTATION

Attenuation and scattering structure in southern California and tidal triggering of earthquakes

by

Wei Wang

Doctor of Philosophy in Earth Sciences

University of California San Diego, 2019

Professor Peter M. Shearer, Chair

In this dissertation, I study two fundamental topics in seismology, tidal triggering of earthquakes and attenuation and scattering structure. Studies of tidal triggering help constrain earthquake nucleation models and relate to earthquake predicability and forecasting. Resolving attenuation and scattering behavior can provide more physically realistic models for strong ground motion prediction equations (GMPEs) and improve our understanding of the physical properties of rocks in the lithosphere. Chapter 1 is an introduction, providing background and motivation for each of the following chapters. Chapters 2 & 3 focus on the topic of tidal triggering of earthquakes. Chapter 2 studies tidal triggering in the central Japan region using $M \geq 3$ earthquakes and finds no clear evidence for tidal triggering. Chapter 3 analyzes seismicity in the Coso region of California and finds strong tidal triggering but an absence of remote triggering at the Coso geothermal field, constraining earthquake triggering sensitivities at different time scales of stress perturbations. Chapters 4–6 study the inelastic properties of the crust and upper mantle in southern California using both coda and direct-wave observations. Chapter 4 stacks coda envelope functions across southern California and synthesizes them using a two-layer model, composed of a shallow crustal layer with strong wide-angle scattering and high P and S intrinsic attenuation and a deeper layer with weaker scattering and lower intrinsic attenuation. Chapter 5 describes improvements to the conventional coda-*Q* method to solve for coda attenuation, site amplification and source radiated energy simultaneously. Chapter 6 models focal-sphere-dependent S/P amplitudes assuming a whole-space intrinsic and scattering attenuation model around the San Bernardino region.

Chapter 1

Introduction

Earthquakes are one of Earth's most challenging natural hazards. Every year, there are an average of about 20 $M \geq 7$ earthquakes, including one great earthquake ($M \geq 8$). The unpredictable and abrupt release of energy by large earthquakes can cause many casualties and severe property damage. Studying earthquakes can provide important information on earthquake hazard prediction and strong ground motion estimation, as well as valuable data to probe Earth structure, including its internal constitution and dynamic properties.

1.1 Tidal Triggering of Earthquakes

Earth's tides are the distortions of Earth's shape caused by gravitational potential changes from external bodies, i.e., Sun, Moon, etc. This change of shape produces tidal stresses. Since the gravitational changes are related to the relative periodic motions between Earth and celestial bodies, the tidal stresses exhibit clear periodicities, i.e., semi-diurnal, diurnal, semi-monthly, etc. Among all the tidal-stress components, the semi-diurnal one has the maximum amplitude. Since the amplitude of these periodic (days to months) tidal stress variations is much higher than the buildup of long-term tectonic stress over the same time period, the tidal stress may trigger faults at a critical state. The continental crust is thought to be in a state of incipient failure (Zoback and Zoback, 2002) and the stress perturbation from Earth tides can potentially trigger ruptures (Gomberg et al., 1997; Hill and Prejean, 2007; Delorey et al., 2017). Studying tidal triggering of earthquakes can help us understand the earthquake nucleation process. However, it is not easy to observe direct tidal triggering of earthquakes and the question as to whether tidal stress can trigger earthquakes has been puzzling seismologists for over a century (Schuster, 1897). If we could observe tidal triggering of earthquakes, this could shed light on the earthquake initiation process and provide clues regarding earthquake forecasting and prediction.

Most of the convincing observations of tidal triggering occur near-shore and/or offshore (Tanaka et al., 2002a; Cochran et al., 2004; Scholz et al., 2019), where the ocean loading term (from the ocean tides) is much larger than the sold Earth tides. A robust statistical correlation between solid Earth tides and earthquake occurrence on the continent is hard to detect and requires a large and complete catalog (Métivier et al., 2009; Scholz et al., 2019). Consequently, increasing the detection ability for small events can improve the possibility to observe tidal triggering, as well as other kinds of triggering, i.e., remote triggering of earthquakes. In addition, triggering has been observed more in certain susceptible regions, i.e., geothermal fields or volcanic regions, likely owing to the role of fluids. Natural and/or anthropogenic fluid-related activities can efficiently change the stress state locally, such as increasing pore pressure, which can reduce the effective normal stress and promote seismicity. For this reason, geothermal fields and volcanic regions are ideal places to conduct triggering studies (Brodsky and Prejean, 2005; Peng et al., 2010; Aiken and Peng, 2014).

A key issue in seismology is whether the mechanisms of physical processes with different time scales can trigger the slips on faults. The tidal force acts as an intermediate-term process with a period of days to months. Besides the tidal triggering of earthquakes, there are two other commonly-observed triggering behaviors, i.e., static stress triggering and remote triggering. Static stress triggering is induced by permanent stress changes caused by large-earthquake ruptures and is often used to explain the occurrence of aftershock sequences near mainshock ruptures (King et al., 1994; Stein, 1999). Remote or dynamic stress triggering is caused by the passing seismic waves radiated by an earthquake (Gomberg et al., 1997; Hill and Prejean, 2007). The typical period of the dynamic triggering is seconds. These different types of triggering have been observed around the world (i.e., tidal triggering: Tanaka et al. (2002a); Cochran et al. (2004); Scholz et al. (2019); remote triggering: Gomberg et al. (1997); Brodsky and Prejean (2005); Hill and Prejean (2007); Peng et al. (2010); Aiken and Peng (2014)). Events at large distances from mainshocks are clearly dynamically triggered, but there is a debate regarding the relative importance of static versus dynamic triggering in generating aftershocks close to mainshocks (Brodsky and Prejean, 2005; Hill and Prejean, 2007). These kinds of observations can shed lights on discovering the physical mechanisms of the triggering.

1.2 Attenuation Structure of the Earth

The amplitude of ground motion can be described as the convolution of the source radiated energy, the ray path effect (i.e., Green's Function), and the site amplification term. The decrease of amplitude with distance depends on two factors, geometrical spreading and attenuation, both of which are involved in the Green's Function. The geometrical spreading term describes the decrease of seismic wave intensity with distance due to energy conservation, i.e., the area of the wavefront increases as it moves further from the source. Seismic attenuation describes the energy dissipation of seismic waves during wave propagation. Attenuation is caused by two factors: scattering attenuation (elastic attenuation) and intrinsic attenuation (anelastic attenuation). Intrinsic attenuation is caused by the energy transfer from the potential and kinetic energy to heat loss, which is not reversible. Scattering is caused by heterogeneity in the media, which changes the propagation direction of the wavefield, and/or transfers it into other seismic phases. Characterizing the intrinsic and scattering attenuation structure of the Earth is a fundamental problem in seismology.

Attenuation parameters are an important input for accurate strong ground motion estimation, especially at high frequencies ($>$ 1 Hz). In addition, resolving attenuation can improve our understanding of Earth's interior structure and physical properties because attenuation has different dependences on rock properties than seismic velocity. A significant difference between the behaviors of intrinsic attenuation and scattering attenuation is that the scattered wavefield only alters the propagation direction, rather than attenuates its energy. At local scales, the scattered energy becomes part of the coda wave (Aki and Chouet, 1975), which is the tail that follows direct arrivals in a seismogram. It is difficult to separate intrinsic and scattering attenuation using only direct waves. Analysis of coda waves provides a powerful tool to separate intrinsic and scattering attenuation.

To describe the coda energy decay with time, coda attenuation (Q_C) is defined as

$$E(f,t) = S(f)R(f)t^{-\alpha}e^{-2\pi ft/Q_C(f)}, \tag{1.1}$$

where E is the power spectrum, S is a frequency-dependent source amplitude term, R is a frequency-dependent station amplitude term, t is the lapse time, f is the frequency, α is a positive constant that is related to geometrical spreading and wave type (Aki and Chouet, 1975), and Q_C is the coda quality factor. The physical meaning of Q_C is of great interest to seismologists. It is a combination of intrinsic and scattering attenuation based on the scattering model (Aki and Chouet, 1975; Shapiro et al., 2000). Many studies indicate the value of coda attenuation, Q_C^{-1}, correlates with tectonics. For example, high Q_C^{-1} values are observed in active regions and low values in stable regions (e.g. Singh and Herrmann, 1983; Hoshiba, 1993; Mitchell et al., 1997; Hiramatsu et al., 2000; Jin and Aki, 2005; Sato et al., 2012). There are a variety of studies to explore the relation between temporal changes of Q_C and seismicity, especially some possible precursors before large earthquakes (Jin and Aki, 1988; Su and Aki, 1990). However, this topic is still in debate, because this precursory behavior is not consistently observed (Beroza et al., 1995; Hellweg et al., 1995; Aster et al., 1996; Tselentis, 1997; Sumiejski and Shearer, 2012).

Chapter 2

No clear tidal triggering of earthquakes in the central Japan region

We search for possible localized tidal triggering in earthquake occurrence near Japan by testing for tidal periodicities in seismicity within a variety of space/time bins. We examine 74,610 earthquakes of $M \geq 3$ in the Japan Meteorological Agency (JMA) catalog from January 2000 to April 2013. Because we use many earthquakes for which accurate focal mechanisms are not available, we do not compute tidal stresses on individual fault planes, but instead assume that the mechanisms are likely to be similar enough among nearby events that tidal triggering will promote earthquake occurrence at specific tidal phases. After dividing the data into cells at a range of spatial (0.2°, 0.5°, 1.0°) and temporal dimensions (100, 200, 400 days), we apply Schuster's test for non-random event occurrence with respect to both the semi-diurnal and semi-monthly tidal phases. Because the resulting p-values will be biased by temporal clustering caused by aftershocks, we apply a declustering method that retains only one event per tidal cycle per phase increment. Our results show a wide range of p-values for the localized earthquake bins, but the number of bins with very small p-values (e.g., $p < 0.05$) is no more than might be expected due to random chance, and there is no correlation of low p-value bins with the time of the 2010 M 9.0

Tohoku-oki earthquake.

2.1 Introduction

Because cyclical stressing rates from the Earth tides are typically much higher than the long-term buildup rate of tectonic stresses, many studies have searched for a possible correlation between earthquake occurrence and tidal phase. Although most of these studies find no clear relation between earthquakes and tides, evidence for at least some correlation has been found in a number of regions. Métivier et al. (2009) and Wilcock (2009) reported regional tidal triggering and Tanaka et al. (2002a) and Cochran et al. (2004) reported tidal triggering influence on a global scale. Some studies have reported a positive correlation between tidal triggering and certain types of focal mechanisms (Tsuruoka et al., 1995; Cochran et al., 2004). On the other hand, Shudde and Barr (1977) and Vidale et al. (1998) reported no correlation or a weak regional correlation, and on a global scale, Heaton (1982) and Hartzell and Heaton (1989) found no evidence for tidal triggering.

Recently Tanaka and her collaborators (Tanaka et al., 2002b; Tanaka, 2010) suggested that enhanced tidal correlation of earthquake occurrence may occur prior to large earthquakes in a region near their hypocenters, including recent giant megathrust earthquakes in Sumatra and Japan. Motivated in part by these results, Brinkman et al. (2015) presented an earthquake generation model that predicts an increased likelihood of large earthquakes during periods when small earthquake occurrence correlates with daily tidal stresses. Because of the potential value of Tanaka's observations for earthquake prediction, it is important to see if they can be confirmed using additional data. Her analyses for the 2004 Sumatra and 2011 Tohoku-Oki earthquakes used the GCMT catalog of M $\geq$ 5 events (Tanaka, 2010, 2012). Here we take advantage of the much larger catalog of Japanese events provided by the local networks to examine possible localized tidal triggering of earthquakes near Japan, including time periods before and after the

2011 M_W 9.0 Tohoku-Oki earthquake. We find no clear evidence for statistically significant tidal periodicities in the seismicity rate for any of our space-time seismicity bins.

2.2 Method

Ideally, studies of possible tidal triggering of earthquakes should compute the tidal stresses on the earthquake faults to establish directly when earthquakes should be encouraged and discouraged. This requires knowledge of the fault orientation, which is usually estimated from focal mechanisms and the local tectonics. However, because event catalogs typically only include focal mechanisms for relatively large earthquakes, this prevents analysis of the much more numerous smaller events.

Here we adopt the simpler approach of searching for non-random distributions of event times with respect to tidal phase, without establishing any explicit relationship to stress or the most likely tidal phase to promote triggering. It should be noted that this approach could fail to detect tidal triggering if a variety of focal mechanisms are present in a region, which trigger at different times during the tidal cycle. However, because nearby events typically have similar focal mechanisms (e.g. Hardebeck, 2006), it is likely that sufficiently localized regions will show clear peaks in occurrence time phase if tidal triggering is present. That is, similar mechanisms likely have similar fault orientations and will have similar tidal stress behavior on the fault and thus should trigger at nearly the same tidal phase. If local tidal triggering is present, we should then see a peak in the number of events occurring at a particular tidal phase rather than a purely random distribution of tidal phases.

To test the local similarity of Japanese focal mechanisms, we use events from the 1990 to 2010 GCMT catalog (see Fig. 2.1) and apply Hardeback's (2006) method to measure the angular difference between focal mechanism pairs. The angular difference is defined as the minimum rotation about any axis to bring the two mechanisms into alignment. Figure 2.2 shows the relation between the hypocentroidal distance separation and angular difference of each pair of events in the GCMT catalog. There is large scatter, but, as expected, the median angular difference decreases as the separation distance decreases. Very similar results are obtained using the declustered catalog that we describe later. The median angular difference is 31.0°, 41.6°, and 48.3° for separation distances of 0.2°, 0.5°, and 1°, respectively. However, given that the median angular difference is about 20° even at zero separation, it is likely that a substantial fraction of the observed angular differences are due to measurement error, rather than true differences in mechanisms (see Hardebeck, 2006). In any case, our approach here is to focus on nearby events for which our assumption of focal mechanism similarity is most likely to be valid. We therefore experiment with dividing the data into cells with spatial scales of 0.2°, 0.5°, and 1.0°. To test for possible temporal variations in tidal triggering, we also divide the data into temporal cells of 100 days, 200 days, and 400 days, aligned with the Tohoku-Oki earthquake time to account for the possibility of abrupt changes at the time of this earthquake.

For the seismicity in each space-time cell, we apply Schuster's test (often used in tidal triggering studies, e.g., Schuster, 1897; Heaton, 1982; Tanaka et al., 2002b, 2004, 2006, etc.) to test for statistically significant non-random distributions of tidal phases at the event times. Earth tides exhibit a variety of periodicities, but two of the strongest are the semi-diurnal (12.4206-hour period) and the semi-monthly (14.7653-day period). Note that the semi-monthly period is the average time between new and full Moons, when the tides have higher amplitudes due to the beating between the periods of the lunar and solar tides. If earthquakes are quickly triggered at a threshold maximum level of stress, then both of these periods are likely to be associated with earthquake occurrence.

For these two periods, we compute p-values for the distribution of tidal phases using

$$p = \exp\left(-\frac{(\sum_{i=1}^{N}\cos\theta_i)^2 + (\sum_{i=1}^{N}\sin\theta_i)^2}{N}\right) \tag{2.1}$$

where N is the number of earthquakes in the cell and θ_i is the tidal phase of the i-th event. The p-value is an estimate of the probability that the tidal phases are randomly distributed; thus $p < 5\%$ indicates a possibly significant correlation between Earth tide and earthquake occurrence in the cell.

As discussed before, we have divided the catalog into small cells and apply Schuster's test separately to the data in each cell. Because there are a large number of cells, about 5% of them are expected to have p-values smaller than 0.05 purely by random chance. However, if localized tidal triggering is present for a significant number of cells, the number of cells with $p < 0.05$ will be above the expected average. We test for this by plotting histograms of the p-values at increments of 0.05, compared to a reference line that shows the expected purely random distribution.

Schuster's test assumes that earthquakes are independent events and thus the p-values can be biased by temporal earthquake clustering unrelated to the tides (e.g., aftershock sequences). We can test whether this is an important factor in our data set by examining the distributions of p-values for periods not associated with the tides, i.e., for which no triggering should be detected. For this purpose we use over 70,000 earthquakes from the JMA catalog (see next section for more details) and test over 500 seismicity bins at increments of 0.5° and 200 days. We first analyze the raw catalog and test for non-random phase by computing the p-values with respect to periods of 7 hours, 12.42 hours (the semi-diurnal tidal period), and 17 hours; as well as the much longer periods of 11 days, 14.77 days (the semi-monthly tidal period) and 19 days. These results are plotted in the left column of Figure 2.3, which includes only bins for which there are 10 or more events. In all cases, there are many more bins with p-values less than 0.05 than would be expected due to random chance, and this is just as true for the non-tidal periods as the tidal periods. This is strong evidence that temporal clustering is biasing the results.

Because most of the temporal clustering is probably caused by aftershock sequences, we first experimented with removing aftershocks by applying the Reasenberg Declustering Method (RDM) (Reasenberg, 1985). The basic idea of RDM is to identify aftershock populations by defining an interaction zone following each earthquake in the catalog. Any earthquake that occurs within the interaction zone of a prior earthquake is considered an aftershock and is statistically dependent on it. Events thus associated are referred to as belonging to a cluster. The spatial and temporal extents of the interaction zone increase with the mainshock size and are defined based on a probabilistic model. We applied the RDM algorithm (using its default parameters) to the complete catalog to remove likely aftershocks and then processed the declustered catalog using the same binning scheme as before. These results are shown in the middle column of Figure 2.3. The anomalously large number of *p*-values below 0.05 is reduced somewhat compared to the raw catalog, particular for the shorter periods shown in Figure 2.3a. However, with the exception of the results for the 7 hour period, there are still more anomalous *p*-values than expected due to random chance, even for the non-tidal periods. By increasing the radius scaling in the Reasenberg method one can remove slightly more events, but not enough to change the overall results shown in Figure 2.3. Thus, the RDM approach does not seem to assure statistical independence of the occurrence times that go into Schuster's test.

This could be caused by several factors. RDM may not be removing all the aftershocks or the catalog could have a significant number of swarms, which have temporal clustering but are not readily explained with mainshock-to-aftershock triggering. To better remove the biasing effects of temporal clustering, we develop a new approach to event declustering that is specific to tidal triggering analysis. This method bins the seismicity within each cell into 16 equal increments of tidal phase and retains only the maximum sized earthquake per phase increment per tidal cycle number (see Fig. 2.4). This prevents a large number of events separated in time by only a small fraction of the target tidal periodicity from biasing the results. It also has the advantage of potentially being able to identify tidal periodicities within extended aftershock sequences (i.e., spanning many tidal cycles), which contain mostly events that would be removed with RDM-declustering. Results of applying this tidal phase binning approach are shown in the right column of Figure 2.3. The distribution of *p*-values now appears much more random, both at tidal periods and the four other periods that we tested.

Note that if tidal periodicities are present in a data set, the phase-binning approach is slightly more likely to remove periodic events than “background” random events because they are more likely to occur in the same phase bin. However, this bias is small, provided the number of tidal cycles is large, and we ignore its effects here. Another potential difficulty with this approach would occur if the seismicity rates were so high that most of the potential time bins contained earthquakes, in which case tidal periodicity might appear only as a larger number of events within particular bins and would go undetected if only one event is retained per bin. However, in our analyses generally only a small fraction of the phase bins contain earthquakes. In particular, 99.7% of our tests for semidiurnal tides and 85.5% of our tests for semi-monthly tides have events in fewer than 20% of the phase bins. Thus, this is not a problem for the vast majority of our tests, with most of the exceptions being for the semi-monthly tests during the very high seismicity rate immediately following the Tohoku mainshock. Because the tidal phase binning approach provides the least-biased results, we adopt this method for the remainder of our analyses.

To see how our approach compares to more established methods for analyzing tidal triggering based on Coulomb stress changes (e.g. Vidale et al., 1998), we examined solid-Earth tidal strains (including the ocean loading term) computed for the Tohoku-Oki earthquake region from 2005 through 2007 (Duncan Agnew, personal communication, 2015). We compared the strains at three different offshore points, but saw only very small differences among them, so for simplicity we consider only a point (36.54°N, 141.77°E) near the Tohoku epicenter. The strain calculation is for the seafloor, but at the long wavelengths of the tidal deformation, there is little depth dependence within the crust. From the strain tensor, we compute the stress tensor components assuming $\lambda = 45.9$ GPa and $\mu = 44.1$ GPa. We assume a large background tectonic stress (20 MPa) with horizontal convergence at 293°N, i.e., perpendicular to the trench. This allows us to compute the Coulomb stress changes (e.g. King et al., 1994) for faults of any orientation assuming an effective coefficient of friction of 0.4. For the shallow-dipping fault plane (strike 203°, dip 10°) inferred from the mainshock GCMT solution, these stresses have daily maximum values of about 2700 Pa during the times of new and full moon, and maximum values of about 700 Pa during first and third quarter moon.

We then performed two different tests. For the first test, we assumed the fault orientation of the GCMT solution for the Tohoku mainshock and computed the Coulomb stress as a function of time. We then found a stress value that is exceeded for only 5% of the time and created a series of synthetic catalogs of n events with times randomly assigned within these periods of high Coulomb stress. For each random catalog, we applied Schuster's test for both the semi-diurnal and semi-monthly periods and computed p-values. For $n = 20$, we found that 100% of the catalogs had p-values below 0.05 for the semi-diurnal period and 50% had p-values below 0.05 for the semi-monthly period. For the second test, we assigned a random fault orientation to each event, computed the Coulomb stress, and assigned a random time from within the 5% of the time with maximum stress. As expected for random fault orientations, the resulting event times are less obviously periodic. For $n = 20$, we found that only 10% of the catalogs had p-values below 0.05 for the semi-diurnal period and 15% had p-values below 0.05 for the semi-monthly period. The fraction of significant p-values increases with the number of events in the synthetic catalog. For $n = 100$, 30% of the catalogs had p-values below 0.05 for the semi-diurnal period and 56% had p-values below 0.05 for the semi-monthly period. Thus, given sufficient numbers of events, our simple approach will detect tidal triggering driven by Coulomb stress changes, even if the faults have random orientation. However, as described above and shown in Figure 2.2, the focal mechanisms in our dataset are quite similar over short distances, and thus we expect our method to perform for the real data more like the first synthetic test than the second. Our test is less sensitive than tests based on explicit Coulomb stress calculations because we do not take into account the tidal stress amplitude (e.g., some of the 12-hour tides are of higher amplitude than others). However, because we do not require event focal mechanisms we can apply our test to larger numbers of events, which should compensate to some degree for its lower sensitivity.

2.3 Results

We examine M $\geq$ 3 events in the JMA catalog from January 2000 to April 2013 in the central Japan region from 130°E to 146°E and from 29°N to 46°N (see Figure 2.1). Although the JMA catalog contains many events smaller than M 3, we use this cutoff to yield a relatively complete catalog even in the offshore region (see Supplemental Figure S2.1). It's possible that the catalog is missing a small number of events larger than M 3, but this is unlikely to bias our results very much, particularly because there is no reason to expect tidally triggered events to be absent from the catalog more than non-tidally triggered events. Later we will show that our results are robust with respect to the minimum magnitude, i.e., we obtain similar conclusions using a less conservative M 2.5 cutoff. We analyze a total of 74,610 earthquakes, of which only 1187 are in the GCMT catalog, with 25 earthquakes larger than M 7.0 including the 2011 M_W 9.0 Tohoku-Oki earthquake. We divide the data into cells with a range of spatial (0.2°, 0.5°, 1.0° in both latitude and longitude) and temporal dimensions (100, 200, 400 days) and compute the p-value for each cell (following our phase-bin declustering method) with respect to both the semi-diurnal and semi-monthly tidal phases.

Figure 2.5 summarizes our results for all of the space-time bins with respect to both the semi-diurnal and semi-monthly tidal phases, presenting results only for bins containing at least 10 events. The distribution of p-values now appears close to random. Although one can identify specific bins with p-values below 0.05, the total number of such bins is close to what would be expected due to random chance. For the semi-diurnal tidal period, only 3 of the 9 bin combinations have numbers of p-values below 0.05 that are more than the numbers expected due to random chance. For the semi-monthly tidal period, none of the 9 bin combinations have numbers of p-values below 0.05 that are more than the expected numbers. However, this plot could mask the presence of extremely anomalous p-values that might none-the-less indicate strong tidal triggering in one or more bins. To test for this possibility, we identified 62 out of

7365 total bins (i.e., 0.84%) with p-values less than 0.01 and 2 out of 7365 total bins (i.e., 0.03%) with p-values less than 0.001 for semidiurnal tides and for semi-monthly tides 37 out of 6443 total bins (i.e., 0.57%) with p-values less than 0.01 and none with p-values less than 0.001. These numbers do not indicate the presence of any bins with p-values below what might be expected for the total number of bins that we analyzed (see Supplemental Figure S2.2).

Tanaka (2010; 2012) suggested that enhanced tidal correlation of earthquakes may occur prior to large earthquakes in a region near their hypocenters. Our results here are relevant to the question as to whether such enhanced tidal correlation can observed before the 2011 M_W 9.0 Tohoku-Oki earthquake. Figure 2.6 and Figure 2.7 show the distribution of anomalously low p-values (≤ 0.05) for our temporal cells immediately prior to the Tohoku-Oki earthquake. We also plot the Chu et al. (2011) hypocenter for the mainshock. Red rectangles indicate that the p-value of the cell is smaller than 0.05, gray rectangles are for larger p-values. In general, the number of cells with $p \leq 0.05$ is no more than would be expected from random chance. There also is no compelling correlation of the red cells in this figure with the Tohoku-Oki epicenter. There are some red cells near the epicenter for the (1°, 200 day) and (1°, 400 day) bins for the semi-diurnal period and the (0.5°, 400 day) bin for the semi-monthly period (with p-values of 0.029, 0.045, and 0.01, respectively), but these anomalies are not robust with respect to the binning scheme. As an additional test, we repeated our analyses using a magnitude cutoff of 2.5 rather than 3.0 (resulting in about 2 times more earthquakes in total), and found that only the (1°, 400 day) semi-diurnal bin near the epicenter remained anomalous (in this case with a p-value of 0.026 rather than 0.01). The $M \geq 2.5$ results are plotted in Supplemental Figures S2.3 and S2.4. The $M \geq 2.5$ results also yielded a semi-diurnal 0.2° bin near the epicenter with a p-value of 0.036 for all three time windows as the 11 events in this bin are all within 100 days of the Tohoku-Oki mainshock. The largest occupation fraction of phase bins is 8.54% for the 100 day case. It should be noted that 10 of these 11 events are from the immediate foreshock sequence of the Tohuku-Oki mainshock (see below), but represent only a somewhat arbitrarily windowed portion of the complete foreshock sequence.

The Tohoku-Oki earthquake was preceded by a pronounced 23-day foreshock sequence (Kato et al., 2012), including aftershocks of a M_W 7.3 earthquake occurring two days before the M_W 9.0 mainshock. The foreshocks occurred mainly to the east and northeast of the mainshock epicenter. Because none of our spatial bins captures the entire foreshock sequence, it makes sense to study the sequence separately to see whether it might exhibit any tidal periodicity. Figure 2.8 shows the locations of 327 $M \geq 2.5$ foreshocks and the diurnal tidal phase versus time for both the raw catalog and the phase-bin reclustered catalog (the foreshock sequence is not long enough to test for semi-monthly periodicity). The p-values in both cases are about 0.65 and thus there is no evidence for tidal periodicity in the foreshock sequence. Overall, we find no clear evidence for observable tidal triggering in seismicity prior to the 2011 Tohoku-Oki earthquake.

As described earlier, our approach has the advantage of including many more earthquakes than methods that require fault orientations in order to explicitly compute tidal contributions to Coulomb stresses, but the disadvantage of not taking into account variations in tidal stress amplitudes. A full Coulomb stress analysis is beyond the scope of our paper, but as a final test we did find the number of events in the catalog from 2005 to 2007 within the 5% of times with the highest Coulomb stress and the 5% of times with the lowest Coulomb stress, assuming all the faults have the same orientation as the shallow-dipping fault in the GCMT solution for the Tohoku mainshock. For the Reasenberg declustered catalog, 4.56% and 5.26% of the events occurred during the highest and lowest stress times, respectively. For the original catalog, the corresponding numbers are 4.64% and 5.41%. Thus, these results do not provide any evidence for strong tidal triggering in the 2005-2007 catalog, at least for events with shallow-dipping thrust mechanisms.

2.4 Conclusions

We use a large set of earthquakes to search for evidence of localized tidal triggering near central Japan from 2000 to 2013. A new time-bin declustering method is adopted to remove temporal clustering that can bias tidal triggering estimates. The method bins the seismicity within each cell into 16 equal increments of tidal phase and retains only the maximum size earthquake per phase increment per tidal cycle number. After examining the results for all of the space-time bins with respect to both the semi-diurnal and semi-monthly tidal phases, we find that the number of bins indicating possible tidal periodicities is no more than might be expected due to random chance and that there is no clear tidal triggering signal prior to the 2011 Tohoku-Oki earthquake.

Acknowledgments

We would like to thank Professor Duncan Angew for synthetic solid-Earth tidal strains and helpful comments. The earthquake catalog used in this study is produced by the Japan Meteorological Agency (JMA), in cooperation with the Ministry of Education, Culture, Sports, Science and Technology. The catalog is based on seismic data provided by the National Research Institute for Earth Science and Disaster Prevention, the JMA, Hokkaido Univ., Hirosaki Univ., Tohoku Univ., the Univ. of Tokyo, Nagoya Univ., Kyoto Univ., Kochi Univ., Kyushu Univ., Kagoshima Univ., the National Institute of Advanced Industrial Science and Technology, the Geographical Survey Institute, Tokyo Metropolis, Shizuoka Prefecture, Hot Springs Research Institute of Kanagawa Prefecture, Yokohama City, and Japan Agency for Marine-Earth Science and Technology. We also thank William Wilcock and another anonymous reviewers for their suggestions to improve this manuscript.

Chapter 2, in full, is a reprint of the material as it appears in Journal of Geophysical Research: Solid Earth: Wang W. and Shearer P., 2015., "No clear evidence for localized tidal periodicities in earthquakes in the central Japan region", *Journal of Geophysical Research: Solid*

Earth, 120 (9), 6317-6328. The dissertation author is the primary investigator and author of this paper.

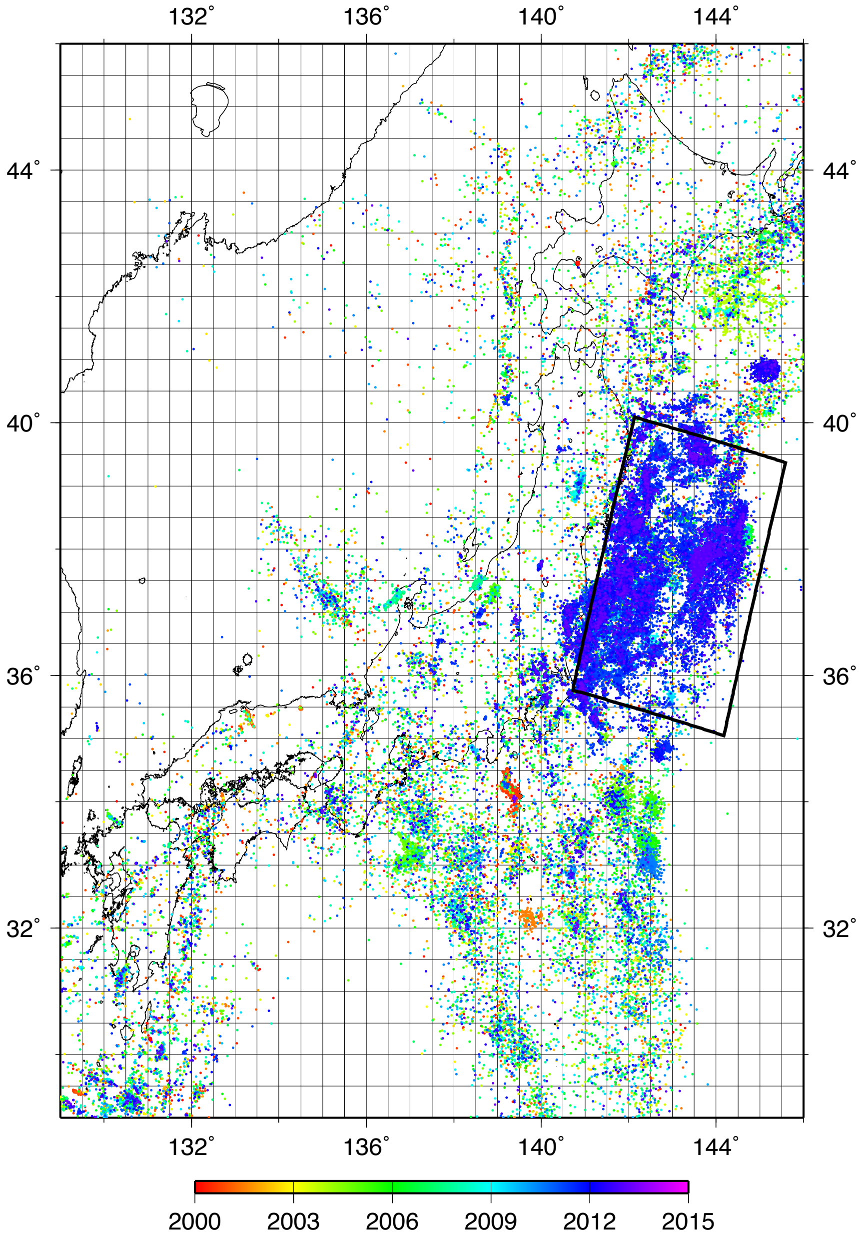

Figure 2.1: Earthquakes used in this study. 74,610 events of $M_W \geq 3.0$ from the JMA catalog (January 2000 to April 2013) are plotted, colored by their year of occurrence. Grid lines are shown every 0.5°.

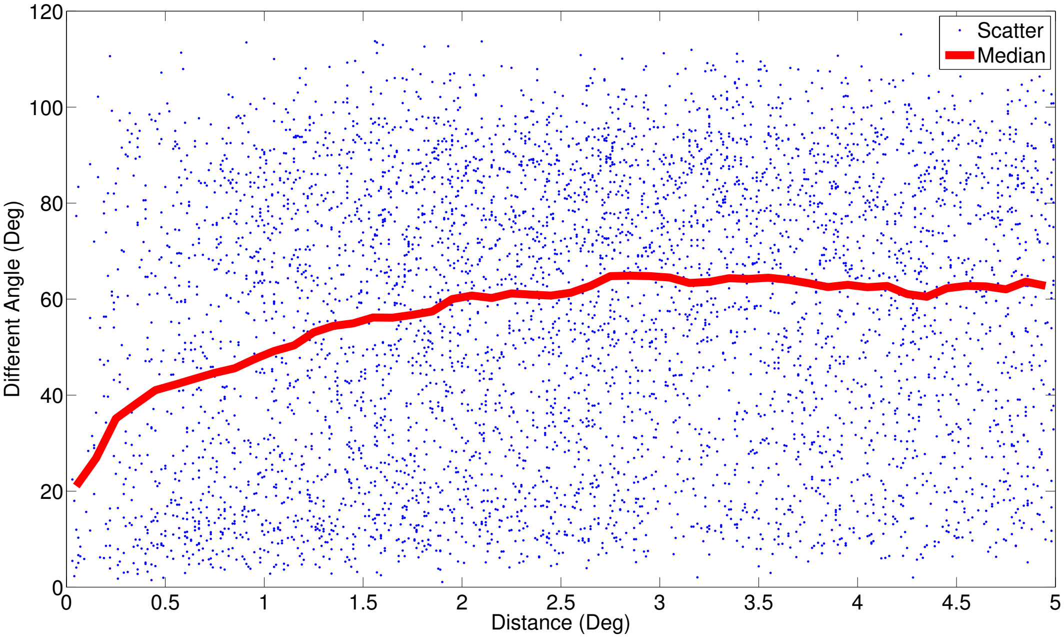

Figure 2.2: The angular difference between GCMT focal mechanisms versus their interhypocentral distance for event pairs in our study region. The red line is the median, computed in bins at 0.1° spaces. For clarity only a random 1% of the points are plotted.

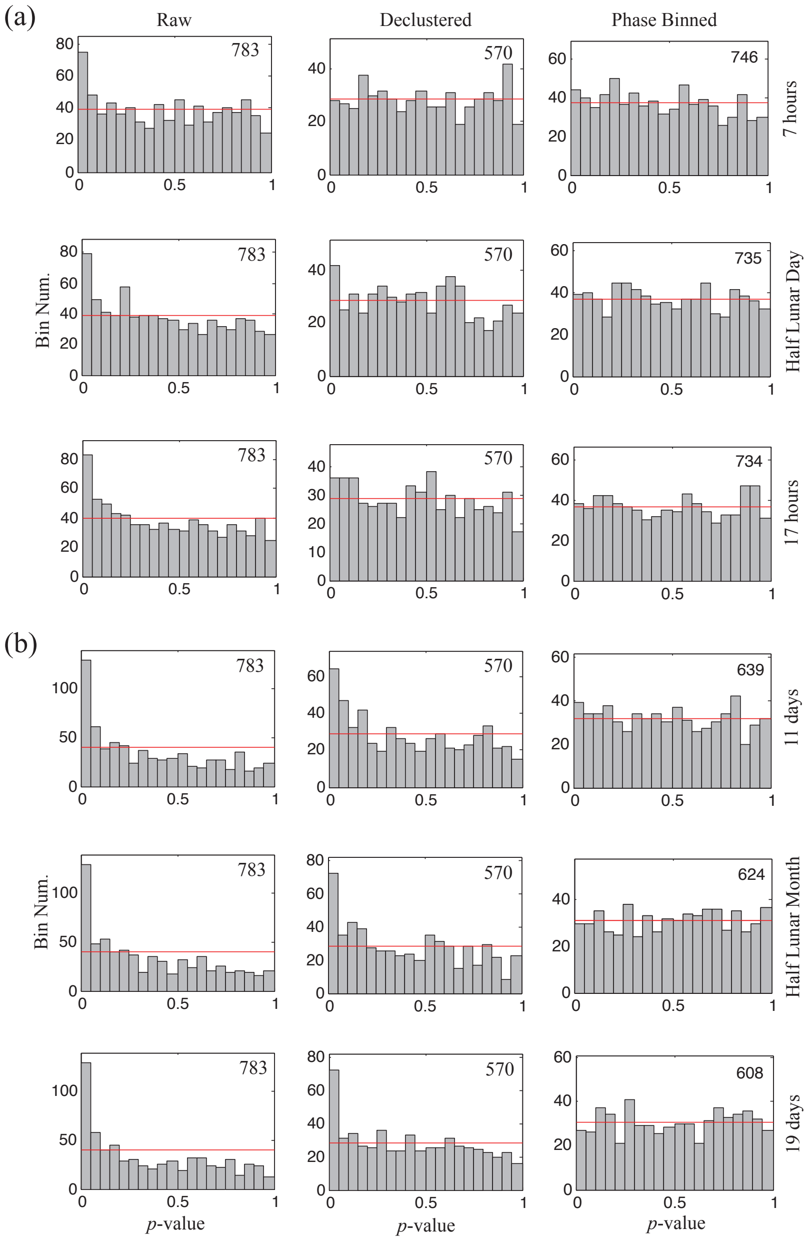

Figure 2.3: A comparison of the *p*-value distribution resulting from periodicity tests applied to seismicity bins in (left) the original JMA catalog, (middle) the Reasenberg declustered catalog, and (right) the phase-bin declustered catalog. The histograms show the numbers of *p*-values for bins with cell dimension (0.5° and 200 days) for tests at different possible periods, including non-tidal and tidal. The number in the upper right corner shows the total cell numbers for each case. The red line shows the expected number for a purely random distribution.

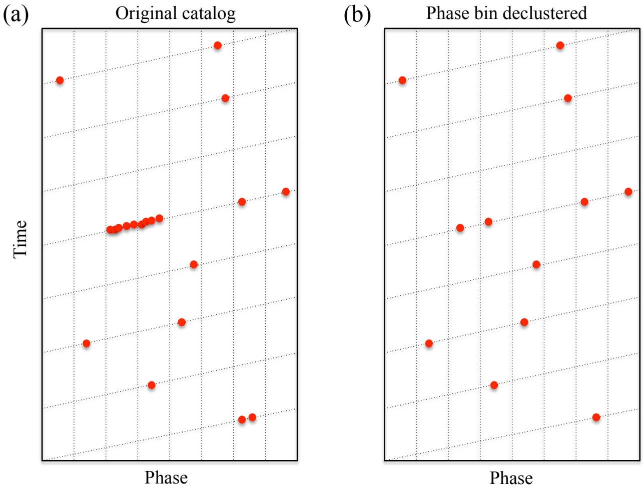

Figure 2.4: A synthetic example showing how the phase-bin declustering method works. (a) Event time versus phase for a given period. Red dots represent individual event location in time versus phase. Vertical dashed lines separate each cycle into eight equal increments. The sloping lines show increasing phase with respect to time in each cycle. Note that events within a tight temporal cluster (e.g., a swarm or aftershock sequence) will tend to occur at the same phase, possibly biasing tests of phase randomness. (b) The phase-bin declustered catalog, in which only the maximum magnitude event is retained for each phase bin at each cycle.

(a) Semi-diurnal Period

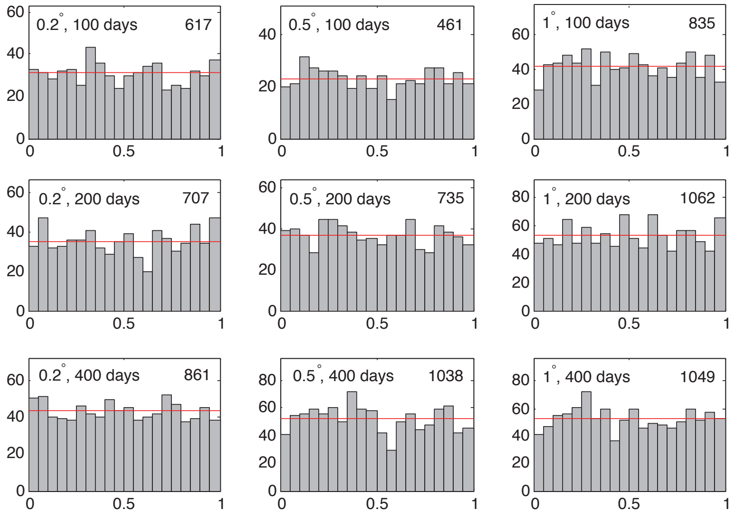

(b) Semi-monthly Period

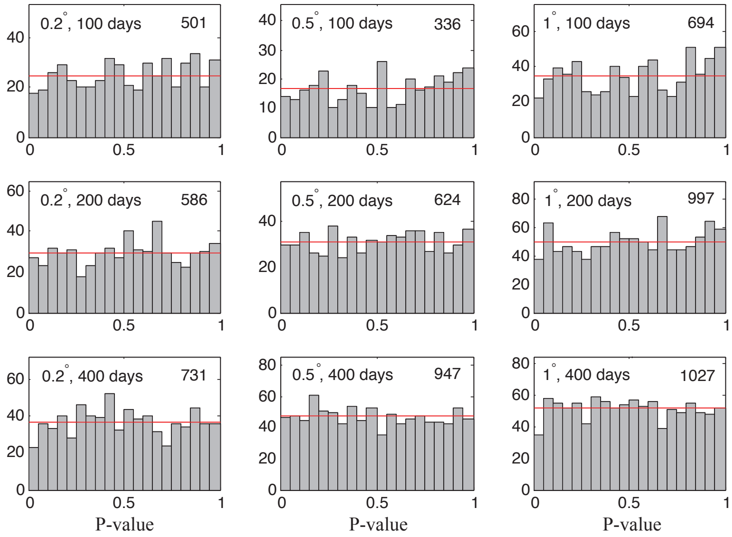

Figure 2.5: Histograms of the p-value distributions for tests of seismicity periodicity for (a) the semi-diurnal tidal period, and (b) the semi-monthly tidal period, for bins over a range of spatial (0.2°, 0.5°, 1.0°) and temporal dimensions (100, 200, 400 days). The numbers in the upper left corner show “spatial, temporal size” for each case. The number in the upper right corner in each histogram shows the total number of cells. The red line shows the expected number for a purely random distribution.

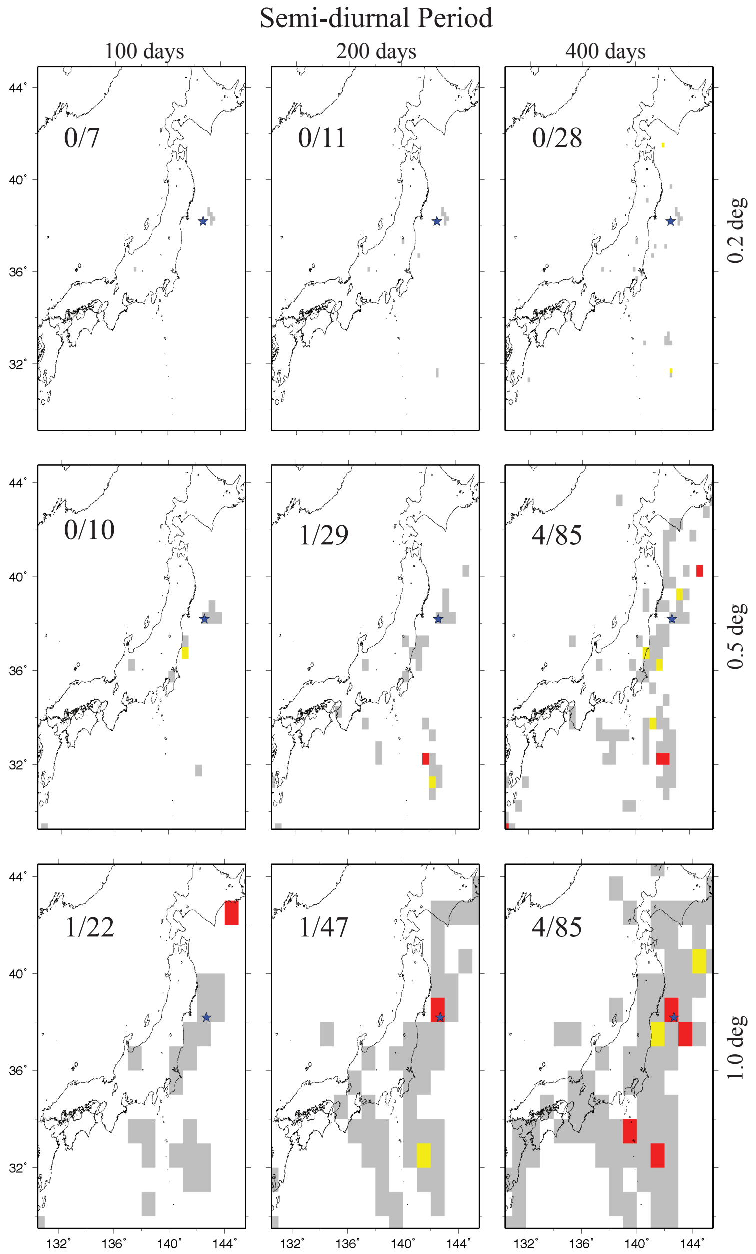

Figure 2.6: The spatial distribution of anomalous p-values for possible semi-diurnal tidal periodicity for $M \geq 3$ seismicity bins over a range of spatial (0.2°, 0.5°, 1.0°) and temporal dimensions (100, 200, 400 days), with each time bin ending immediately before the 2011 M_W 9.0 Tohoku-Oki earthquake. The star indicates the mainshock epicenter from Chu et al. [2011]. Red indicates p-values less than 0.05, yellow for p-values between 0.05 and 0.1 and gray for the other p-values. Only cells with more than 10 events are plotted. The number in each panel shows "(number of cells with $p < 0.05$)/(number of plotted cells)".

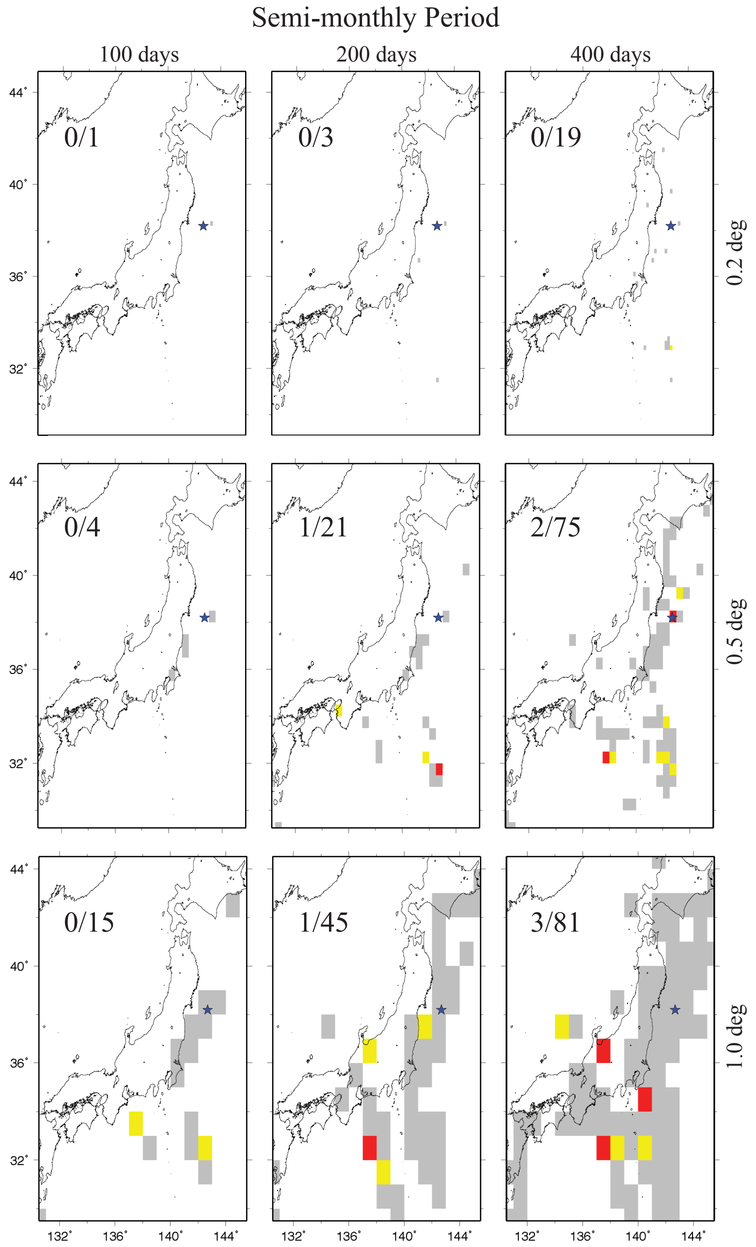

Figure 2.7: The spatial distribution of anomalous p-values for possible semi-monthly tidal periodicity for $M \geq 3$ seismicity bins over a range of spatial (0.2°, 0.5°, 1.0°) and temporal dimensions (100, 200, 400 days), with each time bin ending immediately before the 2011 M_W 9.0 Tohoku-Oki earthquake. The star indicates the mainshock epicenter from Chu et al. [2011]. Red indicates p-values less than 0.05, yellow for p-values between 0.05 and 0.1 and gray for the other p-values. Only cells with more than 10 events are plotted. The number in each panel shows "(number of cells with $p < 0.05$)/(number of plotted cells)".

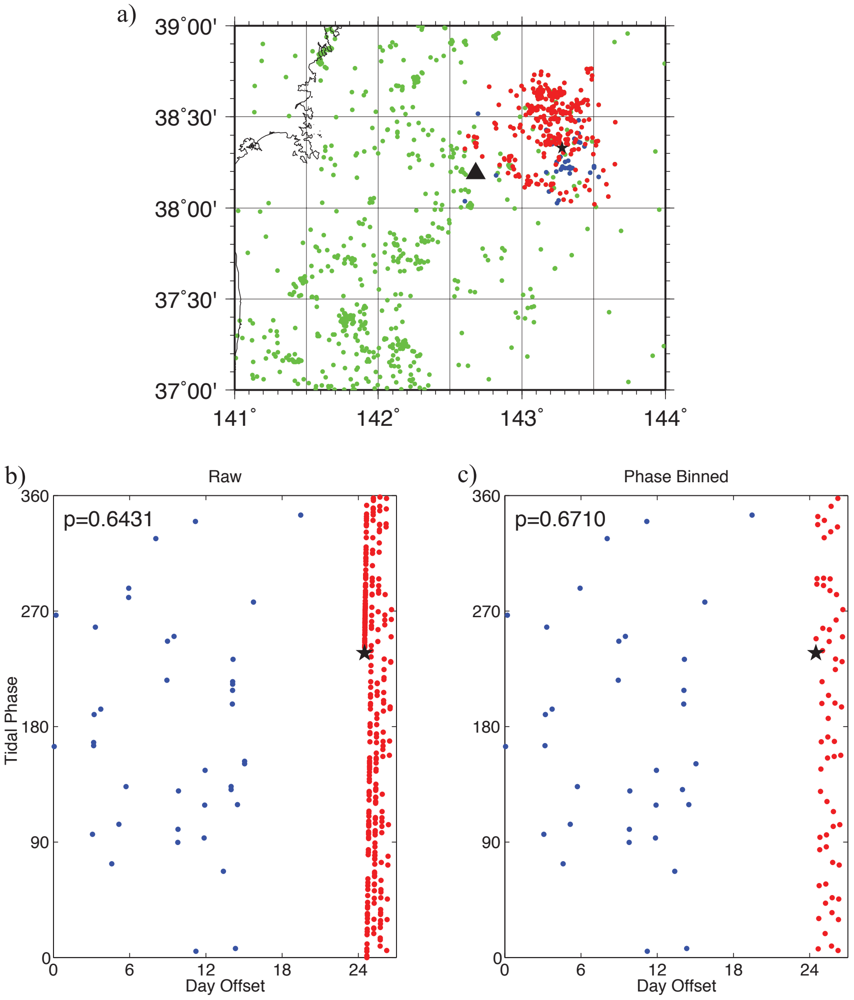

Figure 2.8: Foreshocks of the Tohoku-Oki earthquake: (a) Map of seismicity in the foreshock region within 400 days prior to the M_W 9.0 Tohoku-Oki earthquake, showing the epicenters of the M_W 9.0 mainshock (large black triangle) and the M_W 7.3 foreshock (small black star) and all the 327 $M_W \geq 2.5$ foreshocks (blue and red dots) between 2/13/11 and 3/11/11, including aftershocks of the M_W 7.3 foreshock (red dots). (b) Diurnal tidal phase versus time for the original 23-day foreshock sequence of the Tohoku-Oki earthquake between 2/13/11 and 3/11/11. Black star represents the M_W 7.3 foreshock and the *p*-value is listed. (c) Diurnal tidal phase versus time for the phase-bin declustered 23-day foreshock sequence of the Tohoku-Oki earthquake between 2/13/11 and 3/11/11.

2.5 Supplementary Materials

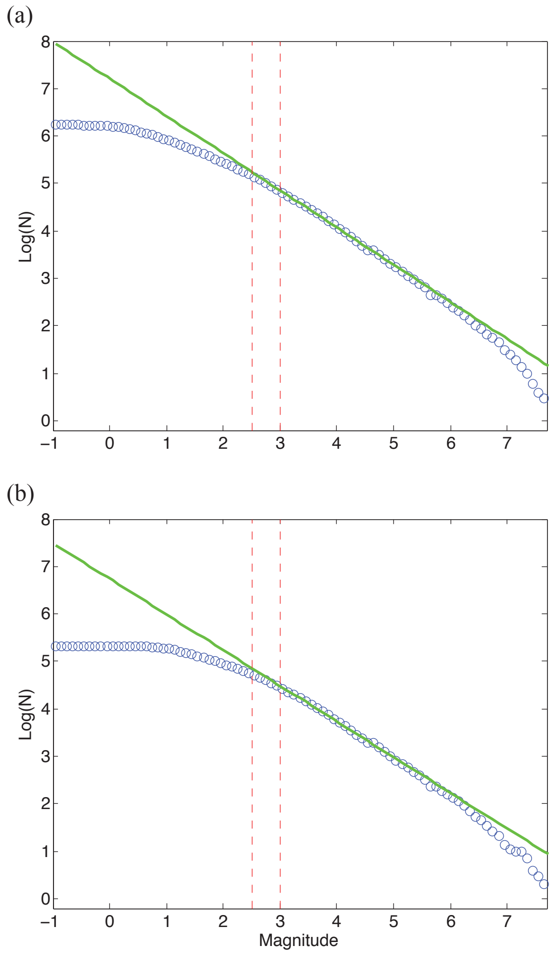

Figure S2.1: Earthquake count as a function of minimum magnitude for the JMA catalog (January 2000 to April 2013). The solid green line shows Gutenberg-Richter relationship. (a) is for the whole Japan region seen in Fig. 1, and (b) is for the offshore region marked with the black rectangle in Fig. 1.

(a) Semi-diurnal Period

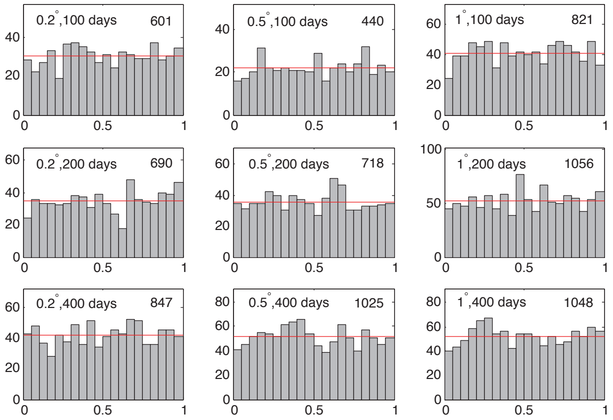

(b) Semi-monthly Period

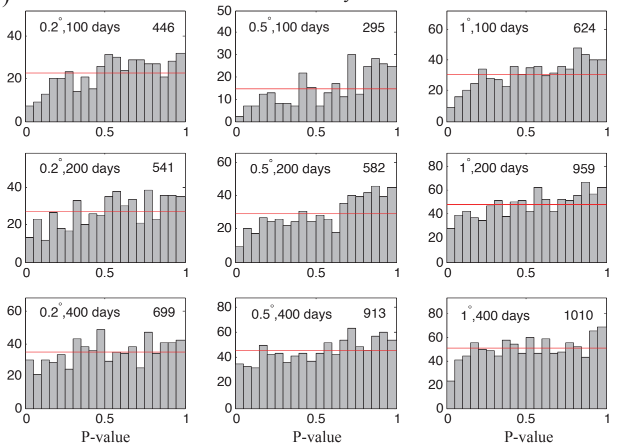

Figure S2.2: Histograms, similar to Fig. 5, but computed using 8 bins for the phase-bin declustering, of the *p*-value distributions for tests of seismicity periodicity for (a) the semi-diurnal tidal period and (b) the semi-monthly tidal period, for bins over a range of spatial (0.2°, 0.5°, 1.0°) and temporal dimensions (100, 200, 400 days). The numbers in the upper left corner show “spatial, temporal size” for each case. The number in the upper right corner in each histogram shows the total number of cells. The red line shows the expected number for a purely random distribution.

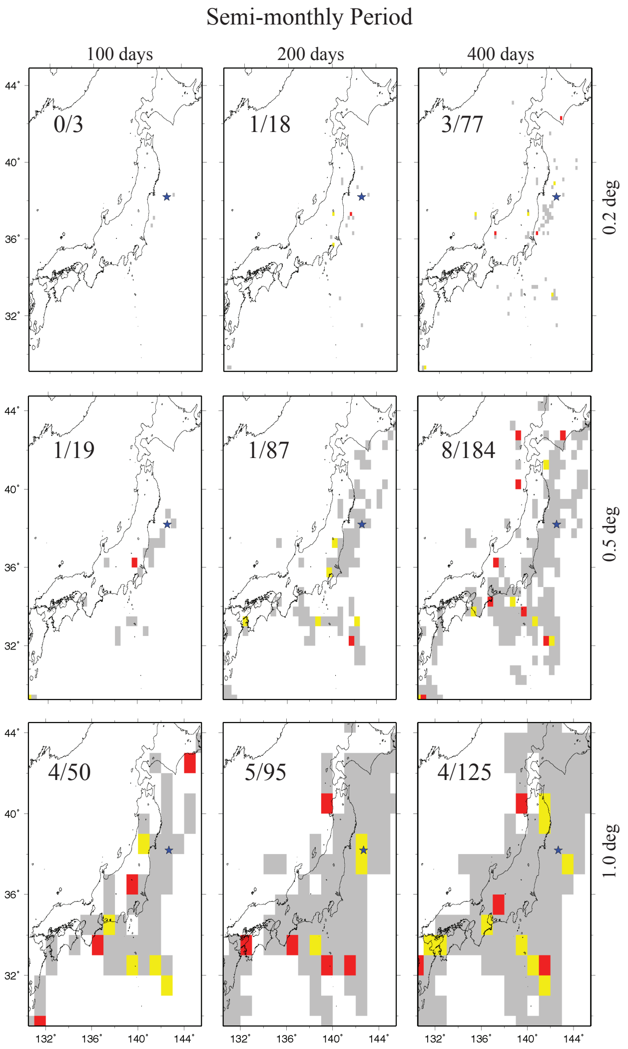

Figure S2.3: The spatial distribution of anomalous *p*-values for possible semi-dirunal tidal periodicity for $M \geq 2.5$ seismicity bins over a range of spatial (0.2°, 0.5°, 1.0°) and temporal dimensions (100, 200, 400 days), with each time bin ending immediately before the 2011 M_W 9.0 Tohoku-Oki earthquake. The star indicates the mainshock epicenter from Chu et al. [2011]. Red indicates *p*-values less than 0.05, yellow for *p*-values between 0.05 and 0.1 and gray for the other *p*-values. Only cells with more than 10 events are plotted. The number in each panel shows “(number of cells with $p < 0.05$)/(number of plotted cells)”.

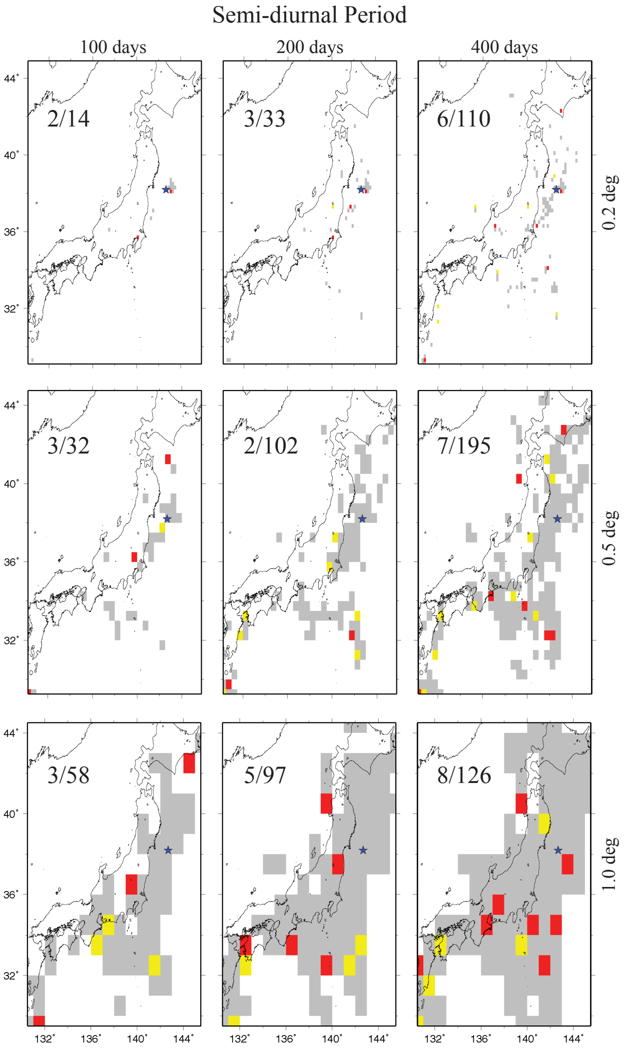

Figure S2.4: The spatial distribution of anomalous p-values for possible semi-monthly tidal periodicity for $M \geq 2.5$ seismicity bins over a range of spatial (0.2°, 0.5°, 1.0°) and temporal dimensions (100, 200, 400 days), with each time bin ending immediately before the 2011 M_W 9.0 Tohoku-Oki earthquake. The star indicates the mainshock epicenter from Chu et al. (2011). Red indicates p-values less than 0.05, yellow for p-values between 0.05 and 0.1 and gray for the other p-values. Only cells with more than 10 events are plotted. The number in each panel shows "(number of cells with $p < 0.05$)/(number of plotted cells)".

Chapter 3

Spatial decorrelation of tidal triggering and remote triggering at the Coso geothermal field

The triggering response of seismic fault systems to short- to mid-term (i.e., seconds to months) stress fluctuations can improve our understanding of earthquake nucleation, rupture failure processes, and local stress states. Geothermal fields are well known to be susceptible to triggering effects, since the injection and extraction activities change the local stress and fluid flow conditions within geothermal areas. Here, we examine two often-studied triggering responses at very different time scales: tidal triggering by Earth tides (day to month) and remote triggering by seismic waves (seconds), within the Coso geothermal field and its vicinity. Considering that the triggered earthquakes are typically small, we take the advantage of the new quake template matching catalog in southern California, which has nearly 2 times more events in the Coso region and is complete to about magnitude 0.3, to examine the tidal and remote triggering. We observe strong tidal triggering of earthquakes, but no remote triggering, within the Coso geothermal field (CGF), even though the fluctuations of tidal stresses are significantly smaller than those of the passing seismic waves. The preferentially tidal triggered earthquakes occur near the time of the maximum extensional tidal strain. A possible physical mechanism to interpret these two different triggering responses is a fluid unclogging fracture process sensitive to long-period strain/stress changes.

3.1 Introduction

A long-standing question in seismology is whether different periodic physical processes can trigger earthquakes and what this implies for earthquake initiation mechanisms. The continental crust is thought to be in a state of incipient failure nearly everywhere (Zoback and Zoback, 2002) and stress fluctuations can potentially push faults in a critical stress state to failure (Gomberg et al., 1997; Hill and Prejean, 2007; Delorey et al., 2017), either directly or from reductions in normal stress due to fluid transport and pore-pressure changes. If this is true, widespread earthquake triggering should be observed if the stress perturbations are large enough.

Two of the most widely studied examples of stress fluctuations as possible earthquake triggers occur at very different time scales. Dynamic triggering from the passing of seismic waves from distant earthquakes occurs at scales of seconds to tens of seconds, whereas triggering caused by Earth tides occurs over times of hours to days. Remote triggering from earthquakes has been observed worldwide for over two decades, especially in geothermal and volcanic areas (Hill et al., 1993; Gomberg and Davis, 1996; Prejean et al., 2004; Brodsky and Prejean, 2005; Peng et al., 2010; Meng and Peng, 2014; Aiken and Peng, 2014). In contrast, searches for tidal triggering of earthquakes have a much longer history, but positive results are still elusive (e.g. Schuster, 1897; Vidale et al., 1998; Beeler and Lockner, 2003; Wang and Shearer, 2015). Most of the well-documented tidal triggering examples are observed near-shore or offshore, where the ocean loading term can be almost ten times larger than the solid Earth tide alone (Tsuruoka et al., 1995; Cochran et al., 2004; Tanaka et al., 2002a, 2006; Métivier et al., 2009; Wilcock, 2009; Ide et al., 2016; Scholz et al., 2019). A robust statistical correlation between solid Earth tides and earthquake occurrence on the continent is hard to detect and requires a large and complete catalog (Métivier et al., 2009; Scholz et al., 2019).

Geothermal fields and volcanic areas are apparently more susceptible to triggering effects, because of their active tectonic settings and the presence of fluid and/or magma. In commercial geothermal fields, the continuous injection and extraction of fluids alters the stress state and fluid flow conditions within the porous medium and complex fracture system (Martínez-Garzón et al., 2013). Here we study the Coso region, which includes one of the largest geothermal plants in the United States. It has been in operation since 1987 witha total of 270 MW of rated capacity (Monastero, 2002). The Coso geothermal field (CGF) is located in eastern California between the Sierra Nevada and Argus Ranges, in the transtensional stress regime between the strike-slip San Andreas fault and the extensional Basin and Range province, subject to major strike-slip faulting and some normal faults (Walter and Weaver, 1980; Reasenberg et al., 1980). Zhang et al. (2017) report that remote triggering more likely occurs with the area surrounding the CGF rather than within the CGF itself. We investigate both remote and tidal triggering within and near the CGF to study the effects of the local stress state and fluid conditions on the triggering response.

3.2 Methodology

Both tidal and remote triggering studies require a large number of events to ensure their statistical confidence (Harrington and Brodsky, 2006; Métivier et al., 2009; Scholz et al., 2019). Recently, Ross et al. (2019) applied the template matching approach to detect 1.8 million earthquakes in southern California, about a 10-fold increase from the Southern California Seismic Network (SCSN) catalog (Yang et al., 2012). This enlarged catalog, with many more small events, improves our ability to detect statistically significant earthquake triggering (Vidale et al., 1998; Harrington and Brodsky, 2006). The completeness magnitudes in the CGF and its surroundings are 0.0 and 0.3, respectively, compared to 0.5 for the SCSN catalog (see Figures 3.1 & S3.1).

Tidal triggering studies often apply Schuster's test for statistical significance. However, this test assumes each event is independent, so the p-value can be biased by clustering effects in the seismicity, i.e., aftershock sequences and earthquake swarms (e.g. Wang and Shearer, 2015), which are not related to the triggering process. In this study, we apply two different methods to decluster the catalog. We first use the Reasenbergdeclustering method (RDM) (Reasenberg, 1985), which identifies aftershocks by checking whether these events are statistically located within the spatial and temporal interaction zone of a prior earthquake. The size of the interaction zone increases with earthquake magnitude. Since there are some swarms in the Coso region (Zhang et al., 2017) and RDM fails to identify and decluster the swarms, we apply the phase-bin declustering method (PBDM) (Wang and Shearer, 2015) to the RDM-declustered catalog. The PBDM declusters the catalog based on the tidal cycles, so it is only used for the tidal triggering study. Each cycle is divided into several equal-size bins, and only the largest event in each bin is kept. This processing removes the fully occupied cycles automatically in computing the p-values. In this study, the solid earth tides are computed for the 2004 version of the Goddard Ocean Tide Model (GOT4.7) plus a local model for the west coast of United States and British Columbia of Canada, using the program SPOTL (Agnew, 1997, 2012; Ray, 1999). The PBDM is applied to the synthetic tidal signals, which is dominated by the semi-diurnal periodicity.

Ideally, the geometry of the fault planes or the focal mechanisms of the triggered events could be used to relate tidal stress fluctuations to the shear and normal stress changes on the faults. However, faulting is complex in our study region and obtaining reliable focal mechanisms for the tiny events that make up the bulk of our catalog is very difficult (Martínez-Garzón et al., 2013). Therefore, we divide the study region into small cells ($0.02^\circ \times 0.02^\circ$) (see Figures 3.2 & 3.3), in which it is likely that the earthquakes will have similar focal mechanisms (Hardebeck, 2006; Wang and Shearer, 2015). These similar nearby events will be triggered at the same tidal phase assuming the background tectonic stress state is almost uniform. To examine the correlation between solid Earth tides and earthquake occurrence, we apply Schuster's test separately to the events in each small cell (Schuster, 1897), using only cells containing more than 200 events to ensure reasonable statistical confidence. For a random sequence, the Schuster's p-value is defined as

$$p = \exp\left(-((\sum_{i=1}^{N} cos(\theta_i))^2 + (\sum_{i=1}^{N} sin(\theta_i))^2)/N \right), \tag{3.1}$$

where is the tidal phase for the i-th event and N is the total event number. We define the maximum value of the tidal signal as occurring at 0 phase, i.e., dilatational strain in this study (see Figure S3.2a]). The p-value indicates the estimated probability that the earthquake occurrence has no correlation with the tidal phases. The 5%, i.e., 0.05, p-value is often used as a proxy to indicate a significant correlation between Earth tides and earthquake occurrence. However, since Schuster's test may overestimate the significance (Cochran et al., 2004), to be conservative we require a much lower p-value of 0.001 as a threshold to detect tidal triggering in our study region. Also, similar to Cochran et al. (2004), we define the number of excess events (Nex) as the number of events in the half cycle centered at the peak triggered tidal phase (see Figure S3.2b). The percent of excess event is defined as, $R_{ex} = (N_{ex} - N/2)/N$. In Figure S3.1b, the R_{ex} for the subarea A is around 7%, while the tidal triggering is visibly apparent with p-values smaller than 0.001.

To examine remote triggering, we calculate the seismicity change within 10 days after a large distant event relative to the background seismicity using β-statistics (Matthews and Reasenberg, 1988; Reasenberg and Simpson, 1992; Kilb et al., 2000; Hill and Prejean, 2007; Zhang et al., 2017). The $beta$-value is defined by the difference between the expected earthquake number within the study time window and the reference background seismicity normalized by the standard deviation of the expected seismicity. The $beta$-value is defined as,

$$\beta = [n_a - E(n_a; n_b)]/\sqrt{var(n_a; n_b)}, \tag{3.2}$$

where $E(n_a; n_b) = n_b(t_a/t_b)$ is the expected number during window t_a based on the background seismicity within t_b and $var(n_a; n_b) = n_b/(t_a/t_b)$ is the variance for a Poisson process. To facilitate comparisons, we apply the same spatial gridding scheme as in the tidal triggering study. A β-value larger than 2 or smaller than -2 indicates the remote triggering or not with 95% statistical confidence.

3.3 Results

We first examine tidal triggering based on two different tidal signals, dilatational strain (Figure 3.2 & 3.3) and tidal height (Figure S3.7). Both results indicate there is strong tidal triggering, i.e. $p < 0.1\%$, in part of the CGF, located where there is observed surface subsidence and highly active seismicity (see Figure 3.2, 3.3, and S3.7). This anomaly is distinct from its surroundings, as the only extreme low p-value region is located in the CGF. Based on the spatial pattern of p-values, we divided the CGF into four subareas (see Figure 3.2c). Figure 3.2d illustrates that subarea A shows strong tidal triggering, subarea B shows weak tidal triggering, and the other two subareas have no clear tidal triggering behavior. After we remove the potential swarms in this region using PBM, significant tidal triggering in subarea A is still present (see Figure 3.3). In the CGF, about 95% of earthquakes are shallow (< 3 km) earthquakes and related to geothermal operations. In CGF, about 95% of earthquakes are shallow earthquakes and related to geothermal operation (Zhang et al., 2017). Tidal triggering is observed for the shallow events alone (see Figure 3.3). We also designed several statistical tests to examine the spatial robustness of this low p-value region (see supplement and Figures S3.4-3.6). The triggered dilatational tidal phase in subarea A is around 0°, implying triggering occurs at times corresponding to the maximum dilatational stress.

Zhang et al. (2017) observed the absence of remote triggering in the CGF. They considered magnitude 1.3 and greater events in the SCSN catalog, compared to magnitude 0 in the QTM catalog used here. We search for distant earthquakes from 2008 to 2017 with Ms ≥ 7, depth ≤ 20 and epicentral distance > 100 km in the GCMT catalog (Dziewonski et al., 1981; Ekström et al., 2012). The estimated peak-ground velocities (PGVs) in the CGF are required to exceed 0.02 cm/s (Prejean et al., 2004; Harrington and Brodsky, 2006). The PGV can be estimated using the equation, , where Ms is the surface wave magnitude, A is the distance to the event, and T is surface-wave period (Lay and Wallace, 1995). We find 5 events in the catalog meeting these requirements (see Table S3.1). Of these, the 2010 El Mayor-Cucapah earthquake (Ms=7.3) is by far the strongest, generating over 0.2 cm/s PGV. For this earthquake, the CGF and its subarea A show no significant remote triggering within 10 days and 30 days after the event (see Figure 3.4). In addition, the other 5 earthquakes do not trigger earthquakes remotely in this area (see Figure S3.11-S3.14). Thus, using a greatly enhanced earthquake catalog our results confirm the absence of remote triggering in the CGF reported by Zhang et al. (2017).

3.4 Discussion and Conclusions

In this study, we directly observe a frequency-dependent earthquake triggering behavior in the Coso geothermal field. Compared to the reported tidal triggering in mid-ocean ridge or subduction zone environments (Tsuruoka et al., 1995; Cochran et al., 2004; Tanaka et al., 2002a, 2006; Métivier et al., 2009; Wilcock, 2009; Ide et al., 2016; Scholz et al., 2019), our study finds continental tidal triggering within the CGF but not its surroundings. However, detection of tidal triggering at the CGF required the large number of low magnitude ($M < 0.5$) earthquakes in the QTM catalog, as the SCSN catalog or QTM catalog cannot confirm a significant tidal signal using only magnitude 0.5 or larger events (see Figure S3.8). We also attempted to explore the triggering response of the Salton Sea geothermal field. Although we find some evidence for tidal triggering near this field (see Figure S3.10), its significance is much less clear than at Coso, since unfortunately the CalEnergy Subnetwort (EN) seismic network has been turned off since 2014 (see Figure S3.9) and there are many fewer events to analyze. Therefore, we do not include any discussion here for the Salton Sea field.

The continuous extraction of hot water and the injection of cold water into a geothermal reservoir causes deflation of the reservoir. At the CGF, we observe that the tidal triggered earthquakes preferentially occur around the maximum of the dilatation tidal stress. This result is consistent with most events occurring on normal and strike-slip faults caused by deflation of the geothermal reservoir, and which may be triggered by the dilatation stress (Fialko and Simons, 2000; Yu et al., 2018). It should be noted that the tidal stresses on the continent are much smaller than the dynamic stresses from passing seismic waves in remote triggering studies. The peak dynamic stress can be estimated using the equation , where v is the PGV, c is the phase velocity, assuming 3 km/s, and is the shear modulus, assuming 30 GPa, giving the stress for the six earthquakes we studied as ranging from 2 to 20 kPa. The peak dilatational tidal stress is about 0.5 kPa estimated from the peak dilatation tidal strain, assuming a Poisson solid. The tidal stress in the CGF is much smaller than the dynamic stress for the 2010 El Mayor-Cucapah earthquake (20 kPa). These frequency-dependent triggering behaviors shed light on the elusive mechanisms of triggering. Zhang et al. (2017) proposed that an unclogging fracture process removes the pore pressure gradient within the CGF and inhibits remote triggering. Under the unclogging scenario, the fluid driven into the porous medium by the periodic dilatational strain can act as a low-pass filter (Brodsky and Prejean, 2005). The pressure oscillation amplitude increases with the periodicity of the dilatational stress. The higher pore pressure change reduces the effective normal stress and enhances the probability of rupture failure, which can cause the geothermal fields to be more susceptible to tidal stress rather than dynamic stress. Previous studies have pointed out that long-period seismic waves trigger earthquakes more efficiently than short-period seismic waves at similar stress levels (Brodsky and Prejean, 2005) and static stresses can trigger local earthquakes even at smaller stress levels at the Long Valley Caldera geothermal field (Kilb et al., 2002; Hill et al., 2003).

Our study of remote triggering and dynamic triggering in Coso geothermal region is the first direct observation of frequency-dependent triggering since Brodsky and Prejean (2005) proposed a frequency-dependent triggering mechanism. Further analysis of catalogs with many small events may help to resolve whether this triggering behavior is a universal phenomenon.

Acknowledgments

We would like to thank Duncan Angew, Yuri Fialko, Zachary Ross, Daniel Trugman, David Sandwell, Adrian Borsa, John Vidale for helpful discussions and comments on this study. The QTM and SCSN earthquake catalog used in this study is provided by the Sourthern California Earthquake Center, which can be downloaded from the website 'http://scedc.caltech.edu/research-tools/downloads.html'. The SPOTL for computing the earth tides can be downloaded from the website 'https://igppweb.ucsd.edu/ agnew/Spotl/spotlmain.html'.

Chapter 3, in full, is currently under review for publication as Wang, W., Shearer P., and Xu X., "The spatial dislocation of tidal triggering and remote triggering at the Coso geothermal region". The dissertation author was the primary investigator and author of the paper.

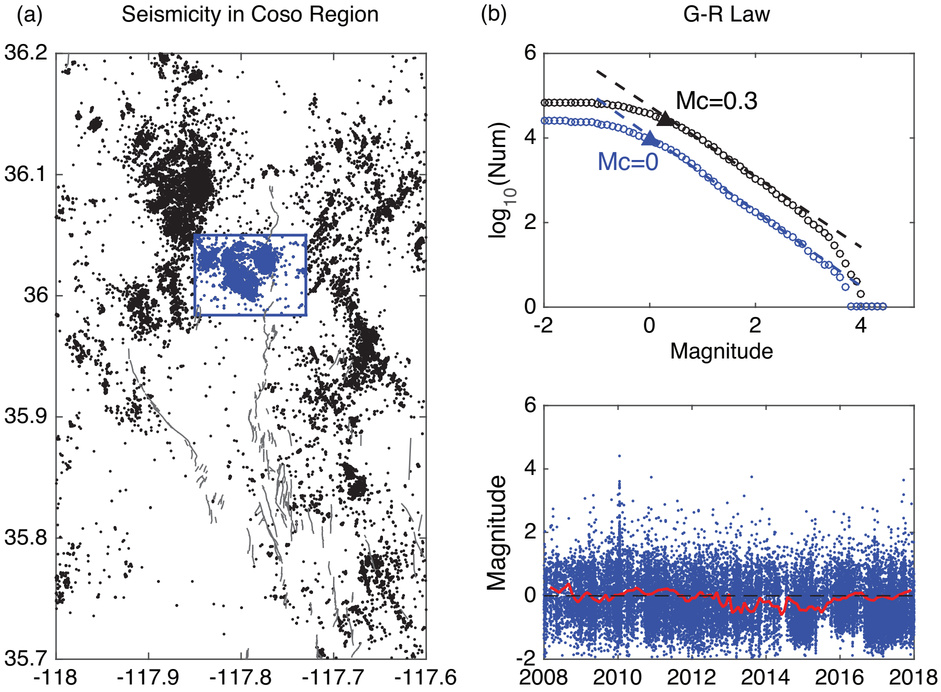

Figure 3.1: Seismicity in the Coso geothermal field. (a) shows the seismicity in the CGF (blue) and its surrounding area (black). (b) illustrates the Gutenberg-Richter law in the CGF and its vicinity with triangles indicating the approximate completeness magnitudes. (c) plots the temporal variation of completeness magnitudes (red line) in the CGF.

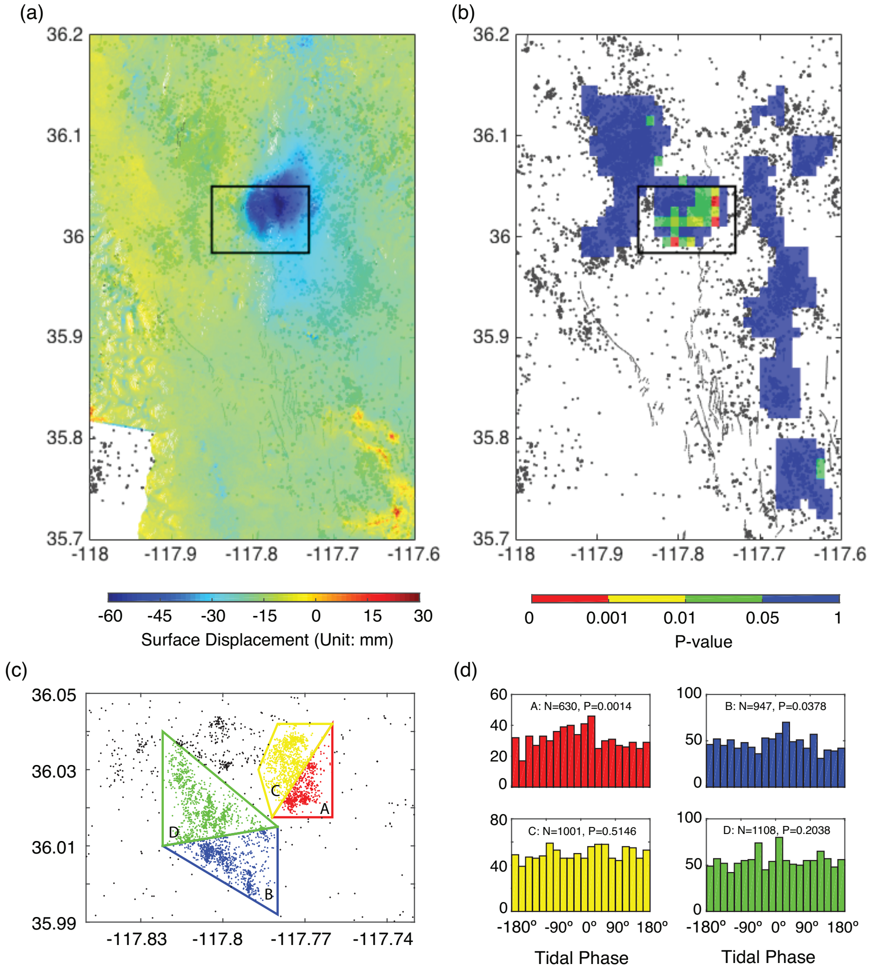

Figure 3.2: Spatial variations in tidal triggering compared to observed vertical surface displacement. (a) plots the p-value distribution for tidal triggering based on a 0.02° by 0.02° grid with shifts of 0.01°. (b) shows the surface displacement, as derived from InSAR data of Sentinel-1 between November 2014 and December 2017. (c) and (d) show four subsets of seismicity in CGF and their corresponding tidal phase histograms and p-values.

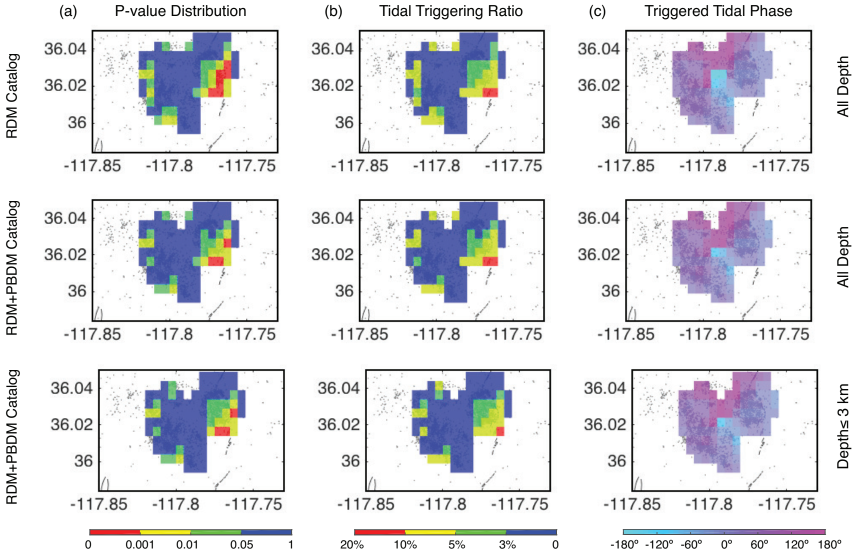

Figure 3.3: Maps of p-values, tidal triggering ratios, and triggered tidal phases in 0.02° by 0.02° grids with 0.005° shifts, with respect to the dilatational tidal strain. The top row shows the results for the RDM catalog alone. The middle and bottom rows show results for the RDM and PBDM catalogs, with the bottom row restricted to shallow events only ($<$ 3 km).

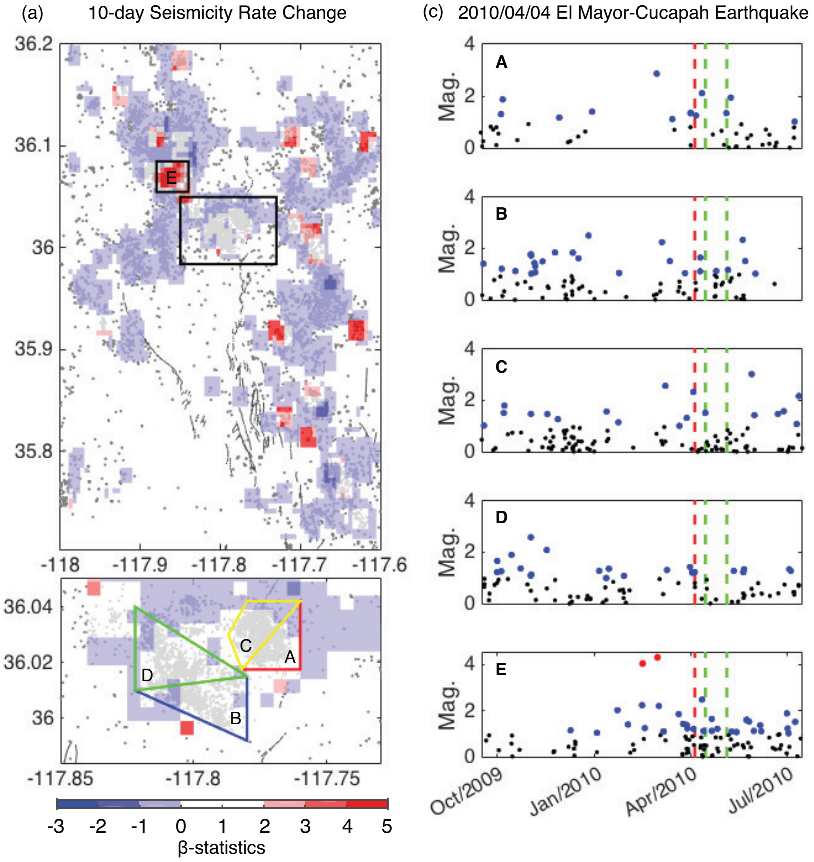

Figure 3.4: Estimates of seismicity rate changes and magnitude vs. time plots for subsets of the Coso seismicity for the 2010 El Mayor-Cucapah (EMC) earthquake. (a) indicates the beta test results in the CGF and its vicinity, and (b) shows the beta test in the black box. (c) shows the seismicity in the four subsets in (b) within 200 days before the EMC earthquake to 100 days after it. The black dots indicate small earthquakes ($M < 1$), blue dots for moderate earthquakes ($1 < M < 4$) and red dots for large earthquakes ($M > 4$). The red dashed line marks the earthquake occurrence time and the two green lines mark 10 days and 30 days after the EMC occurrence.

3.5 Supplementary Materials

3.5.1 Statistical Tests

To examine the spatial robustness of this low p-value region, we randomly pick one event and find the closest 200 or 500 events, then we apply PBM to this cluster and compute its p-value. We run this process for 2000 times ($>$ 1/0.001 to check the randomness of the extreme low p-value). After repeating this process many times, the results indicate that the extreme low p-values are almost all located in subarea A in the CGF (see Figure S4). In some cases, there may be extreme low p-values outside CGF, however, considering the randomness of the p-values, the robust spatial locations of the p-values are within the CGF region. The distribution of the triggered tidal phase in subarea A and B of CGF are more uniform than the surrounding areas (see Figure S4). Secondly, we randomly pick 5 years in the dataset and run the same process described above to check the location of the extreme low p-values. The results are similar to the whole dataset (see Figure S5). The spatial distribution of low p-values is generally more compact for the 500 event clusters than the 200 event clusters, since more tidal triggered events in the CGF dominate the p-values for the 500 event clusters. Finally, we compare the injection, projection, and net production data with the declustered seismicity within the CGF. The correlations between the seismicity and these parameters are very weak (see Figure S6), which has been reported by Trugman et al. (2016). This indicates that the tidal triggering of earthquakes has no significant modulation from anthropogenic activities.

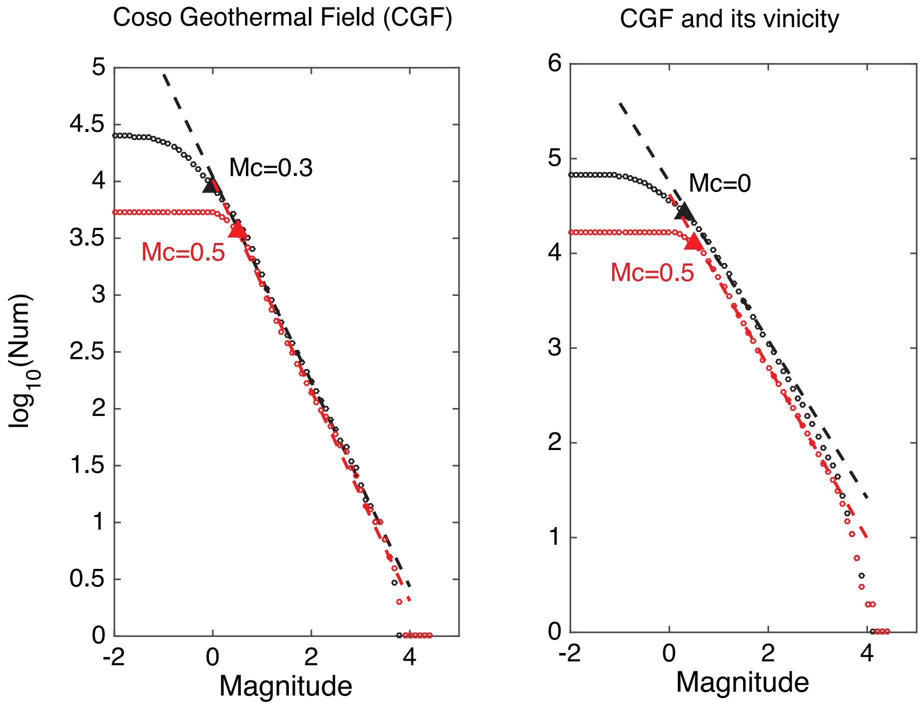

Figure S3.1: Comparison of the completeness magnitude of the Coso geothermal field and its surroundings for the QTM catalog (black) and SCSN catalog (red).

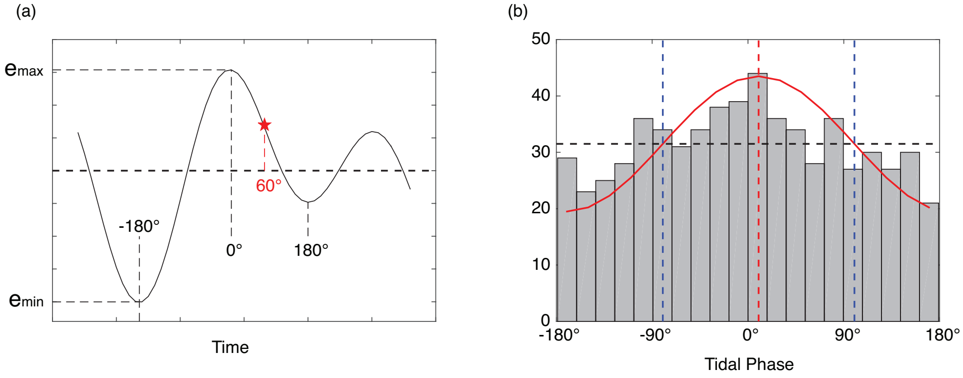

Figure S3.2: (a) A diagram of the tidal strain time series and one earthquake with tidal phase 60. (b) The histogram of tidal phases for the event in subarea A in Figure 2. The red line is the best fitting cosine function of the tidal phase distribution. The red dashed line marked the preferential tidal phase histogram, and two blue dashed lines mark the half cycle centered at the preferential tidal triggering phase.

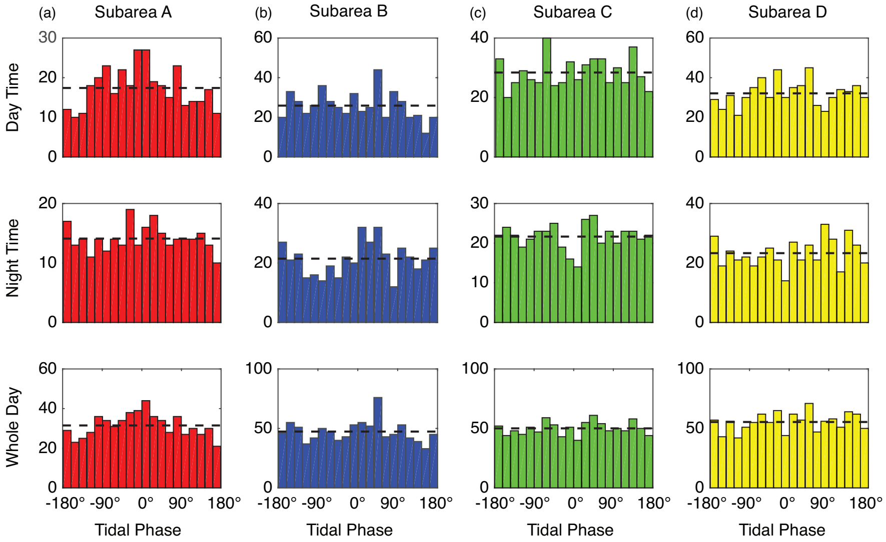

Figure S3.3: The day and night tidal distribution of tidal phases for the events in subareas A-D in Figure 2.

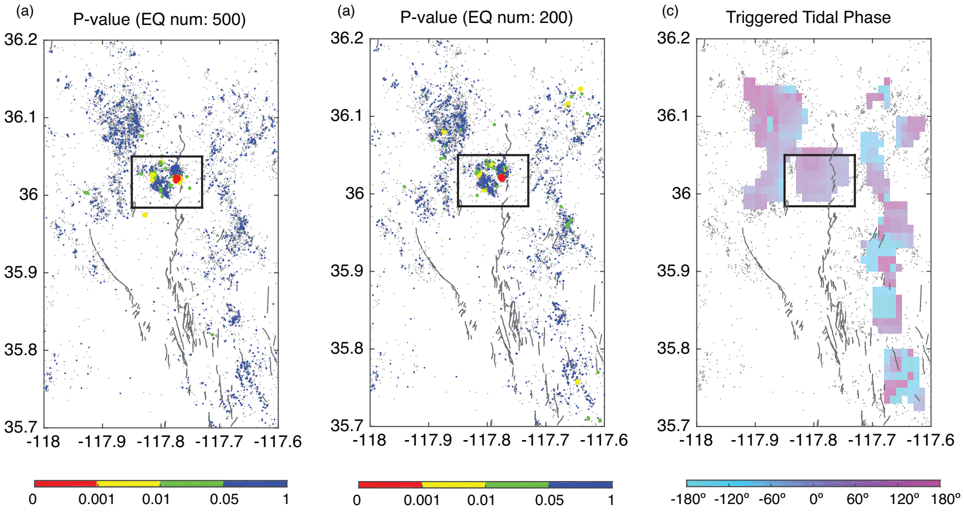

Figure S3.4: The p-value distributions of 2000 clusters from one randomly picked event and its closest 500 and 200 events and the triggering tidal phases for the events in 0.02° by 0.02° grids with 0.01° shifts.

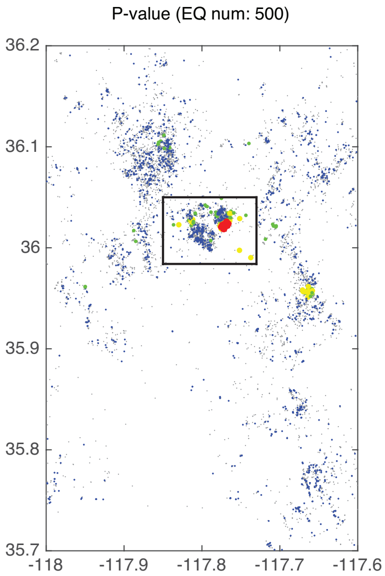

Figure S3.5: An Example of p-value distributions of 2000 randomly picked clusters from one event and its closest 500 and 200 events from a random 5 years of data.

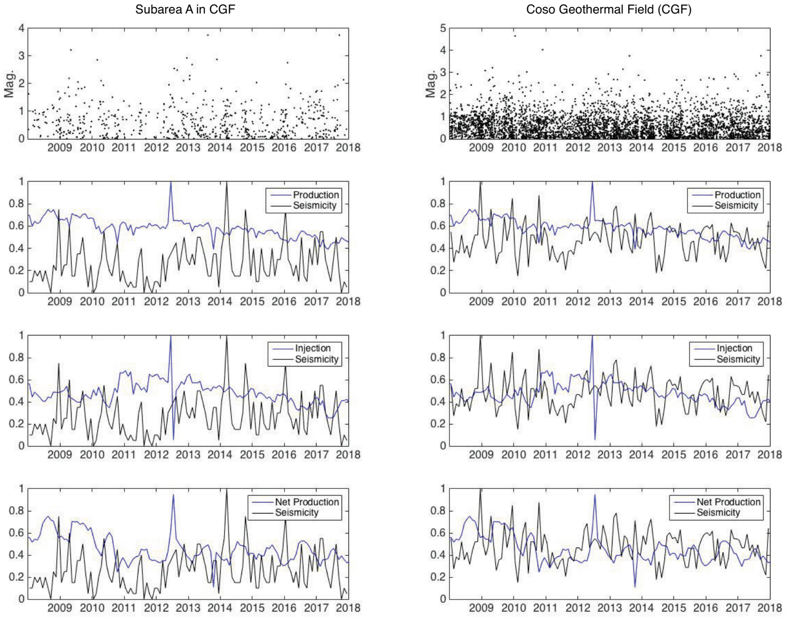

Figure S3.6: Comparison of declustered seismicity rate and production, injection and net production rate. The seismicity, production, injection, and net projection are normalized by their maximum values.

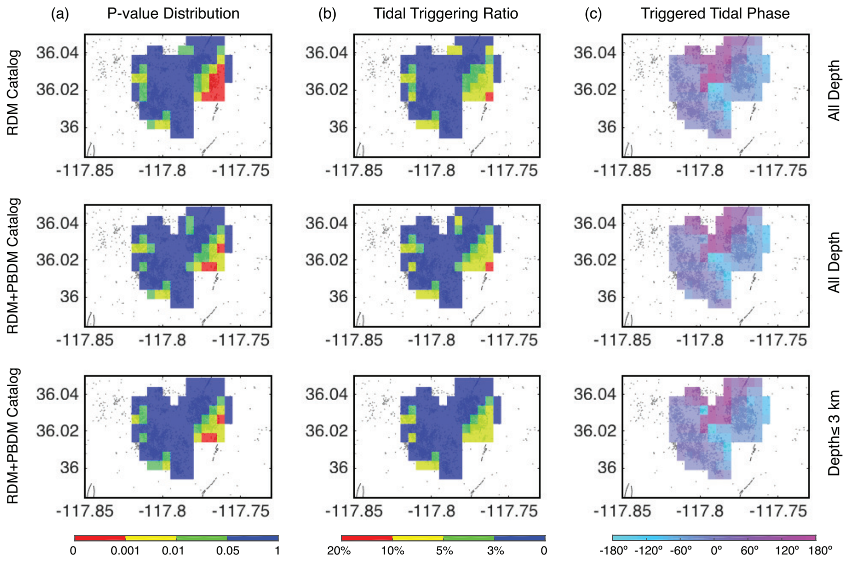

Figure S3.7: Maps of p-values, tidal triggering ratios and triggered tidal phases similar to Figure 3. The tidal phases in this plot are computed using the tidal height, rather than dilatational strain.

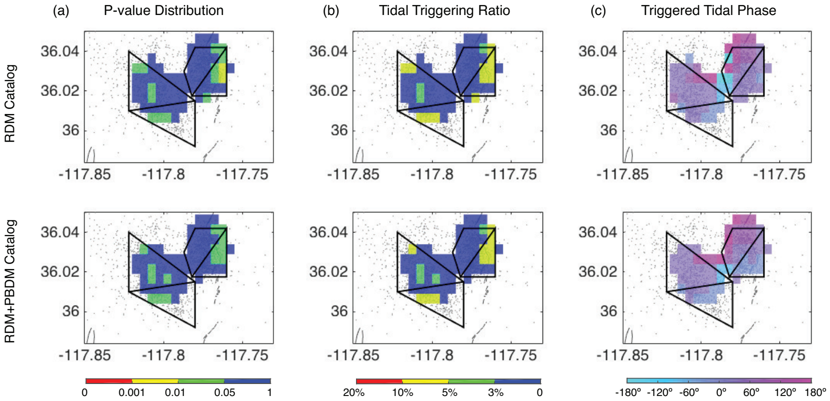

Figure S3.8: Maps of p-values, tidal triggering ratios and triggered tidal phases similar to Figure 3 using the SCSN catalog with complete magnitude 0.5.

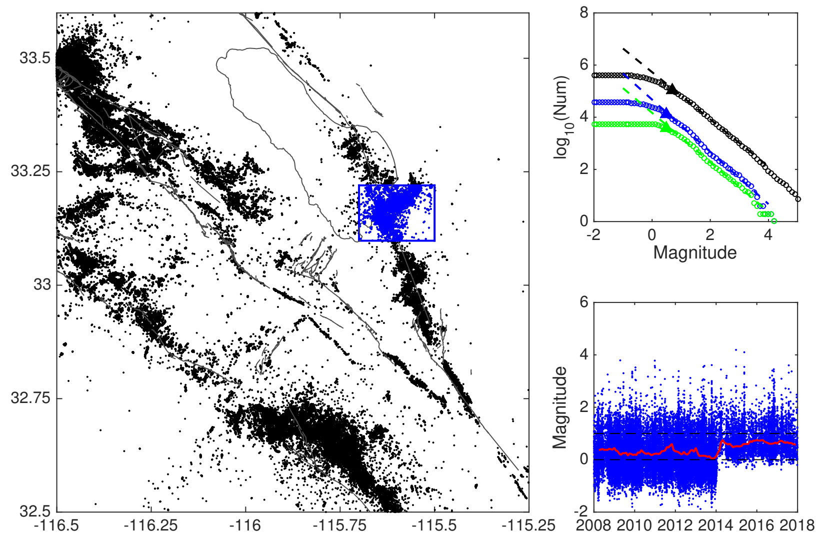

Figure S3.9: Seismicity in the Salton Sea geothermal field similar to Figure 1.

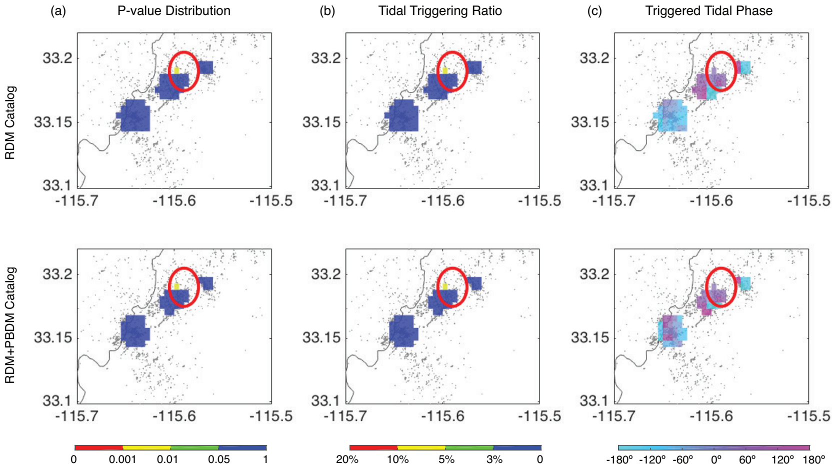

Figure S3.10: Maps of p-values, tidal triggering ratios and triggered tidal phases similar to Figure 3 for the Salton Sea geothermal region.

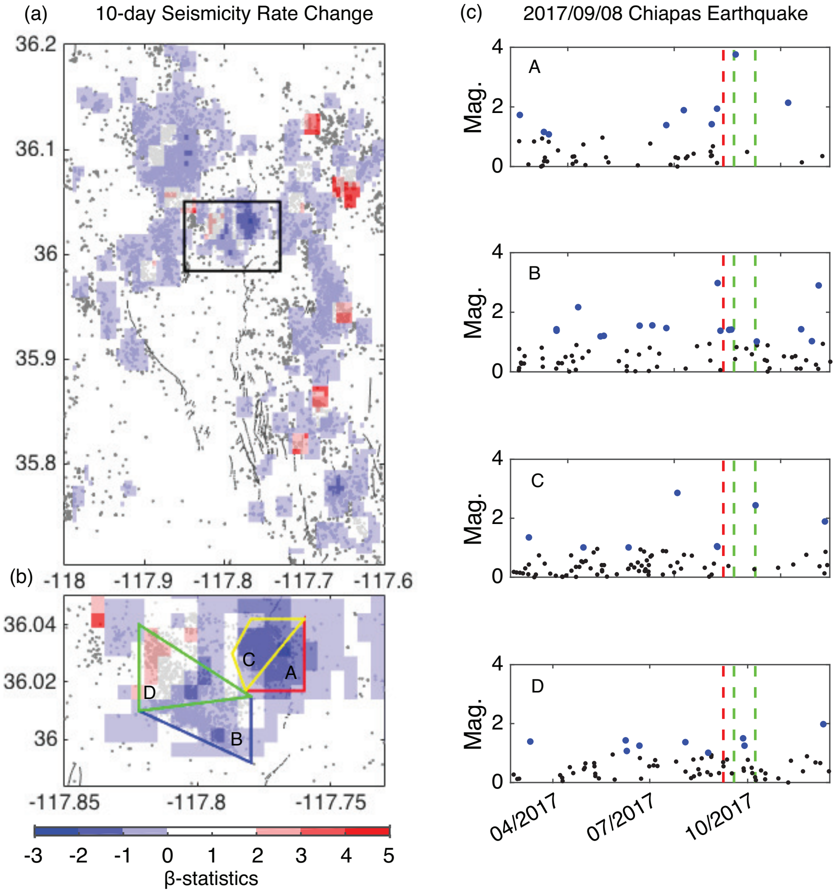

Figure S3.11: Estimates of seismicity rate changes and magnitude vs. time plots for subsets of the Coso seismicity for 2010 Gwaii earthquake.

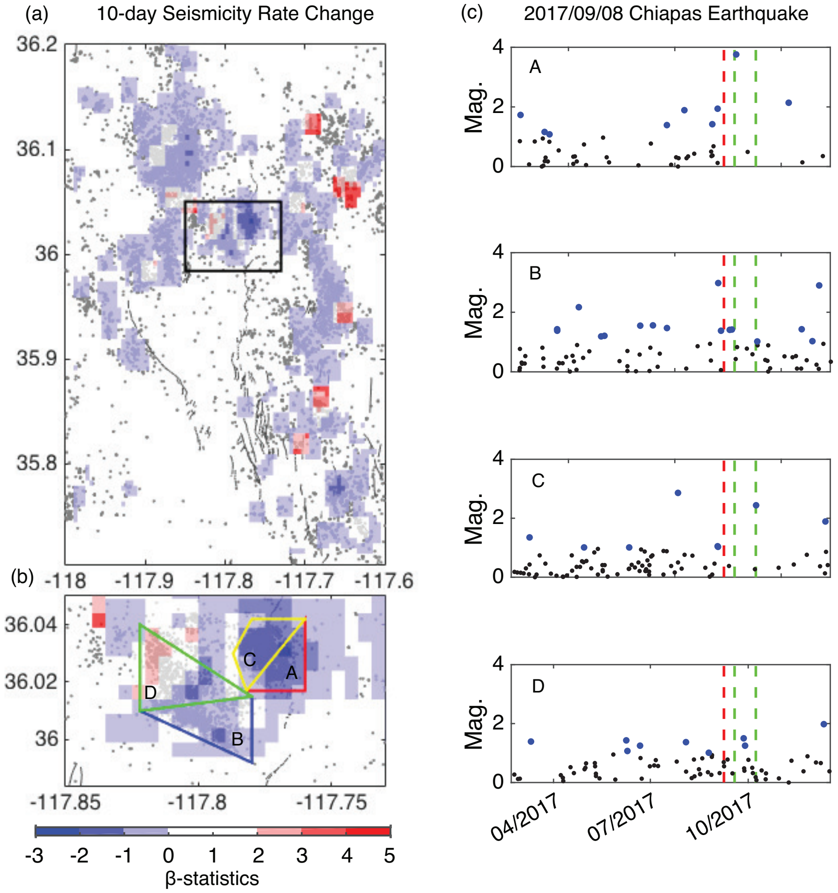

Figure S3.12: Estimates of seismicity rate changes and magnitude vs. time plots for subsets of the Coso seismicity for 2010 Gwaii earthquake.

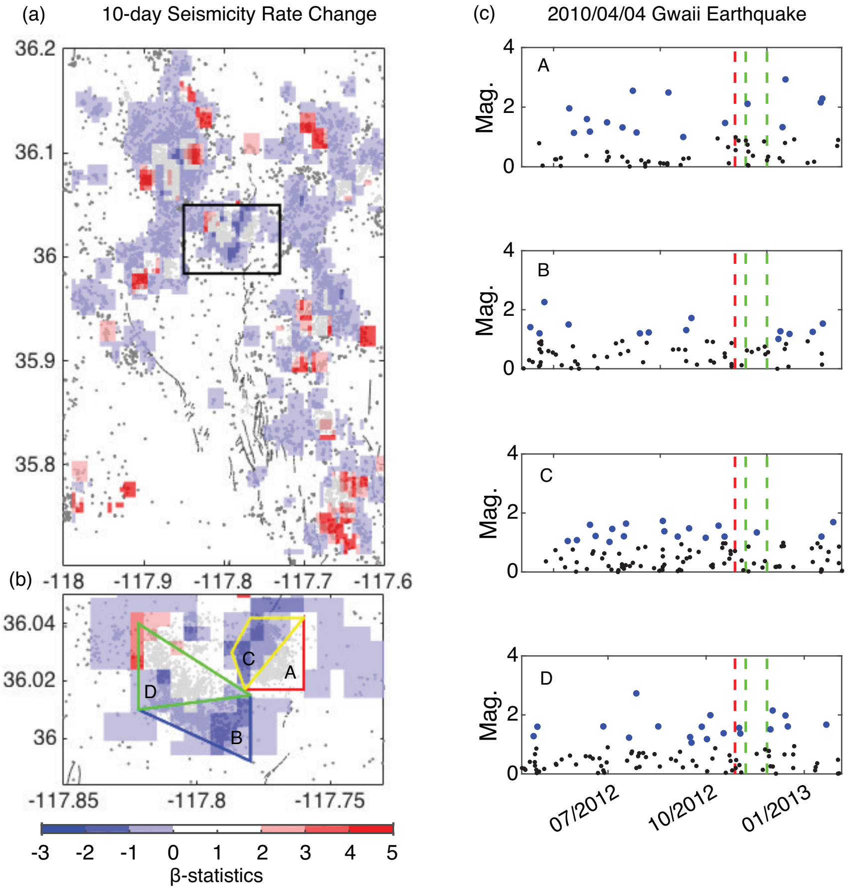

Figure S3.13: Estimates of seismicity rate changes and magnitude vs. time plots for subsets of the Coso seismicity for 2017 Chiapas earthquake.

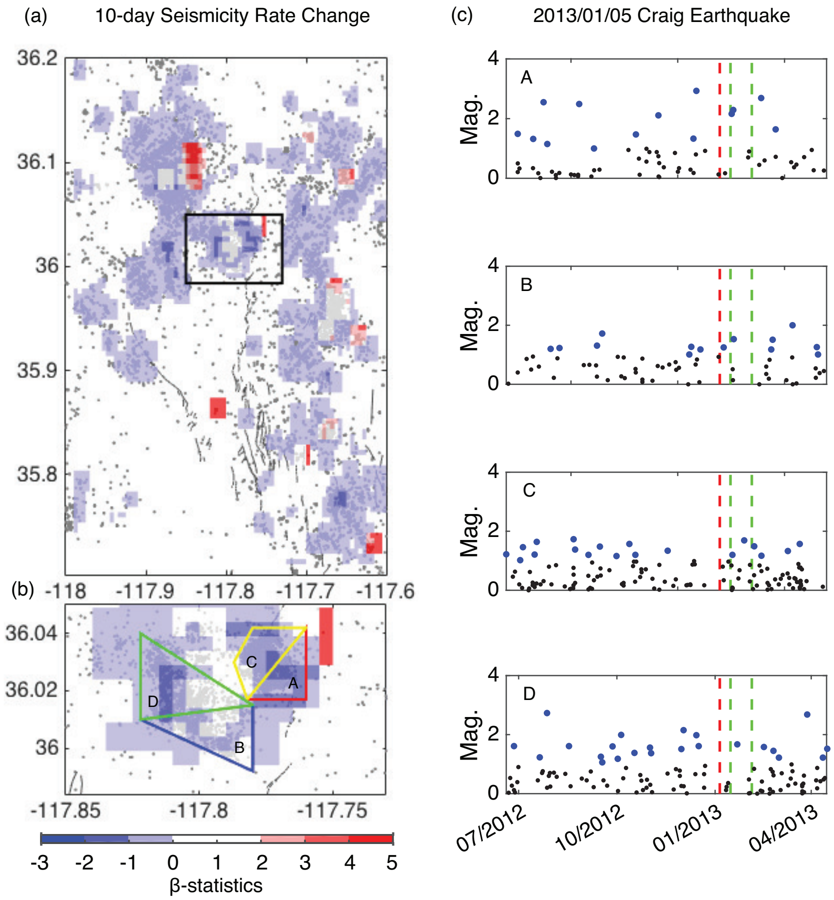

Figure S3.14: Estimates of seismicity rate changes and magnitude vs. time plots for subsets of the Coso seismicity for 2013 Craig earthquake.

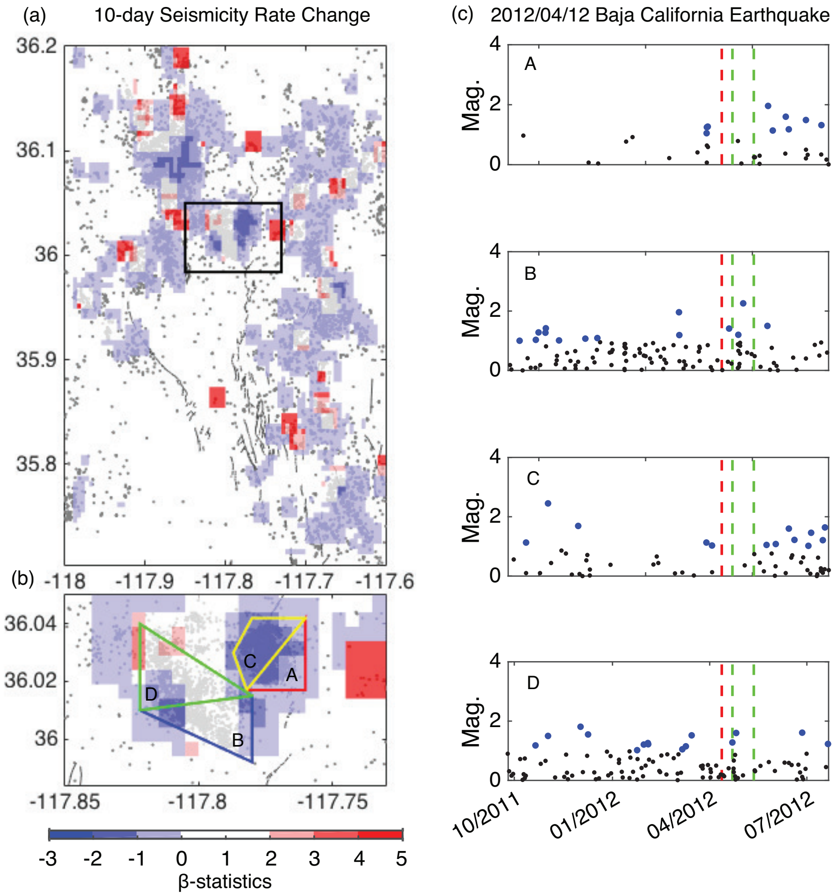

Figure S3.15: Estimates of seismicity rate changes and magnitude vs. time plots for subsets of the Coso seismicity for 2012 Baja earthquake.

Table S3.1: Earthquakes for remote triggering

Date	Time	Ms	Latitude	Longitude	Depth (km)	Location
2010/04/04	22:40:43.0	7.3	32.30°	-115.27°	6.0	El Mayor-Cucapah, Mexico
2012/04/12	07:15:48.5	7.0	28.70°	-113.10°	13.0	Baja California, Mexico
2012/10/28	03:04:08.8	7.8	52.79°	-132.10°	6.0	Gwaii, Haida
2013/01/05	08:58:19.3	7.7	55.39°	-134.65°	6.0	Craig, US
2017/09/08	04:49:19.2	8.2	15.02°	-93.90°	6.0	Chiapas, Mexico

Chapter 4

Using direct and coda wave envelopes to resolve the scattering and intrinsic attenuation structure of Southern California

Characterizing scattering and absorbing properties and the power spectrum of crustal heterogeneity is a fundamental problem for informing strong ground motion estimates at high frequencies, where scattering and attenuation effects are critical. We perform a comprehensive study of local earthquake coda waves in southern California to constrain scattering and intrinsic attenuation structure. We analyze data from 1195 spatially distributed earthquakes from 1981–2013 at source depths of 10 to 15 km and epicentral distances from 0–250 km with magnitudes larger than 1.8. We stack envelope functions from 28,127 vertical-component and 27,521 transverse-component seismograms, filtered from 2 to 4 Hz. We model these observations using a particle-based Monte Carlo algorithm that includes intrinsic attenuation as well as both P- and S-wave scattering and both single and multiple scattering events. We find that spatially averaged coda-wave behavior for southern California can be explained only with models containing an increase in scattering strength and intrinsic attenuation within the uppermost crust, i.e., they are poorly fit with half-space models of constant scattering strength. A reasonable fit to our data is obtained with a two-layer model, composed of a shallow crustal layer with strong wide-angle scattering and high P and S intrinsic attenuation and a deeper layer with weaker scattering and lower intrinsic attenuation (top 5.5 km: ${}^{\alpha}Q_I = 250$, ${}^{\beta}Q_I = 125$, heterogeneity correlation length $a = 50$ m, fractional velocity heterogeneity $\varepsilon = 0.4$; lower crust: ${}^{\alpha}Q_I = 900$, ${}^{\beta}Q_I = 400$, $a = 2$ km, $\varepsilon = 0.05$).

4.1 Introduction

The seismic coda is a tail of scattered waves that follows direct arrivals in a seismogram. Since the pioneering work of Aki and Chouet (1975), coda waves are known to be generated by random heterogeneity in the Earth. In the ensuing decades, researchers have conducted a wide variety of observational, theoretical and numerical studies of seismic coda waves and scattering processes. Although most seismic analyses of Earth structure rely on observations of the travel times and waveforms of direct seismic waves that travel along ray paths determined by Earth's large-scale velocity structure, coda waves, containing seismic energy scattered by smaller-scale velocity or density perturbations, can be used to interpret high-frequency seismic signals. In particular, the temporal decay of coda wave amplitudes provides important information about scattering strength and attenuation.

Since Aki (1969) first interpreted coda waves using a single-scattering model, many methods have been developed to relate seismic attenuation to coda wave properties. Attenuation is characterized by the quality factor Q, whose reciprocal is the fractional energy loss per cycle of the passing wave. Attenuation is caused by two factors: scattering and anelastic phenomena and the total attenuation Q can be expressed as $Q^{-1} = Q_I^{-1} + Q_{Sc}^{-1}$, where Q_I and Q_{Sc} are the intrinsic and scattering attenuation, respectively. Separating and determining the effects of scattering and intrinsic attenuation has been of interest to seismologists for many years (e.g. Wu, 1985; Frankel and Wennerberg, 1987; Wu and Aki, 1988; Hoshiba, 1991; Fehler et al., 1992; Carcolé and Sato, 2010). Local and regional seismic attenuation structure is an important input for many seismic applications and provides information to understand lithospheric properties and tectonics. Attenuation is also a key input parameter for strong ground motion estimates and magnitude versus yield relations for nuclear explosion monitoring.

Radiative transfer theory (RTT) is a widely used approach to model and separate the effects of intrinsic and scattering attenuation. Based on RTT, Wu (1985) introduced a method for determining both intrinsic and scattering attenuation, and Wu and Aki (1988) applied this approach to estimate attenuation in the Hindu Kush region. The Monte Carlo method was introduced by Gusev and Abubakirov (1987) and Hoshiba (1991) to numerically solve the radiative transfer equation and simulate the temporal shape of the coda envelope function. Based on this approach, Fehler et al. (1992) developed the Multiple Lapse Time Window Analysis (MLTWA) method to study attenuation in the Kanto-Tokai region. In the following decades, the Monte Carlo approach has been widely used to study scattering and attenuation structures throughout the Earth (e.g. Margerin and Nolet, 2003a,b; Shearer and Earle, 2004; **?**; Mancinelli et al., 2016). The MLTWA method has also been employed to study intrinsic and scattering attenuation structure in different regions (e.g. Fehler et al., 1992; Bianco et al., 2002; Lee et al., 2010; Carcolé and Sato, 2010). Other recent studies have adopted RTT to resolve attenuation, especially scattering attenuation, in the crust (Przybilla et al., 2006, 2009); in a volcanic region (Yamamoto and Sato, 2010). Non-isotropic scattering and conversion scattering between P and S waves can be readily accommodated in Monte Carlo RTT simulations (Przybilla et al., 2006, 2009) and the mode conversion and multiple scattering should be included to describe the seismic energy propagation in the volcanic environments (Yamamoto and Sato, 2010).

Another approach considers coda attenuation Q_C instead of intrinsic and scattering attenuation (i.e., the coda-Q method). The coda energy decay can be expressed as

$$E(t,f) = S(f)t^{-\alpha}e^{-2\pi ft/Q_C(f)} \tag{4.1}$$

where E is the power spectrum, S is a frequency-dependent source term, t is the lapse time, f is the frequency, α is a positive constant that is related to wave type (Aki and Chouet, 1975), and Q_C is the coda quality factor. The frequency-dependent Q_C depends on both scattering and anelastic absorption structure. In particular, at long lapse times, when coda waves are in the diffusive regime, Q_C asymptotically approaches the intrinsic Q in a uniform half-space model (Shapiro et al., 2000). This method provides another important parameter to measure and many studies have mapped coda attenuation variations in different regions (e.g. Jin and Aki, 2005; Mukhopadhyay and Tyagi, 2008; Calvet and Margerin, 2013).

Southern California is one of the most well-studied seismically active regions in the world. For use in seismic hazard estimation, there are a variety of seismic attenuation models in southern California obtained by different methods (Frankel et al., 1990; Aki, 1996; Raoof et al., 1999; Hauksson and Shearer, 2006). Our goal in this study is to obtain spatially averaged high-frequency full-waveform envelope functions and apply modeling to resolve the depth dependence of scattering and intrinsic attenuation in southern California. We consider both vertical- and transverse-component seismograms at a range of source-receiver distances, stack and average the waveform envelope functions, which include direct P and S waves and their codas. We then apply a Monte Carlo, particle-based method to forward model the envelope functions at different distances. This method includes multiple non-isotropic scattering, conversions between P and S waves and intrinsic attenuation, and is based on a realistic 1-D velocity model that yields accurate P and S arrival times as well as Moho reflections. We obtain good fits to the data stacks with a two-layer model of intrinsic attenuation and scattering properties.

4.2 Dataset

We select local events from a relocated catalog Yang et al. (2012) from 1981 to 2013 and download waveform data using the Seismogram Transfer Program (STP) available from the Southern California Earthquake Center (SCEC).

We use four criteria to select the seismic data:

1) To ensure good signal-to-noise ratios even at large epicentral distances, we only use events with magnitudes larger than 1.8. This criterion is to guarantee that the signal-to-noise ratio is high enough to characterize the seismic signals and coda wave decay. The seismic signals from these events are generally recorded by multiple stations at a variety of azimuths, which helps average out any focal mechanism effects.

2) We only select events at depths from 10 km to 15 km. This minimizes complications due to strong scattering and lateral heterogeneity in the shallow crust and simplifies our modeling by ensuring that travel times are approximately only a function of distance.

3) Since we want both vertical and transverse component records for our comparisons to synthetics, we only use data from three-component stations.

4) Since our focus is on high frequencies, we only use the short period (EH) and broadband (BH, HH) seismic channels.

Figure 4.1 shows the distribution of events and stations. To get a more uniform distribution of sources than the original catalog, we apply the following criteria: First, we divide the catalog into 0.1° wide cells. In each spatial cell, we keep all the events with magnitudes larger than 4.0. For events with magnitudes between 1.8 and 4.0, we separate the events into bins of 0.2 in magnitude. In each magnitude bin, we select a single representative event, the one recorded by the most stations. We store the waveforms using a -5 to 200 s window relative to the P arrival to capture the entire waveform, including Moho reflections and the S coda.

All clipped seismograms are discarded. Waveform clipping is caused by instrument limitations at large amplitudes, and occurs most often when the epicentral distance is small and/or the event magnitude is large (e.g. Yang and Ben-Zion, 2010). We use a simple algorithm to detect the clipped waveforms. The basic idea is to check whether waveform peaks and troughs have nearly the same value when they approach the extreme values of the traces. Within a 3-s window centered on the maximum absolute value point, we find the values for the 10 highest peaks and 10 lowest troughs. We then compute the mean and standard deviation (SD) of the peak and trough values respectively. If the SD-to-mean ratio is less than 0.06, we discard the seismogram as probably clipped (the 0.06 value was determined empirically for our dataset from visual inspection of seismograms). In total, we flagged 2160 vertical components and 1217 horizontal components as clipped.

4.3 Data Processing and Methodology

4.3.1 Data Processing

At local and regional scales, seismic records vary considerably among different source-receiver paths, especially at high frequencies. These differences contain valuable information about lateral variations in velocity structure, attenuation, and scattering, but greatly complicate data presentation and modeling efforts. Here we focus on a simpler problem: generating a laterally averaged model of the average wavefield properties of direct and coda waves in southern California, which we then attempt to simulate using a model with properties that vary only with depth.

To process the data, we adopt the envelope-stacking method (e.g. Hedlin et al., 1997; Shearer and Earle, 2008). Unlike conventional seismogram-stacking methods, this approach discards phase information and only considers the energy in the seismograms. It is well suited for coda-wave analysis because it does not require waveform coherence among the traces. By stacking many records, we can improve the signal-to-noise ratio as well as average the energy radiated from different focal mechanisms, which simplifies the modeling by allowing us to ignore the source focal mechanism. This method has been successfully adopted to interpret PKP and PKKP precursors (Hedlin et al., 1997; Shearer et al., 1998; Mancinelli and Shearer, 2013) and P coda (Shearer and Earle, 2004).

Before stacking, the seismograms are filtered at 2–4 Hz with a zero-phase, fourth-order Butterworth filter and the envelope function is calculated. For each trace we estimate the noise level from a 3-s time window before the P-wave arrival and the coda level from a 3-s time window starting at twice the S-wave travel time. We require that the coda level be at least three times larger than the noise level. We apply a noise correction by assuming that the noise is uncorrelated to the signal, so that we can remove the noise energy from each trace. Before stacking, we normalize the traces to their maximum amplitude in order to uniformly weight seismograms from events of varying sizes. Because the peak amplitude may be less stable than time-averaged amplitude measures, we also experimented with normalizing each trace to the average amplitude in a 3-s time window centered on the peak amplitude. However, this alternate normalization led to negligible differences in the final data stacks, so for simplicity we use the peak amplitude normalization here. All the traces are aligned on the P-wave arrival and binned at 10-km intervals in epicentral distance. These processes are applied to seismic signals from both vertical (V) and transverse (T) components within 250-km epicentral distance. Note that surface waves are of minor importance in our data set because of the deep sources (10 to 15 km), limited distance range and relatively high frequencies (2 to 4 Hz).

Figure 4.2 (a) and (d) shows the stacked envelopes aligned on the P-wave arrival, which is set to zero time. The V component stack clearly shows the direct P and S arrivals with coda waves that decay with time. At distances beyond 200 km, the stacked envelopes are not as smooth as at shorter distances, owing to fewer contributing seismograms. Compared to the V components, the T components have a relatively larger S/P peak energy ratio, since the S waves have higher amplitudes on the horizontal components and the P-wave energy is relatively weak.

The stacking process does not include the absolute amplitude versus distance information, which was removed by the amplitude normalization applied to the envelopes prior to stacking. To consider this, we adopt the coda normalization method to compute the absolute amplitudes. The basic idea is to use the coda wave at a fixed lapse time as a reference to calibrate the amplitudes of the direct P and S waves. The peak amplitude of the direct wave, $A_{ij}^{D}(f,r)$ can be expressed as (Yoshimoto et al., 1993),

$$A_{ij}^{D}(f,t) = I_{\theta\phi} r^{-\gamma} \exp\left[-\frac{\pi f}{Q(f)V} r\right] S_i(f) R_j(f) \tag{4.2}$$

where $I_{\theta\phi}$ is the source radiation pattern, r is the hypocentral distance, γ denotes the geometrical spreading exponent, S_i is the i-the source spectral amplitude, R_j describes the site effect of j-th receiver, V indicates the average wave velocity, and Q is the average attenuation. In the logarithm domain, we assume the peak amplitude is the summation of three terms:

$$\log(A_{ij}^{D}(f,t)) = \log(S_i(f)) + \log(R_j(f)) + \log(D_k(f,r)) \tag{4.3}$$

where D_k is equal to $I_{\theta\phi} r^{-\gamma} \exp\left[-\frac{\pi f}{Q(f)V} r\right]$, which means the ray path term contains the radiation pattern, geometrical spreading and propagation attenuation. Because our stacking approach averages lateral variations and source radiation pattern effects in the observations, the ray path term $D(f,r)$ is only a function of distance. The coda amplitude in the logarithm domain can be expressed as (Aki and Chouet, 1975)

$$\log(A_{ij}^{C}(f,t)) = \log(S_i(f)) + \log(R_j(f)) - \alpha \log(t) - \frac{-\pi f t}{Q_C(f)} \tag{4.4}$$

where the $Q_C(f)$ is the frequency-dependent coda attenuation. The lapse time should be long enough to guarantee that the coda waves average the media variations and source radiation pattern effects. Comparing equation (3) and (4) and reordering the terms, we also have

$$\log[\frac{A_{ij}^{D}(f)r^{\gamma}}{A_{ij}^{C}(f,t)}] = C(f,r) \tag{4.5}$$

where the constant $C(f,r)$ is a function of distance and frequency based on our stacking approach. Here we assume the geometrical spreading exponent $\gamma = 1$.

We used the coda normalization method to process the P- and S-wave amplitude of each vertical peak component and the S-wave peak amplitude of the transverse component. A 3-s time window starting from the P-wave arrival is used to measure the average P-wave amplitude from the envelope functions. For the S waves, we search for the peak amplitude within ±5 s around the predicted S-arrival time and use a 3-s window centered on the maximum value point to measure the average S-wave amplitude. To estimate the coda wave amplitude, we use a 5-s time window starting at lapse time 60 s for epicentral distances smaller than 100 km and 110 s for epicentral distances larger than 100 km to ensure the lapse time is larger than twice the S-wave travel time. Since the results of $\log_{10}[\frac{A_{ij}^{D}(f)r^{\gamma}}{A_{ij}^{C}(f,t)}]$ from observations are rather scattered, we compute the median value in each 5 km bin in epicentral distance. Figure 4.2 (b) and (e) illustrate that the S-wave amplitudes gradually decrease with epicentral distance. It is noted that we compute the coda-normalized peak amplitude using the hypocentral distance, but plot the results versus epicentral distance. The jump of peak amplitudes at epicentral distance 100 km is caused by the reference coda time window change at this distance.

4.3.2 Monte Carlo simulation

Monte Carlo simulation is a versatile and powerful approach for simulating scattering in complex models. Gusev and Abubakirov (1987) first introduced the Monte Carlo method in seismology to model S-wave scattering in a uniform whole space. Later work adopting this approach is described by Hoshiba (1991, 1994, 1997), Margerin and Michel Capillo Van Tiggelen

(2000), Yoshimoto (2000), Margerin and Nolet (2003a,b), and Shearer and Earle (2004). Although there are some differences among applications of Monte Carlo methods, the basic idea of each algorithm is similar. The source is modeled as spraying millions of seismic energy particles, which can be tracked through the seismic velocity model using ray theory. The particles are continuously subject to a scattering probability and tested for possible scattering events by using a random number generator. During its propagation, the energy carried by each particle is reduced by any intrinsic attenuation. Finally, the particles that reach the surface are counted and summed in time-range bins as the total energy flux. To compare more directly with seismic records, the energy carried by the particles may be decomposed into three components (vertical, transverse, radial) based on the ray incidence angle. At the end of the calculation, all the time-range bins can be converted to envelope functions to compare with real data. The Monte Carlo approach obeys energy conservation and multiple scattering and geometric spreading effects are naturally obtained.

Here, based on Shearer and Earle's (2004) early work on modeling teleseismic P coda, we develop a flexible Monte Carlo code that can be applied to simulations at different scales, in particular to local and regional scattering problems. For such efforts, our algorithm has the advantage of modeling P- and S-coda waves simultaneously, furthermore, it can constrain the intrinsic and scattering attenuation for both P- and S waves, compared to some other methods such as the multiple-lapse-time-window approach (MLTWA) (Fehler et al., 1992); coda normalization method (Yoshimoto et al., 1993) and the coda-Q method (Hiramatsu et al., 2000), which only compute or invert P- or S-wave attenuation separately. In addition, the Monte Carlo method can handle realistic depth-dependent models, which can take into account the free surface, velocity gradients in the crust, and the presence of the Moho discontinuity.

In a Monte Carlo simulation, the scattering probabilities and scattering angles can be computed based on theoretical results for random heterogeneity models. The scattering strength can be described as the mean free path (Sato et al., 2012). On the computer, this can be simulated by testing whether the ray path length of the particle exceeds a random length, obtained for each particle and scattering volume by randomly sampling an exponential distribution based on the mean free path. When a scattering event occurs, the scattering angle is again randomly determined based on a physical model of the scattering medium. As in many previous studies, we define the random medium using just two parameters, the correlation distance, a, and the root-mean-square (RMS) fractional velocity fluctuation, ε. The scattering heterogeneity in the medium can be statistically parameterized by the von Karman autocorrelation function (ACF) (Sato et al., 2012, p. 23).

$$R(r) = \frac{\varepsilon^2 2^{(1-\kappa)}}{\Gamma(\kappa)} (\frac{r}{a})^{\kappa} K_{\kappa}(\frac{r}{a}) \tag{4.6}$$

where r is the lag distance, a is the correlation distance, ε is the RMS fractional velocity fluctuation, Γ is the gamma function and K_κ is the modified Bessel function of the second kind of order κ. The 3-D Fourier transform of equation (6) gives the 3-D power spectral density function (PSDF) (Sato et al., 2012, p. 23).

$$P(m) = \frac{2\pi^{3/2}\Gamma(\kappa+3/2)\varepsilon^2 a^3}{\Gamma(\kappa)(1+a^2m^2)^{k+3/2}} \tag{4.7}$$

where m is absolute value of the wave number and κ controls the relative proportion of large and small scale heterogeneity. The P- to S-wave velocity ratio is assumed to be $\sqrt{3}$, i.e., a Poisson solid, and the fractional P- and S-wave velocity fluctuations are assumed equal. The density/velocity perturbation scaling factor is 0.8, which is estimated for the lithosphere from Birch's Law (Sato et al., 2012). Increasing this value will generally cause more back-scattering. We assume a Bessel function order number κ of 0.3 for the simulation, which is within the range of 0.0–0.5 used to describe crustal heterogeneity in previous studies (Frankel and Clayton, 1986; Przybilla et al., 2009; Bydlon and Dunham, 2015; Savran and Olsen, 2016).

Shearer and Earle (2008) described the Monte Carlo approach in some detail. We note a few key points here. For efficiency, we pre-compute a large table of ray paths for both P and S waves based on the velocity model for thousands of ray parameters. The energy particle's trajectories can then be estimated from this table without performing any ray tracing during the main calculation. Similarly the reflection and transmission coefficients at each interface are pre-computed at the same ray parameter values. When a particle hits an interface, a random number is generated to compare with these coefficients to determine the behavior of this particle, i.e., whether it is reflected or transmitted and/or converts from P to S, etc. S-wave polarities are accounted for by tracking the SH/SV energy ratio. Distinct from the whole Earth case, for regional models we define a maximum possible depth and ignore any particles that exceed this depth. In this study, we do not model the Pn and Sn waves, since within this epicentral distance range, their amplitudes are small compared to the direct P and S waves.

For our simulations, we assume a single point source at 13 km depth (our data stacks are for events from 10 to 15 km depth). We assume an isotropic source, i.e., we do not consider radiation pattern effects. We spray equal numbers of P-wave and S-wave particles, while setting the S-wave particle energy to 14 times the P-wave particle energy, within the range of 9 to 17 observed in studies of P- and S-wave corner frequency (see Boatwright and Fletcher, 1984; Abercrombie, 1995). Note that this is less than the theoretical ratio of 23.4 for a Poisson solid and double-couple source with identical P- and S-wave corner frequencies. The initial polarity of the S wave is randomly assigned. Because each simulation takes several hours to run and our models contain many free parameters, we do not attempt a formal inversion. Instead, our results are derived from trial-and-error forward modeling in an effort to find model parameters that produce a reasonable fit to the observed data stacks.

4.4 Results

We assume a smoothed version of a classic 1-D southern California velocity model shown in Figure 4.4a (Hadley and Kanamori, 1977) for ray tracing. This model features a strong velocity gradient in the upper crust (0–5.5 km), a weak velocity gradient in the lower crust (5.5–32 km) and an upper mantle Pn velocity of 7.80 km/s.

We first attempted to fit our observations (i.e., the direct phase and coda wave envelope stacks, including the range dependence of their absolute amplitudes), with uniform scattering and intrinsic attenuation properties, i.e., a half-space scattering and attenuation model (combined with the 1-D velocity model), and experimented with a variety of parameter choices. However, we found that none of these uniform models could explain the time and range dependence of the coda amplitudes seen in our data stacks. The problem is that relatively strong scattering (resulting from strong heterogeneity, $\varepsilon = 0.4, a = 50$ m) and intrinsic attenuation ($Q_P = 250, Q_S = 150$) is required to explain the coda amplitude and decay at short epicentral distances, but such strong scattering will over-predict coda amplitudes at long distances. Similarly, relatively weak scattering (related to weaker heterogeneity, $\varepsilon = 0.05, a = 1.5$ km, $Q_P = 800, Q_S = 200$) will fit the coda at long distances, but will under-predict coda amplitudes at short distances. This is illustrated in Figure 4.3, which compares transverse-component data stacks with predictions for half-space models tuned to fit the short and long range data, respectively. Although there are a number of free parameters in our model (e.g., ε and a, which determine scattering strength and scattering angle; Q_P and Q_S, which set intrinsic attenuation), we have experimented with enough models that we are confident that the data stacks cannot be fit over their entire time and distance range with uniform scattering and attenuation properties.

Our preferred model (see Figure 4.4b and in Table 4.1), based on fitting both the envelope shapes and their absolute amplitude versus distance, contains two layers, a shallow crustal layer with strong wide-angle scattering and high intrinsic attenuation and a deeper layer with weaker scattering and lower intrinsic attenuation. We do not claim that this model is unique and it is likely that alternate models (e.g., with more layers or with gradients in properties) exist that could provide equal or better fits. However, to fit the data these models will almost certainly also have stronger scattering and intrinsic attenuation in the uppermost crust than in the mid to lower crust. The existence of strong scattering and attenuation at shallow depths has also been noted in some previous studies (e.g. Anderson and Hough, 1984; Abercrombie, 1995; Chandler et al., 2006; Hauksson and Shearer, 2006) and the Hauksson and Shearer (2006) Q model for southern California has greatly increased attenuation within the top few kilometers of the crust.

The properties of our preferred two-layered attenuation model are shown in Figure 4b and Table 4.1 and the predictions of this model are compared to the data stacks in Figure 4.4c. At the scale of this plot, the fits appear good, but it is hard to compare the small amplitude signals at long times. To better show the fit over the entire amplitude scale, Figure 4.5 shows a comparison in log amplitude. In this case, the synthetics are seen to underpredict the data stacks at long times for some of the closest range bins. This plot also makes clear that synthetics underpredict the P amplitude observed on the transverse component stacks, although this mismatch occurs at relatively low amplitude compared to other parts of the coda envelopes (see Fig. 4.4c). Because we achieve a reasonably good fit to the P wavetrain on the vertical component, this suggests that the P-wave transverse-to-vertical energy ratio in the real data is greater than in our synthetics. One possible explanation is that large-scale 3D velocity structure in southern California causes some bending of ray paths out of the vertical plane that defines P/SV arrivals in 1-D models, but we have not yet attempted to test this idea.

However, these comparisons do not include absolute amplitude information, since that information has been removed by the amplitude normalization applied to the envelopes prior to stacking. To show this, we separately process the P- and S-wave peak amplitude of the vertical components and the S-wave peak amplitude of the transverse components using the coda normalization method in the Data Processing section. We compute $\log_{10}[\frac{A_{ij}^D(f)r^\gamma}{A_{ij}^C(f,t)}]$ for each observed and synthetic envelope. Since the results from observations are rather scattered, we compute the median value in each 5 km bin in epicentral distance. The comparison is shown in Figure 4.6 and the overall fit of both P- and S-wave amplitudes to the model predictions is very good within 200 km. In the next section, we will discuss possible sources for the misfits shown in Figure 4.6.

In our preferred model, the interface between the upper and lower crust is at 5.5 km, which matches the (Hadley and Kanamori, 1977) velocity model. For comparison, some southern California attenuation studies have thinner upper crustal layers, i.e., 3 km from (Abercrombie, 1995) and 4 km from (Chandler et al., 2006). We find there is a trade-off between the scattering strength of the upper crust and its thickness, i.e., thicker layers with weaker scattering could also fit the data (a similar tradeoff was noted for the stronger upper-mantle scattering layer of Shearer and Earle, 2004). In our simulations, thinner upper-crustal layers with more scattering could fit the data almost as well as our preferred model, but fits degraded notably for layers less than 3 km thick, as the strong P-wave coda and S-wave coda could not be fit simultaneously.

We selected our preferred model by finding the model with the best fit to both the waveform envelopes and their absolute amplitude decay simultaneously. In doing so, we defined a misfit measure *err* between the Monte Carlo simulations and the data using

$$err = \sum_{i=1}^{n}\sum_{i=1}^{m}\left[\log_{10}(d_i(t_j)) - \log_{10}(s_i(t_j))\right]^2 + \sum_{k=1}^{l}\left[\log_{10}([\frac{A^D_{obs} r_k}{A^C_{obs}}]) - \log_{10}([\frac{A^D_{syn} r_k}{A^C_{syn}}])\right]^2 \quad (4.8)$$

where $s_i(t_j)$ indicates the amplitude of the j-th time point for the i-th synthetic trace, $d_i(t_j)$ is the corresponding data amplitude, n is the total number of stacked envelopes, m is the total number of discrete time points for each envelope and k is the index of epicentral distance. A^D and A^C follow the rules for coda normalization. The misfit function contains two parts, the relative difference of the normalized waveform stacks between synthetics and real data and the difference in absolute amplitudes based on the coda normalization method. We use a 60 s time window starting from

5 s after the P-wave arrival to capture the main features of the P- and S-wave coda for vertical components and a 30 s time window starting from 5 s after the S-wave arrival to capture the main features of the S-wave coda for transverse components. From the trial-and-error forward modeling, our preferred model has the minimum misfit *err*.

4.4.1 Comparison to body-wave attenuation studies

The non-dimensional parameter *ak*, where *a* is the correlation length and *k* is the wavenumber, affects the directivity of scattering (Przybilla et al., 2009; Sato et al., 2012, p. 146). The scattering is primarily in the forward direction for $ak \gg 1$ and relatively more in the backward direction for $ak \ll 1$. When $ak \approx 1$, the scattering is strongest because of the similar scales of heterogeneity and seismic wavelength. However, the scattering patterns can be complicated and depend on the specific parameter choices for the heterogeneous media model.

Attenuation studies based on spectral studies of body-wave phases are sensitive to the combined effects of intrinsic and scattering attenuation, which we will term total attenuation. Generally, the total attenuation, Q_T, can be computed from $Q_T^{-1} = Q_I^{-1} + Q_{Sc}^{-1}$, where Q_I and Q_{SC} are the intrinsic and scattering attenuation, respectively. The scattering attenuation is defined by $Q_{Sc}^{-1} = g_0 v/\omega$ (Carcolé and Sato, 2010; Sato et al., 2012, p. 66), where $g_0 = l^{-1}$ is the scattering coefficient, which is the reciprocal of mean free path, ω is the angular frequency and v is the P- or S-wave velocity. The scattering coefficient is a measure of both the scattering excitation and the amplitude attenuation with distance.

In our upper-crust model, P- and S-wave *ak* are 0.14 and 0.24, respectively, resulting in wide-angle scattering. The upper-crust P- and S-wave scattering attenuation is 192 and 133 based on the mean free paths from our preferred model (see Table 4.1). Spectral analyses of direct P and S arrivals have indicated strong attenuation in the upper 3 to 4 km in southern California (Anderson and Hough, 1984; Abercrombie, 1995; Chandler et al., 2006). Abercrombie measured ${}^{\alpha}Q$ (P-wave Q) of about 27 at a borehole site and 50 at a nearby granite site. Values of ${}^{\beta}Q$ (S-wave

Q), which is measured from broadband spectral analysis, of 21, 36, and 42 were obtained by Abercrombie (1995), Chandler et al. (2006), and Anderson and Hough (1984), respectively. Our model has higher Q values (e.g. 108 for P wave and 64 for S wave), likely because it represents an average over the 5.5-km-thick upper layer and does not capture the lower Q values near the surface.

In our lower-crust model, P- and S-wave ak are equal to 5.6 and 9.7, respectively, and the scattering is mainly forward. In this case, much of the scattered energy will remain close enough to the direct arrival that it will contribute to the direct-phase amplitude in observations (Sato, 1982). Also, other effects like envelope broadening and diffraction can make the behavior of peak amplitudes much more complex (Sato and Fehler, 2016). Thus it is not appropriate to simply use the mean free path to define the scattering-attenuation contribution to direct-phase attenuation. Indeed, our lower-crust model P- and S-wave mean free paths of 21 and 7.3 km, respectively, would predict Q_{Sc} values of 59 and 36 for P- and S-waves. These are much less than Q estimates for the lower crust from body-wave studies (Jin et al., 1994; Hauksson and Shearer, 2006), even without taking into account any contribution from intrinsic attenuation. Instead, for the lower crust, it is more appropriate to use the transport mean free path (Turner, 1998; Przybilla et al., 2009) in computing the new Q^*_{Sc} when computing the total Q, because it takes into account the directionality of the scattering. The transport mean paths for P and S waves can be expressed as (Turner, 1998; Przybilla et al., 2009),

$$l_t^p = \frac{g^0_{sp} + g^0_{ss} - g^D_{ss} + g^0_{ps}}{(g^0_{ps} + g^0_{pp} - g^D_{pp})(g^0_{sp} + g^0_{ss} - g^D_{ss}) - g^D_{ps} g^D_{sp}} \tag{4.9}$$

$$l_t^s = \frac{g^0_{ps} + g^0_{pp} - g^D_{pp} + g^0_{sp}}{(g^0_{sp} + g^0_{ss} - g^D_{ss})(g^0_{ps} + g^0_{pp} - g^D_{pp}) - g^D_{ps} g^D_{sp}} \tag{4.10}$$

with

$$g_{ij}^{D} = \frac{1}{4\pi} \oint g_{ij}(\theta,\phi) \cos\theta d\Omega \tag{4.11}$$

The transport mean free paths in our lower-crust model are 202 and 191 km, for P and S waves respectively, much greater than the corresponding mean free paths, and result in the new scattering attenuation Q_{Sc}^{*} of 569 and 931 for P and S wave, respectively, where we use Q_{Sc}^{*} to avoid confusion with Q_{Sc}, which is based on the mean free path. Our Monte Carlo modeling approach was used in a previous global study of teleseismic P coda (Shearer and Earle, 2004). Their preferred model had upper-mantle scattering (0–200 km) with a = 2 km and ε = 0.055 at 1-Hz, values comparable to the lower-crust and upper-mantle scattering parameters in our study (although it should be noted that only the lower-crustal parameters are important for fitting our data). Our lower-crustal total ${}^{\alpha}Q_T$ of 349 and ${}^{\beta}Q_T$ of 280 differ from the average ${}^{\alpha}Q$ of 500 to 900 and ${}^{\beta}Q$ of 600 to 1000 estimated by Hauksson and Shearer (2006) from direct P- and S-wave spectra in southern California. In our modeling, we assumed that the intrinsic ${}^{\beta}Q_I$ and ${}^{\alpha}Q_I$ are related by ${}^{\beta}Q_I \approx (4/9)\,{}^{\alpha}Q_I$ (Knopoff, 1971), which assumes a Poissonian solid and that shear attenuation dominates over bulk attenuation ($Q_\mu \ll Q_\kappa$). In contrast, *Hauksson and Shearer* [2006] found ${}^{\beta}Q/{}^{\alpha}Q > 1$, that is, less attenuation of S waves than P waves. We cannot explain our coda data with such values. In our simulations, increasing lower crustal intrinsic ${}^{\beta}Q_I$ to 500 or decreasing ${}^{\alpha}Q_I$ to 800 produces noticeably poorer fits to the data stacks. Our results greatly prefer ${}^{\beta}Q/{}^{\alpha}Q$ ratios less than one, in which shear attenuation dominates.

Another coda-based method to estimate intrinsic and scattering attenuation is multiple lapse-time window analysis (MLTWA) (Fehler et al., 1992). This approach was applied to southern California by Jin et al. (1994), who obtained S-wave intrinsic ${}^{\beta}Q_I$ of about 200–300 and scattering ${}^{\beta}Q_{Sc}$ of 300–900 at 3 Hz. Our model contains S-wave intrinsic ${}^{\beta}Q_I$ of 125 and 400 for the upper and lower crust, respectively, and scattering ${}^{\beta}Q_{Sc}$ of 133 and 931 for the upper and lower crust respectively. Note that this implies body-wave S-wave attenuation is dominated by scattering in the upper crust, whereas lower crustal apparent attenuation is dominated by intrinsic attenuation. Similar to S waves, in our model, the P-wave scattering ${}^{\alpha}Q_{Sc}$ of 192 in the upper crust dominates over the intrinsic ${}^{\alpha}Q_{I}$ of 250 and in the lower crust the intrinsic ${}^{\alpha}Q_{I}$ of 900 is more than the scattering ${}^{\alpha}Q_{Sc}$ of 569. Considering that the MLTWA method gives the average attenuation over a station region, without taking into account any depth dependence, the Jin et al. (1994) values are roughly consistent with our results.

4.5 Discussion

Since the earthquakes and stations are not evenly distributed in southern California, we use a bootstrap technique (Efron and Tibshirani, 1994) to check the stability of the envelope-stacking results. First, we evenly divide our study region using a 5 by 5 grid, i.e., 25 cells. We randomly pick three cells and only stack the envelope records from the events in these cells. To ensure the stability of the stacks, we only use stacks containing at least 10 records. This process is independently run 30 times. For each binned distance, we estimate the standard error in the stacked envelopes from the bootstrap results. The Figure 4.7 shows the 1-σ error of our stacking results.

Overall, the fit between the real data and Monte Carlo synthetics shown above is fairly good. However, there are some details that matter in the processing. Ideally, before comparing real data with Monte Carlo simulations, the same data binning and stacking process should also be applied to the synthetic results using the epicentral distance distribution seen in the real data. Adopting this approach, we normalize each synthetic trace, multiply it by the appropriate data epicentral distance distribution coefficient and stack the results. Figure 4.8 shows there are significant differences between the resulting stacked synthetics and those for the single epicentral distances. Within each stacking bin, the P- and S-wave differential arrival times vary with epicentral distance. During the stacking process, since the envelopes are aligned to the P-wave arrivals, the S waves do not arrive at exactly the same time. As a result, the S/P amplitude ratio becomes smaller, since the S-wave energy is not summed at the same time. In addition, both P- and S- wave coda energy decays more slowly after stacking.

In the Monte Carlo simulations, we set κ in the von Karman ACF to 0.3. The parameter κ controls the relative proportion of large and small scale heterogeneity and previous studies have used $\kappa = 0$ to 0.5 to describe the crustal heterogeneity. There are two cases of special interest: $\kappa = 0$ and $\kappa = 0.5$ for an exponential model. We experimented with κ values of 0.1, 0.3, 0.5 and 1.0 and obtained misfit *err* of 24.27, 21.76, 22.68 and 25.00, respectively. As a result, our preferred value of κ is within 0.3 to 0.5. Better constraints on κ and the power spectrum of crustal heterogeneity could be obtained by examining the frequency dependence of coda properties, which will be a target of future work.

To constrain the correlation length a and the RMS fractional velocity fluctuation ε in the von Karman model, we tested a series of values around our preferred model to generate the synthetics. When we computed the Monte Carlo simulations, we set $\kappa = 0.3$ and kept the intrinsic attenuation the same as our preferred model. The misfit *err* are computed and listed in Tables 4.2 and 4.3. For the upper crust, our preferred RMS fractional velocity fluctuation ε is within 0.4 to 0.45 and the correlation length a is within 45–50 m. For the lower crust, ε is within 0.045–0.055 and a is within 1.8–2.2 km. Since the results from the Monte Carlo simulations suffer slight random perturbation around the true ones for each model run, the misfit *err* may fluctuate a little around its true value.

In Figures 4.4 and 4.5, to compare the synthetic results and real data, the P-wave arrival time is added to each trace of real data and then each trace is adjusted to match the S-wave peaks. For both the V and T components, the arrival-time differences between P and S waves show the discrepancy, especially at large distance. In ray tracing, at large distances ($>$150 km), the direct P- and S-wave travel times mainly depend on the structure of the lower crust and upper mantle where the major part of the propagating ray path is located. Our 1-D depth-dependent model may depart from the real Earth due to lateral velocity variations beneath southern California (e.g. Tape et al., 2010). These two factors likely both contribute to the travel-time discrepancy. There are double S-wave peaks in the synthetic envelopes from about 50 to 80 km in both the V and T components, which are not seen clearly in the data stacks. The secondary peaks are caused by the critically-reflected S-wave from the Moho discontinuity. In southern California, the S-wave impedance contrast may not be consistently as large as in our model for computing the synthetics. In addition, the depth of the Moho discontinuity varies across southern California. Both of these factors will tend to remove from the data stacks the second S-wave peak seen in the synthetics.

In the stacking procedure, we normalize each envelope with respect to the largest energy peak, which usually is the S-wave energy. The comparison of vertical components in Figure 4.4 shows a systematic discrepancy of the P-wave peak amplitude. In comparison to the data stacks, at small distances, our simulation has smaller amplitudes, while at large distances, the simulation shows larger amplitudes. In Figure 4.6, we compare the P- and S-wave peak amplitudes. Some discrepancies exist, especially near epicentral distance 60 km and beyond 200 km. In the Monte Carlo simulation, both the velocity and attenuation structures are 1-D depth dependent and the scattering strength is uniform within each layer. These discrepancies may be due to the influence of unmodeled 3-D variations in velocity, scattering, and/or attenuation in southern California (e.g. Aki, 1996; Hauksson and Shearer, 2006; Tape et al., 2010). It is possible that other complications in the real Earth are important, such as statistical anisotropy (e.g., different horizontal and vertical small-scale heterogeneity strength or scale length) or stronger scattering in near-source regions due to earthquakes occurring in more fractured crust. However, despite the limitations in our model, it provides a reasonable first-order approximation to the 1-D scattering and attenuation structure in the southern California crust as resolved in P and S-wave coda at 2–4 Hz. In future work, we hope to explore perturbations to this model by considering lateral variability and other factors.

In this study, the scattering coefficients for the random elastic heterogeneity in the Monte Carlo simulation are computed based on the Born Approximation, which using first-order perturbation theory. The Born Approximation assumes that the primary wavefield is unchanged and the perturbed wavefield is small (Aki and Richards, 1980, p. 742). Unlike some Born methods, our approach does account for the amplitude reduction in the primary wavefield that occurs from one or more scattering events. However, our preferred lower-crustal model RMS fractional velocity fluctuation ε is 0.4, a large value that could cause the small perturbed wavefield assumption to fail locally to describe the scattering and result in a discrepancy between the strength of the computed scattering coefficients in this study and the true ones. This problem needs to be tested by other methods. Thus, while our modeling shows that the upper crust must have much stronger scattering than in the lower crust, the exact value of ε required to produce the scattering has some uncertainty.

4.6 Conclusions

In summary, we apply an envelope-function stacking method to resolve the time and range dependence of spatially averaged direct and coda wave amplitudes at high frequencies (2–4 Hz) across southern California, including the P- and S-wave coda decay rates and their relative amplitude information. We model the data stacks using energy-conserving and multi-scattering regional Monte Carlo simulations. The synthetic results show the southern California region has depth-dependent scattering and attenuation properties and seismic observations can be reasonably fit with a two-layered model composed of a shallow crustal layer with strong wide-angle scattering and high intrinsic attenuation and a deeper layer with weaker scattering and lower intrinsic attenuation.

Acknowledgments

We thank the personnel of the USGS/Caltech Southern California Seismic Network who pick and archive the seismograms and the Southern California Earthquake Center (SCEC) for distributing the data. This research was funded by USGS grant G15AP00094 and by SCEC. The refined catalog is available at http://scedc.caltech.edu/research-tools/downloads.html. The picked arrival times and seismograms are downloaded by using the Seismogram Transfer Program (STP), which is available at http://scedc.caltech.edu/research-tools/stp-index.html. We also express our gratitude to the two anonymous reviewers for their suggestions to improve this manuscript.

Chapter 4, in full, is a reprint of the material as it appears in Journal of Geophysical Research: Solid Earth: Wang W. and Shearer P., 2017, “Using direct and coda wave envelopes to resolve the scattering and intrinsic attenuation structure of Southern California”, *Journal of Geophysical Research: Solid Earth*, 120(9), 7236-7251. The dissertation author is the primary investigator and author of this paper.

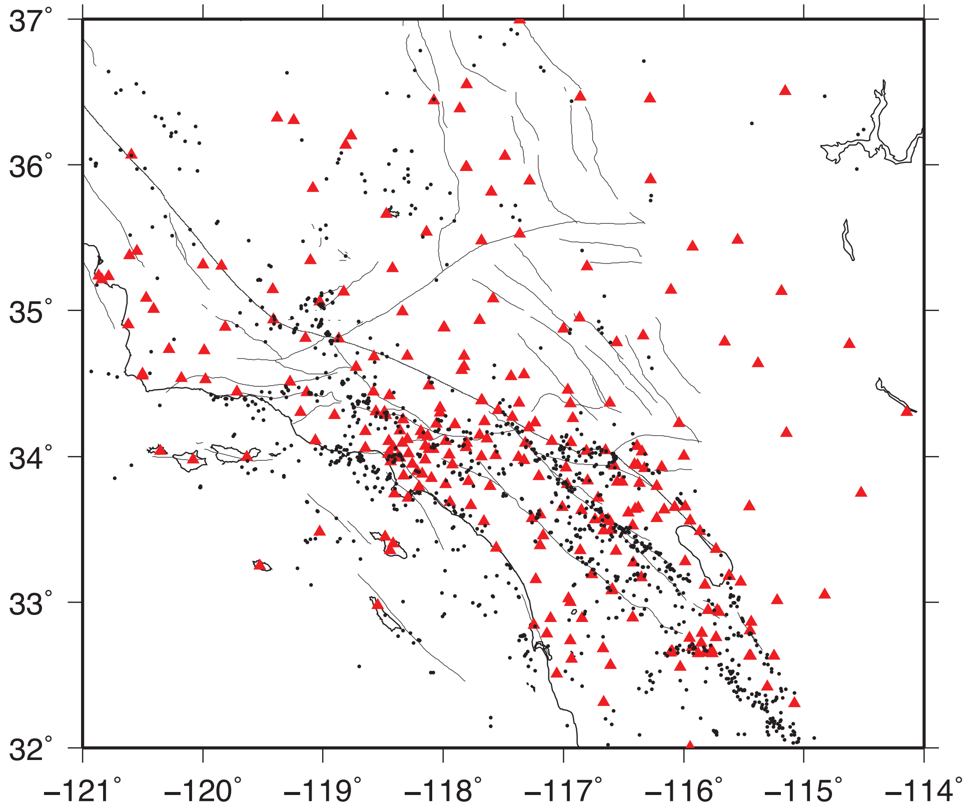

Figure 4.1: Locations of earthquakes and stations used in this study. The event epicenters are shown as black dots and the station locations are shown as red triangles. Quaternary faults are depicted as light black curves.

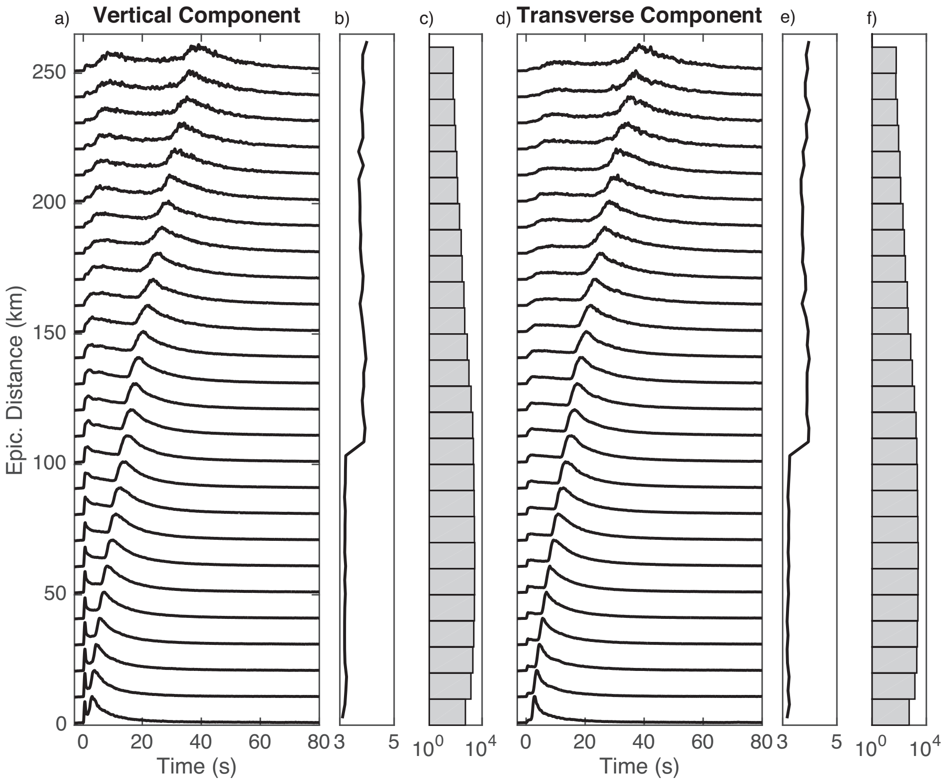

Figure 4.2: Stacked envelope functions, peak amplitudes of S waves and number of contributing traces versus epicentral distance. (a) & (d) show the stacked envelopes aligned on their P-wave arrivals, defined as zero time. (b) & (e) show the logarithmic S-wave peak amplitudes decrease with distance and the mean value is removed. The histograms in (c) & (f) show the number of traces in each stack, note the log scale.

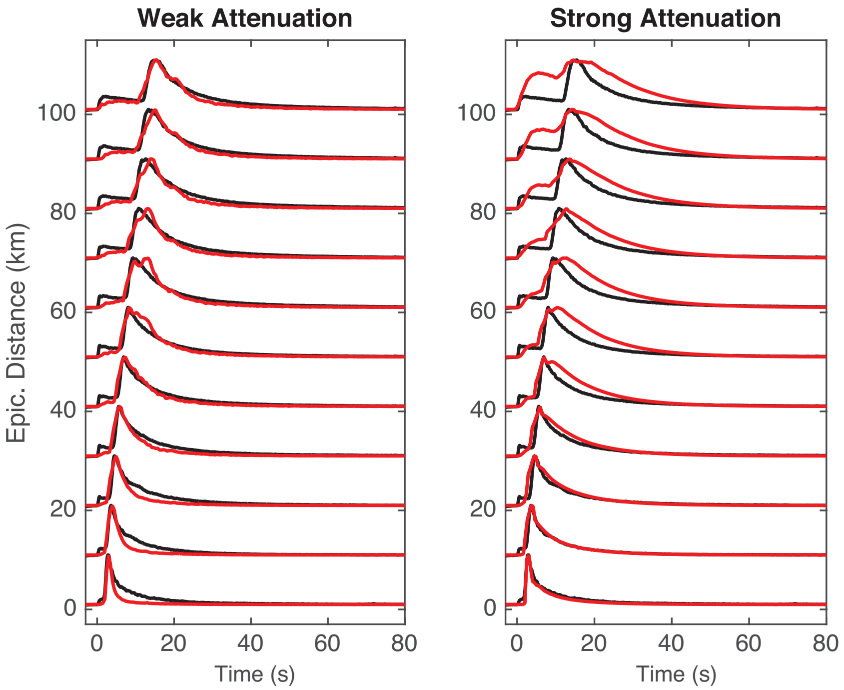

Figure 4.3: Examples of uniform half-space intrinsic and scattering attenuation models that can fit the data stacks at long ranges (left) or at short ranges (right). The black lines show the data stacks and the red lines show synthetics computed using the Monte Carlo method. The left model has relatively weak scattering and attenuation, which is required to fit the data at 50 to 100 km range, but underpredicts the coda amplitudes at close ranges. The right model has relatively strong scattering and attenuation, which is required to fit the data at 0 to 30 km range, but overpredicts the coda amplitudes at long ranges.

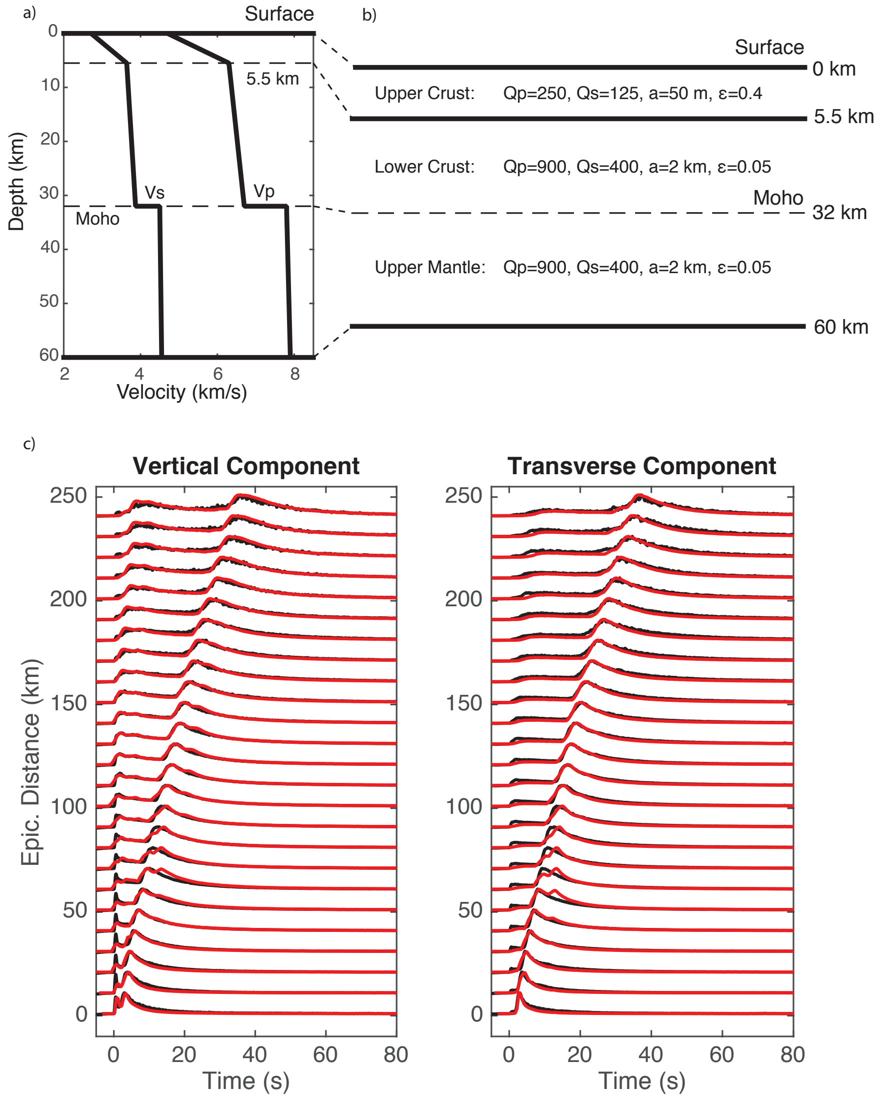

Figure 4.4: Our preferred model for the Monte Carlo simulation and the synthetic results compared to the data stacks. (a) the 1D intrinsic and scattering attenuation model. (b) and (c) synthetic results compared with real data for the vertical components, respectively. The red lines are the synthetic predictions; black lines are the data stacks.

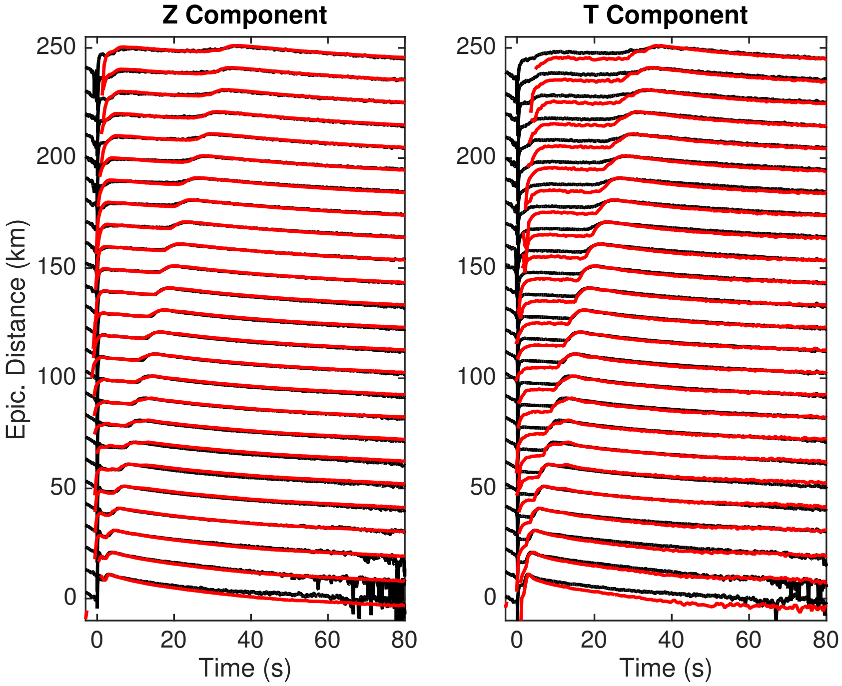

Figure 4.5: Similar to Fig 4c, but plotted using a logarithmic amplitude scale. The red lines are the synthetic predictions; black lines are the data stacks. The decaying amplitude before the P-wave arrival is an edge effect from our band-pass filter.

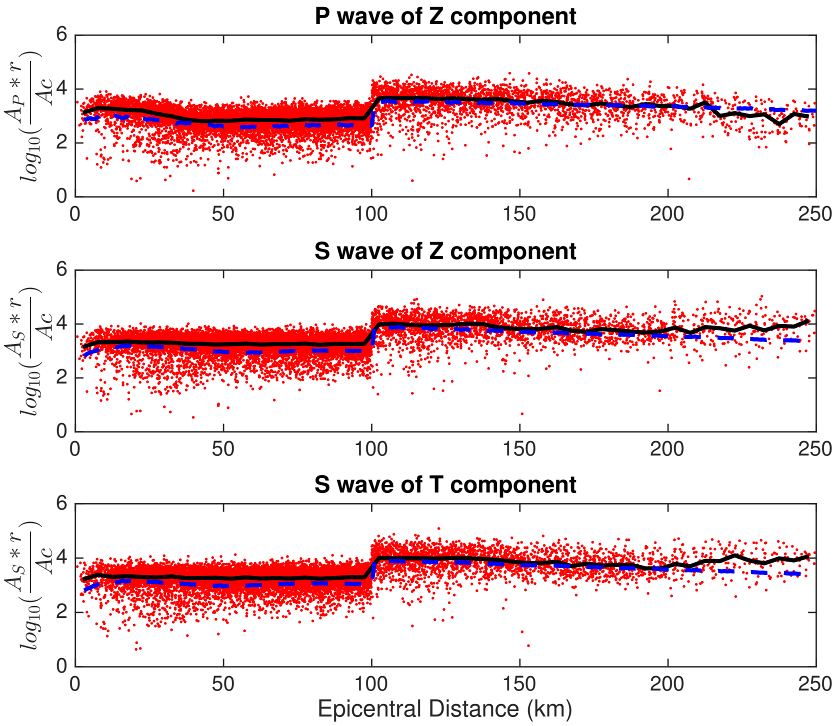

Figure 4.6: A comparison of peak P- and S-wave amplitude versus hypocentral distance based on the coda normalization method. Red dots show the data and the blue dashed line shows predictions of the Monte Carlo method applied to a layered scattering model. The shift at 100 km occurs because of a change at that distance in the lapse time used for the normalization (see text). The black lines show the median values of the data binned every 5 km. (a) P-wave peak amplitude of the vertical components. (b) S-wave peak amplitude of the vertical components. (c) S-wave peak amplitude of the transverse components.

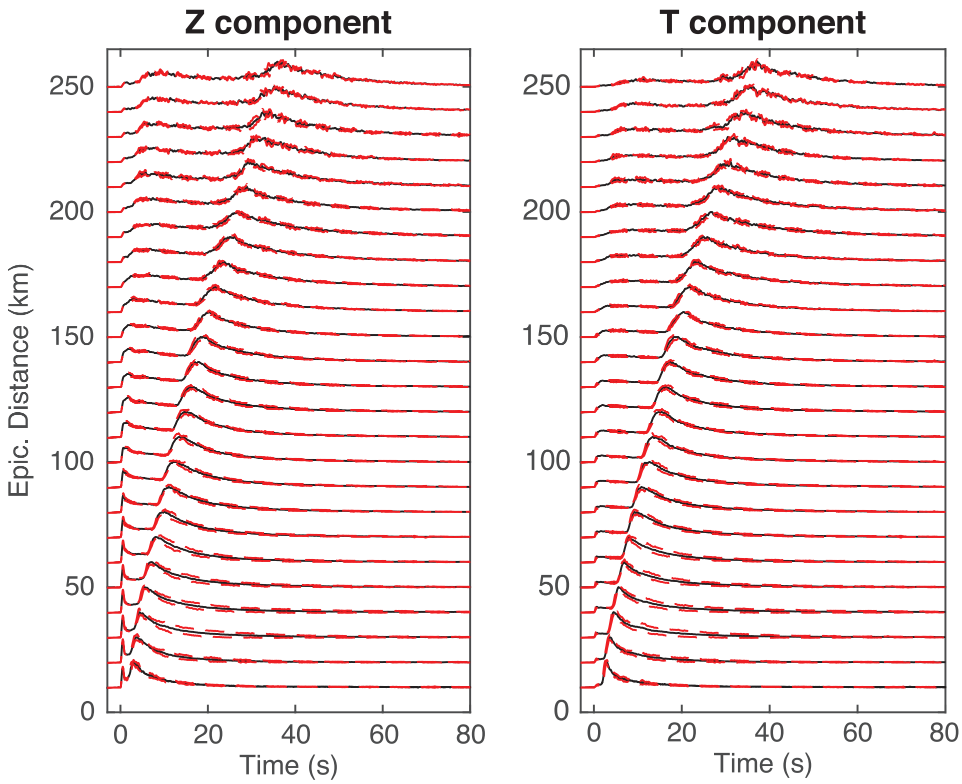

Figure 4.7: Estimated 1-σ errors of the data stack from bootstrap analysis are shown as red dashed lines, while the black lines show the data stacks.

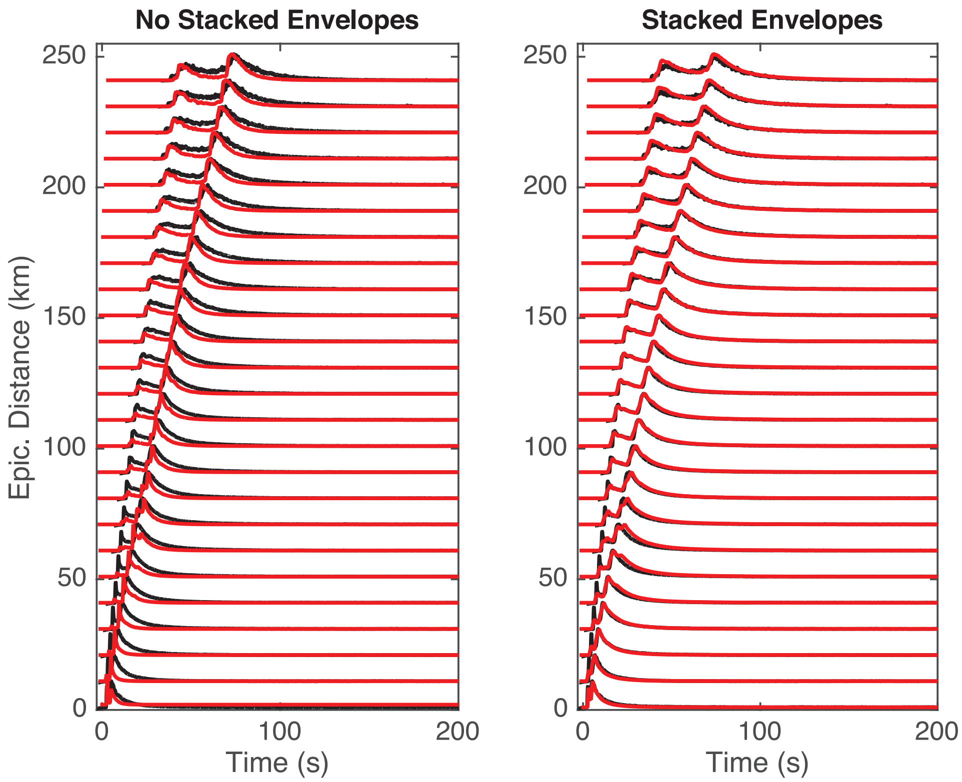

Figure 4.8: Comparison of stacked (left) and non-stacked (right) synthetic envelope functions. The red lines in each figure show the synthetic results and black lines show real data.

Table 4.1: Model parameters, including layer thickness (Δz km), correlation length (a m), rms perturbation (ε), intrinsic Q (${}^{\alpha}Q_I$ and ${}^{\beta}Q_I$), scattering Q (${}^{\alpha}Q_{Sc}$ and ${}^{\beta}Q_{Sc}$), the new scattering Q^* (${}^{\alpha}Q^*_{Sc}$ and ${}^{\beta}Q^*_{Sc}$), and total Q (${}^{\alpha}Q_T$ and ${}^{\beta}Q_T$).

Layer	Δz	a	ε	${}^{\alpha}Q_{Sc}$	${}^{\alpha}Q^*_{Sc}$	${}^{\alpha}Q_I$	${}^{\alpha}Q_T$	${}^{\beta}Q_{Sc}$	${}^{\beta}Q^*_{Sc}$	${}^{\beta}Q_I$	${}^{\beta}Q_T$
upper crust	5.5	50	0.4	192	161	250	108	133	108	125	64
ower crust	26.5	2000	0.05	59	569	900	349	36	931	400	280

Table 4.2: Misfit error table with correlation length (a) and rms perturbation (ε) of the upper crust.

ε a	0.3	0.35	0.4	0.45	0.5
40	27.30	24.94	23.45	22.35	21.99
45	25.02	23.31	22.17	21.58	22.34
50	23.44	22.07	21.76	22.56	24.21
55	22.53	21.77	22.54	24.04	26.25
60	22.30	22.43	24.13	26.60	29.15

Table 4.3: Misfit error table with correlation length (a) and rms perturbation (ε) of the lower crust and upper mantle.

ε a	0.04	0.045	0.05	0.055	0.06
1.6	26.67	25.78	26.38	27.15	27.36
1.8	24.40	23.72	23.91	24.16	23.69
2.0	23.40	23.14	21.76	23.22	23.44
2.2	23.24	22.94	24.16	24.28	23.54
2.5	24.61	24.77	25.44	25.79	25.86

Chapter 5

An Improved Method to Determine Coda-Q, Earthquake Magnitude and Site Amplification: Theory and Application to Southern California

Seismic coda waves can be used to constrain attenuation, estimate earthquake magnitudes, and determine site amplification factors. We have developed a new multi-station and multi-event method to determine these three important seismic parameters simultaneously. We analyze 642 representative local ($\leq$ 100 km) and shallow ($\leq$ 20 km) earthquakes with catalog magnitudes between 1.8 to 5.4 in southern California at multiple frequency bands centered at 1.5, 3, 6, and 12 Hz. We find that the length of the moving-average time window can affect the measurement of coda attenuation Q_C, but our tests indicate that the optimal window length is about 15 times the dominant data period. We use linear regression to fit each coda section and use only those portions that agree with the model decay rate with a correlation coefficient larger than 0.9. For a frequency-dependent coda-Q_C model ($Q_C = Q_0 f^n$) at 1 Hz reference frequency, our results yield estimates for Q_0 and n of 107–288 and 0.42–1.14, respectively. Our coda magnitude estimates are linearly correlated with catalog magnitudes, and our observed lateral variations in coda-Q_C and our site amplification factors are in general agreement with previous results, although there are notable differences at some locations. This approach provides a unified, accurate and stable method to measure coda-Q_C, earthquake magnitude, and site amplification using coda waves of locally recorded earthquakes.

5.1 Introduction

Since Aki (1969) and Aki and Chouet (1975) first interpreted coda waves using a single-scattering model, many methods have been developed to relate seismic attenuation to coda wave properties. Attenuation is characterized by the quality factor Q, whose reciprocal is the fractional energy loss per cycle of the passing wave. The coda energy decay can be expressed as

$$E(f,t) = S(f)R(f)t^{-\alpha}e^{-2\pi ft/Q_C(f)} \tag{5.1}$$

where E is the power spectrum, S is a frequency-dependent source amplitude term, R is a frequency-dependent station amplitude term, t is the lapse time, f is the frequency, α is a positive constant that is related to geometrical spreading and wave type (Aki and Chouet, 1975), and Q_C is the coda quality factor. Some studies indicate the value of coda attenuation, Q_C^{-1}, correlates with tectonics. High Q_C^{-1} values are observed in active regions and low values in stable regions (e.g. Singh and Herrmann, 1983; Hoshiba, 1993; Mitchell et al., 1997; Hiramatsu et al., 2000; Jin and Aki, 2005; Sato et al., 2012).

The properties of Q_C are of great interest. Rautian and Khalturin (1978) first observed that the measured Q_C depends on the lapse time, and ensuing studies reported an increase of Q_C with lapse time all around the world (e.g. Phillips and Aki, 1986; Ibanez et al., 1990; Hiramatsu et al., 2000; Carcolé and Sato, 2010; Calvet and Margerin, 2013). Another research question is whether there are temporal changes in Q_C associated with seismicity. Some studies found evidence that coda attenuation Q_C may change prior to earthquakes (Jin and Aki, 1988; Su and Aki, 1990, e.g.), and others observed a change of Q_C just before or after the earthquakes (e.g. Peng et al., 1987; Tsukuda, 1988; Wang et al., 1989; Huang and Kisslinger, 1992). However, other studies, including several that used similar earthquake pairs, have not obtained clear temporal changes in coda Q_C (e.g. Huang and Wyss, 1988; Woodgold, 1994; Beroza et al., 1995; Hellweg et al., 1995; Aster et al., 1996; Tselentis, 1997; Sumiejski and Shearer, 2012).

The physical meaning of coda-Q has also been widely discussed. Several studies have shown that coda waves are predominantly composed of scattered S waves (Aki and Chouet, 1975; Tsujiura, 1978; Kato et al., 1995). Coda attenuation contains contributions from both scattering attenuation and intrinsic attenuation and separating these two factors is a long-standing problem in seismology. There are two end-member models used to interpret coda attenuation, the single scattering model and the diffusion model. The single scattering model predicts that coda attenuation is a combination of scattering and intrinsic attenuation, $Q_C^{-1} = Q_{Sc}^{-1} + Q_I^{-1}$, while the diffusion model shows that Q_C asymptotically approaches the intrinsic attenuation Q_I at increasing times in the coda wavetrain in a simple uniform half-space (Shapiro et al., 2000). Another studies (Yomogida et al., 1997; Margerin et al., 1998, 1999; Wegler, 2004) use more complex but more realistic layer model to study the Q_C and indicate the relation between Q_C and intrinsic and scattering attenuation structure is complicated. Margerin et al. (1998) first points out the 'leakage effect', which significant affects Q_C in the layered models in the low-frequency range.

Determining the sensitivity of coda-Q to both scattering and intrinsic attenuation is an area of active research (Wennerberg, 1993; Margerin et al., 1998, 1999), in which advanced simulation methods such as radiative transfer are applied to more realistic depth-dependent models than the simple models that motivated early coda research (Wang and Shearer, 2017). We do not address these issues here, as we adopt an empirical approach to examine the origin of coda-Q variations in southern California, without attempting to resolve specific physical models that can explain coda-Q and its variations. We hope, however, that improved observational constraints on coda-Q will inform future modeling by identifying interesting signals to be explained, in particular the scale length of coda-Q variations and whether they are more coherent when mapped to station or source locations.

Earthquake magnitude is an important parameter for a variety of investigations. Current methods to determine magnitude depend on the amplitude of body waves, or on coda duration and/or amplitude (Lee et al., 1972; Herrmann, 1975; Archuleta et al., 1982; Bakun, 1984; Eaton, 1992; Mayeda et al., 2003; Sens-Schönfelder and Wegler, 2006; Denieul et al., 2015; Hawthorne et al., 2017). However, estimated magnitudes from body-wave amplitudes can be biased by the source radiation pattern and raypath focusing and defocusing anomalies (Mayeda et al., 2003). Since coda-wave magnitudes were first implemented by Johnson (1979) and Suteau and Whitcomb (1979), coda-wave magnitudes have proven to be more stable compared to other methods (Mayeda and Walter, 1996; Mayeda et al., 2003), as scattering tends to average out much of the spatial variability seen in direct-wave amplitudes.

Understanding and measuring site amplification is a fundamental problem for seismologists and earthquake engineers and helps to improve strong ground motion estimates. Since the late coda is dominately shear waves, the site amplification of coda waves closely approximates that of direct shear waves (Tsujiura, 1978; Phillips and Aki, 1986; Kato et al., 1995). By comparing results from direct shear waves and coda waves, Tsujiura (1978) and Tucker et al. (1984) argued that coda waves provide a more stable estimate of site effects, because the coda waves are composed of scattered seismic waves from different directions and average the heterogeneities around the source and receiver.

Based on a variety of research goals, previous studies have developed different methods to measure coda Q, source amplitude terms (e.g., magnitude), and site terms (e.g. Boatwright et al., 1991; Mayeda and Walter, 1996; Prieto et al., 2004; Shearer et al., 2006; Eulenfeld and Wegler, 2016). Starting with equation (5.1), most studies have attempted to separate the three terms, eliminate two of them and solve for the remaining term of interest (i.e., most coda-Q studies remove the source and station terms and then use linear regression to fit the coda energy decay). Dewberry and Crosson (1995) focus on the earthquake source by first fitting for coda-Q from individual records and then using least-squares inversion to solve for the best-fitting source and station amplitude terms, assuming the single scattering model. Mayeda and Walter (1996) used an empirical raypath correction based on 2-D multiple scattering to estimate the coda magnitude and spectra. Later, Eulenfeld and Wegler (2016) developed an improved method to fit the envelopes of direct S wave and S coda to resolve source amplitude terms and site terms, together with attenuation terms (intrinsic and scattering attenuation), and applied this method to data from USarray (Eulenfeld and Wegler, 2017). They used an analytic approximate solution of 3-D isotropic radiative transfer theory (Paasschens, 1997) to model the scattering effect to separate intrinsic and scattering attenuation.

Southern California is one of the most well-studied seismically active regions in the world and has seen a variety of studies on seismic attenuation structure (Frankel et al., 1990; Mayeda et al., 1991; Aki, 1996; Raoof et al., 1999; Hauksson and Shearer, 2006; Wang and Shearer, 2017; Lin and Jordan, 2018) and source properties and site effects (Boatwright et al., 1991; Kato et al., 1995; Su and Aki, 1995; Ben-Zion and Zhu, 2002; Prieto et al., 2004; Shearer et al., 2006; Trugman and Shearer, 2017). Here, based on equation (5.1), we invert the data to resolve simultaneously the coda attenuation Q_C, the source amplitude terms, and the station amplitude terms, assuming the multiple scattering model from late S coda ($>$ 2 times S travel time). To reduce the size of the inverse problem, we show how to set up a simplified problem with many fewer time points than the original data, but which produces the same L2-norm solution. To consider lateral variations in the attenuation structure in southern California, we introduce a source-side attenuation term together with the conventional station attenuation term to describe the coda energy decay. We show how our source amplitude term estimates can be related to coda magnitude and compare our coda attenuation and site amplification terms to those obtained in previous studies.

5.2 Data Selection and Proceeding

5.2.1 Data Selection

We select local events from a relocated catalog (Yang et al., 2012) from 2000 to 2013 and download waveform data using the Seismogram Transfer Program (STP) available from the Southern California Earthquake Center (SCEC). We use only events shallower than 20 km and stations at less than 100 km epicentral distance (to focus on body waves). We require three-components (either short-period (EH) or broadband (HH, BH) seismometers), since we compute the smoothed energy densities based on vector summation of the three components. The seismograms are generally sampled at 100 Hz.

Most coda-Q studies have examined station-averaged coda-Q, requiring a minimum number of recorded events at each station to obtain stable estimates. For our multi-station and multi-event method (MSMEM), we also require both a minimum number of stations recording each event and events recorded by each station, and have found that a threshold of 10 events per station and 10 stations per event is enough to yield stable results. We filter the seismograms with a 4th-order zero-phase Butterworth filter at the following octave frequency bands: 1–2, 2–4, 4–8 and 8–16 Hz. For each trace, we estimate the noise level by using the energy densities in a 3-s time window before the P-wave arrival and the coda level from a 40-s window starting at the 50-s lapse time used to measure the coda attenuation at each frequency band. We require that the coda level be at least five times larger than the pre-event noise level.

5.3 Methodology: Multiple Station and Multiple Event Method

5.3.1 Single Station and Multiple Event Method

Even if the dependence of measured coda attenuation Q_C on the components is weak, the site amplifications between vertical and horizontal components may be different (Kato et al., 1995). We directly measure coda attenuation Q_C from the energy densities. We rewrite equation (5.1) as

$$E_{ij}(f,t_k) = S_i(f)R_j(f)t_k^{-\alpha}e^{-2\pi f t_k/Q_{Cij}}, \tag{5.2}$$

where E_{ij} indicates the energy density of the coda wave, S_i indicates the i-th source amplitude term, R_j indicates the j-th station amplitude term, and Q_{Cij} is the quality factor of the coda wave for the raypath between the i-th source and j-th station. To implement linear inversion, we take the natural logarithm and obtain

$$e_{ij}(f,t_k) = s_i(f) + r_j(f) + (-\alpha)\log(t_k) + \frac{-2\pi f}{Q_{Cij}(f)}t_k \tag{5.3}$$

where e_{ij}, s_i and r_j denote $\log E_{ij}$, $\log S_i$ and $\log R_j$, respectively.

Conventional methods measure the coda attenuation Q_C from the waveforms by only considering the time-dependent terms in equation (5.3). Assuming the geometrical spreading term α is a constant, e.g., α is set to 2 for body-wave coda studies, assuming the single scattering model (Aki and Chouet, 1975; Dewberry and Crosson, 1995; Carcolé and Sato, 2010). In this study, we use $\alpha = 1.5$ estimated from 3D diffusion theory in a whole space (Paasschens, 1997; Margerin et al., 1998). We find that the choice of α does not effect the results significantly (see discussion). We can express (3) as

$$b_{ij}(f,t_k) = e_{ij}(f,t_k) + \alpha \log(t_k) = C_{ij} + \frac{-2\pi f}{Q_{Cij}(f)} t_k \tag{5.4}$$

in which we subtract $-\alpha \log(t_k)$ from our original coda power time series, $a(t)$, to create a new time series, $b(t)$ which has been corrected for geometrical spreading. For each $b(t)$, we can apply simple linear regression to solve for the best-fitting amplitude factor C and slope parameter $-2\pi f/Q_C$. This provides a separate coda attenuation estimate Q_C^{-1} for each seismogram. Assuming that much of the variation Q_C^{-1} is caused by near-station differences, the values Q_C^{-1} obtained at each station can be averaged to obtain a measure of the average attenuation properties around the station (Jin and Aki, 1988; Aki, 1996; Carcolé and Sato, 2010). We term this commonly-applied approach the Single Station and Multiple Event Method (SSMEM). Notice that by replacing the separate event and station amplitude factors s_i and r_j in equation (5.3) with a seismogram-specific scaling factor, C_{ij}, the model now has many more free parameters.

Previous studies have shown that the coda attenuation Q_C increases with lapse time but eventually settles at a stable value (Rautian and Khalturin, 1978; Phillips and Aki, 1986; Yoshimoto and Jin, 2008; Carcolé and Sato, 2010; Calvet and Margerin, 2013). However, the required lapse time for convergence is hard to determine precisely. It depends on a variety of factors, such as the frequency band and source location. There are two main approaches to setting the minimum lapse time for data analysis. One is to use the lapse time $\alpha r/v$, where α is a time-lapse coefficient, always set to 2 (Hiramatsu et al., 2000; Carcolé and Sato, 2010; Calvet and Margerin, 2013), r is the epicentral distance, and v is the average crustal shear-wave velocity. The coda waves after twice the shear-wave travel time are considered independent of the source mechanisms and affected only by the multiple scattering behavior. Another strategy is to use a constant lapse time, but long enough to ensure that the coda waves suffer enough scattering during the propagation (Kato et al., 1995; Calvet and Margerin, 2013). A further complication is that the coda attenuation measurement also depends on the length of the time window. Given the scatter in real data, a too-short window cannot reliably determine the coda-decay rate, but a too-long window may extend into the low signal-to-noise regime where the coda begins to merge back into the background noise. Here, we use a 40-s-long time window starting at a lapse time of 50 s. Note that 50 s is slightly more than twice the S-wave travel time at the maximum epicentral distance of 100 km and that our signal-to-noise selection criteria should ensure that we are still resolving coda power at 90 s.

The squared seismograms are smoothed with a moving-average window. The length of the appropriate moving window depends on the frequency band (Phillips and Aki, 1986; Carcolé and Sato, 2010; Calvet and Margerin, 2013). The choice of averaging length can affect the measurement of coda attenuation Q_C. Most previous studies define the length as a function of the central frequency of the frequency band, $T_W = a/f$, where f is the central frequency and a is an adjustable parameter. If a is too large, the coda decay rate will change because of over-smoothing; on the other hand, if a is too small, near-zero values may persist in the coda window, which will bias the fits in the log domain. In this study, a is assigned 15, comparable to Phillips and Aki (1986) and Calvet and Margerin (2013). We use linear regression to fit each smoothed coda wave and only those portions that agree with the model decay rate with a correlation coefficient larger than 0.9 are used for later analyses. The coda waves with positive coefficients (i.e., their amplitudes grow with time and $Q_{Cij} < 0$) are discarded. This procedure serves to remove observations contaminated by aftershocks, noise spikes, or other effects.

5.3.2 Multiple Station and Multiple Event Method

Because our goal is to solve for both source amplitude terms and station amplitude terms together with coda attenuation, we model C_{ij} in equation (5.4) as a sum of a source amplitude term s_i and station amplitude term r_j. For one coda record at frequency f we have

$$\begin{bmatrix} b_{ij}(t_1) \\ b_{ij}(t_2) \\ \vdots \\ b_{ij}(t_k) \end{bmatrix} = \begin{bmatrix} e_{ij}(t_1) \\ e_{ij}(t_2) \\ \vdots \\ e_{ij}(t_k) \end{bmatrix} + \begin{bmatrix} \log(t_1) \\ \log(t_2) \\ \vdots \\ \log(t_k) \end{bmatrix} \alpha = \begin{bmatrix} 1 \\ 1 \\ \vdots \\ 1 \end{bmatrix} s_i + \begin{bmatrix} 1 \\ 1 \\ \vdots \\ 1 \end{bmatrix} r_j + \begin{bmatrix} t_1 \\ t_2 \\ \vdots \\ t_k \end{bmatrix} \frac{-2\pi f}{Q_{Cij}} \tag{5.5}$$

The decay rate depends only on the average medium properties of the crust sampled by the coda waves. These properties of coda waves offer an alternative approach for studying the source and site effects on high-frequency seismic waves. Local coda waves are likely backscattered S waves from heterogeneities distributed in a volume surrounding the source and receiver (Tsujiura, 1978; Aki, 1980; Mayeda et al., 1991; Koyanagi et al., 1992). This explains why local S-wave coda records decay at a similar rate for all source-station pairs within a localized region. However, our study region in southern California is large enough that lateral variations in attenuation structure are apparent, so modeling coda decay variations only as a function of the station location, as in the SSMEM method, may be insufficient. Because the coda decay rates at a single station can vary (see Figure 5.2) at all frequency ranges, we introduce another attenuation term, the source-side attenuation term. Equation (5.5) is rewritten as

$$\begin{bmatrix} b_{ij}(t_1) \\ b_{ij}(t_2) \\ \vdots \\ b_{ij}(t_k) \end{bmatrix} = \begin{bmatrix} 1 \\ 1 \\ \vdots \\ 1 \end{bmatrix} s_i + \begin{bmatrix} 1 \\ 1 \\ \vdots \\ 1 \end{bmatrix} r_j + \begin{bmatrix} t_1 \\ t_2 \\ \vdots \\ t_k \end{bmatrix} \frac{-2\pi f}{Q^S_{Ci}} + \begin{bmatrix} t_1 \\ t_2 \\ \vdots \\ t_k \end{bmatrix} \frac{-2\pi f}{Q^R_{Cj}}, \tag{5.6}$$

where Q^S_{Ci} is the i-th source-side coda attenuation and Q^R_{Cj} is j-th station-side coda attenuation. We combine the records from different stations and different events and rearrange equation (5.6) as **d=Gm**. The **G** matrix is large and sparse, but in principle solvable using sparse-matrix least-square methods. However, each data vector $b_{ij}(t_k)$ contains a 40-s waveform (i.e., 4000 discrete time points), which when combined with many different events and stations, results in a very large inverse problem. To reduce the size of the problem, we define a corrected data vector $\hat{b}_{ij}(t_k) = \hat{e}_{ij}(t_k) + \alpha \log(t_k)$, where $\hat{e}_{ij}(t_k)$ is the best fitting $e_{ij}(t_k)$ by using equation (5.4). In the appendix, we prove that the new inverse problem has the same L2-norm solution as equation (5.6). Since the fit to the data vector is controlled by only two parameters, we can greatly reduce the size of the corrected data vector. In this study, we use just 2 points to represent each waveform instead of 4000 points.

5.3.3 Error Estimation

Based on the least-squares solution, the misfit function is defined as,

$$err = \frac{\sqrt{\sum_{i,j,k}(\hat{b}_{ij}(t_k) - s_i - r_j + 2\pi f t_k / Q^S_{Ci} + 2\pi f t_k / Q^R_{Cj})^2}}{\sqrt{\sum_{i,j,k} \hat{b}^2_{ij}(t_k)}}. \tag{5.7}$$

where i is the index for the source, j for the station and k for the time series. The least-squares method finds the parameters that minimize err. However, to avoid biasing the solution with anomalous data (outliers) we exclude some of the data as follows. We define a reference misfit based on equation (5.4) as

$$err_1^{ij} = \sqrt{\sum_{k=1}^{n} (\hat{b}_{ij}(t_k) - C_{ij} - \frac{-2\pi f}{Q_{Cij}(f)} t_k})^2. \tag{5.8}$$

err_1 describes the misfit between a single coda waveform and its best fitting curve from a model that includes a custom amplitude scaling term, C_{ij}. After solving the inverse problem of equation (5.6), we define the new misfit for each trace as

$$err_2^{ij} = \sqrt{\sum_{k=1}^{n} (\hat{b}_{ij}(t_k) - s_i - r_j + \frac{2\pi f}{Q_{Cij}(f)} t_k})^2. \tag{5.9}$$

err_2 describes the misfit between a single coda waveform and its best fitting curve from a model in which the amplitude scaling is given by the sum of a source term, s_i, and a receiver term, r_j. For some waveforms, the coda amplitude is poorly approximated by this sum and the misfit will be correspondingly larger. If $err_2 > 5 \times err_1$, we flag this trace as an outlier and remove it from the dataset. After removing all the outliers, we repeat solving the inverse problem and continue removing outliers until there are no more outliers found. In this study, this process converges after 4–6 iterations and removes about 20% of the original data. This fraction exceeds the percentage of individual seismograms that fail the misfit test because removal of traces will sometimes cause entire events or stations to be removed from the dataset if they no longer meet the 10 stations per event and 10 events per station criteria.

The model uncertainty of the least-squares inverse problem can be estimated by using the method in Menke (2012). If we assume the data are uncorrelated and the variance of the observed data is σ_d, the covariance matrix of the least squares solution m can be estimated from

$$\mathrm{cov}[\mathbf{m}] = \left[[\mathbf{G}^T\mathbf{G}]^{-1}\mathbf{G}^T\right]\sigma_d^2\left[[\mathbf{G}^T\mathbf{G}]^{-1}\mathbf{G}^T\right]^T = \sigma_d^2(\mathbf{G}^T\mathbf{G})^{-1}. \tag{5.10}$$

where $\mathbf{G}^T\mathbf{G}$ is invertible in this overdetermined inverse problem. The data resolution matrix for the overdetermined inverse problem $\mathbf{N} = \mathbf{G}[\mathbf{G}^T\mathbf{G}]^{-1}\mathbf{G}^T = \mathbf{I}$ indicates the prediction error can be ignored in the inversion (Menke, 2012, p. 70). The single coda waveform can be described by equation (5.5). Since we use the corrected coda waveforms in the inversion and do not know the measurement error, the variance estimated from the difference between the coda waveform and the best fitting curve by equation (5.5) is used as the data variance,

$$\sigma_d^2 = \sum_{k,i,j}(\hat{b}_{ij}(t_k) - C_{ij} - \frac{-2\pi f}{Q_{Cij}(f)}t_k)^2/(N-1), \tag{5.11}$$

where N is the product of the number of points in each discrete time series and the number of coda waveforms. In each frequency range, the estimated source and station amplitude term errors are of order 10^{-2} and the source- and station-side attenuation terms are of order 10^{-4}. The formal relative errors are thus about 1% of the best-fitting attenuation terms, although this should be considered a lower error bound because it does not take into account the possibility of systematic (correlated) errors in the data, such as might be generated by 3D attenuation structure not fully modeled by source and station amplitude terms alone.

5.4 Results

In total we obtained 16,318 measurements from 642 events with catalog magnitudes between 1.8 and 5.4 at 105 stations. The numbers of seismograms are 14,781, 14,781, 14,909 and 8244 for the frequency bands centered at 1.5, 3, 6 and 12 Hz, respectively.

5.4.1 Coda Magnitude and Coda Spectra

Coda waves are less affected by the source radiation pattern and directivity than direct waves and thus coda-derived magnitudes are potentially more reliable and stable than those computed using other methods. At long lapse times, coda waves sample and average a large volume surrounding the source and receiver region. In equation (5.7), the source amplitude term is a measure of the source radiated energy at a particular frequency (Aki, 1969; Mayeda and Walter, 1996; Mayeda et al., 2003; Sens-Schönfelder and Wegler, 2006; Baltay et al., 2010), which can be used to compute the source magnitude or source spectra.

In the inversion, there is a trade-off between the source and station amplitude terms and the source-side attenuation and the station-side attenuation terms (i.e., if we remove a constant from the source amplitude terms and add it to the station amplitude terms, the misfit shown in equation (5.8) for the inverse problem remains the same). However, the relative differences in the terms among each set are resolved, even if their mean values are uncertain because of the source vs. station trade-off. We can resolve the trade-off by setting the mean of one set of terms to zero, which will maximize the signal in the other set of terms. For example, we can remove the mean of the source-side attenuation terms and add it to the station-side attenuation terms and then compute station specific coda-Q, which can be compared with the conventional SSMEM method. Sens-Schönfelder and Wegler (2006) use a similar method to solve for coda magnitude assuming the logarithmic average of the station terms is zero at all frequency ranges and then fit the source spectra by applying the omega-squared model. Here, we also remove the absolute amplitudes from the source terms and Figure 5.3 shows the source amplitude terms at different frequency bands. At the low-frequency bandpasses (1–2 and 2–4 Hz), the source amplitude terms scale linearly with catalog magnitude (i.e., larger source amplitude terms for larger earthquakes), as expected given that these two frequency ranges are well below the corner frequencies of most earthquakes in our dataset. At frequencies above 4 Hz, the source amplitude terms no longer scale linearly because the effect of earthquake corner frequency can no longer be ignored.

For small earthquakes ($M_L \leq 3.5$), the magnitudes listed in the catalog are the local magnitudes (M_L) rather the moment magnitudes (M_W). Previous studies have indicated that $M_W \neq M_L$ (Shearer et al., 2006; Hutton et al., 2010; Ross et al., 2016; Trugman and Shearer, 2017). Before calibrating the source amplitude term to coda spectra, we need to compute the moment (M_0) for each event as our first step. Here, we follow the method in Shearer et al. (2006). At low frequency (1–2 Hz), we first perform a linear regression between catalog magnitude M_L and source amplitude terms s: $M_L = as + b$. Since we use the energy densities of the seismograms and the moment is proportional to the low frequency amplitude, the source amplitude terms scale linearly with log moment as $\log_{10}(M_0) = s/2 + C$ with scaling factor 0.5. The moment magnitude M_W (Kanamori, 1977) may be expressed as

$$M_W = \frac{2}{3}\log_{10} M_0 - 10.7 \tag{5.12}$$

where the moment M_0 is in N-m. Finally, the source amplitude term of each event is converted to moment by assuming that $M_L = M_W$ at $M_W = 3.5$, consistent with recent results of *Ross et al.* [2016]. We estimate the moment M_0 as a function of catalog moment M_L expressed as,

$$M_0 = 10^{1.26(M_L - 3.5)} 1.43 \times 10^{14}\ N \cdot m \tag{5.13}$$

Our observed scaling between M_L and $\log_{10}(M_0)$ is 1.26, which is within the range of 1.0 to 1.5 found in previous studies. Ben-Zion and Zhu (2002) obtained 1.0 for $M_L < 3$ events and 1.34 for $3.5 < M_L < 6.0$ in southern California and Bakun (1984) estimated 1.2 for $1.5 \leq M_L < 3.5$ events and 1.5 for $3.0 < M_L < 6.0$ events in central California. Scaling factors in other studies include 1.0 for $M_L < 3.7$ by Abercrombie (1996), 1.04 for $1.5 \leq M_L \leq 3.1$ by Shearer et al. (2006), 1.1 for $1.5 \leq M_L \leq 4$ by Hawthorne et al. (2017), 1.22 for $0 \leq M_L \leq 4$ by Ross et al. (2016), and 1.5 for $1.8 \leq M_L \leq 3.4$ by Prieto et al. (2004). In general, larger scaling factors are expected for larger earthquakes where M_L and M_W are in better agreement (see Figure 9.25 from Shearer, 2009), and this is seen in the observed factors of 1.39 for $3 \leq M_L \leq 7$ events by citetarchuleta1982source and 1.5 for $3 \leq M_L \leq 7$ by Thatcher and Hanks (1973). Note that our coda study includes larger earthquakes (112 $M_L \geq 3.5$ events and 69 $M_L \geq 4.0$ events than the $1.5 \leq M_L \leq 3.1$ range in the P-wave spectral study of Shearer et al., 2006).

Differences in the source amplitude terms as a function of frequency contain information about the source spectra. However, because of the tradeoff between the average source and station amplitude terms, the source amplitude terms at a given frequency only resolve the relative differences among the events and cannot be used directly to estimate the source spectrum of individual events by comparing the terms at different frequencies. To resolve this ambiguity, we apply the multiple-event empirical Green's function (EGF) approach used in spectral analysis of direct phases (e.g. Shearer et al., 2006; Oth et al., 2011). We stack the source amplitude terms at 0.2 increments in calibrated moment magnitude bins from $M_W = 2.3$ to 3.9 for the frequency bands centered at 1.5, 3, 6 and 12 Hz, respectively. Following Shearer et al. (2006), we estimate an EGF spectrum that will bring the stacked source amplitude terms into agreement with a theoretical model of the source spectra. Specifically we minimize the L2-norm residual between the EGF-corrected stacked spectra and a self-similar Brune-type circular crack model (Brune, 1970; Madariaga, 2007). The amplitude of source spectra model is expressed as

$$S(f) = \frac{2\Omega_0}{1+(f/f_c)^\eta}, \tag{5.14}$$

where Ω_0 is the long-period displacement amplitude, f is the frequency, f_c is the corner frequency and 2 is the scaling factor from displacement to the energy densities. The corner frequency in the source model related to the moment and the stress drop is expressed as (Madariaga, 1976; Abercrombie, 1995; Shearer et al., 2006),

$$f_c = \frac{0.42\beta}{(M_0/\Delta\sigma)^{1/3}} \tag{5.15}$$

where β is the S-wave velocity, M_0 is the moment, and $\Delta\sigma$ is the stress drop, and β is shear-wave velocity, assumed here a constant 3.5 km/s.

Assuming a self-similar constant stress drop model, we perform a grid search over stress drop to determine the EGF that minimizes the difference between the EGF-corrected stacked spectra and the synthetic spectra of the Brune-type source model. Following Trugman and Shearer (2017), we also experiment with models in which stress drop varies as a function of moment, specifically as

$$\log_{10}\Delta\sigma = \varepsilon_0 + \varepsilon_1 S(0) \tag{5.16}$$

where $S(0)$ is the long-period displacement amplitude (proportional to moment), ε_0 and ε_1 are two model parameters to describe the scaling between moment and stress drop.

Figure 4 shows results for both the self-similar and non-self-similar scaling models.

Results for the 8–16 Hz frequency range are problematic (i.e., yield poor fits), most likely a result of the poorer signal-to-noise in this band and the fact that it is difficult to use a single center frequency for plotting purposes when many of the earthquake corner frequencies are in this range. Consequently, we only use the 1–2, 2–4 and 4–8 Hz bands to fit the source spectra. The best fitting ω^{-2} Brune-type stress drop for the self-similar model is 19 MPa, which is higher than the average stress drop seen in previous studies. However, the best fitting ω^{-2} Brune-type stress drop for the non-self-similar model ranges from 2.5 MPa to 13.7 MPa with scaling parameter $\varepsilon_1 = 0.31$, which roughly agrees with results for the San Jacinto region of southern California in Trugman and Shearer (2017). Compared to the self-similar source model ($err = 0.165$), the non-self-similar source model yields a better fit ($err = 0.121$) (see Figure 5.4 a & b). However, the model fits are far from exact, and there is a fundamental trade-off between the non-self-similar scaling parameter (ε_1) and the assumed high-frequency fall-off rate (η) (Trugman and Shearer, 2017). Thus, the source spectral results shown here should be considered tentative until a more complete analysis can be performed that considers all of the model uncertainties and parameter tradeoffs. However, uncertainties in the source spectral calibration do not affect the accuracy of the amplitude and coda decay terms that are the main focus of this paper. We plan further study of coda-based source spectral estimates and comparisons to direct phase spectral analyses in future work.

5.4.2 Site Amplification

As mentioned in the Coda Magnitude section, the mean value of the station amplitude terms is removed, which means the station amplitude terms are relative to the ‘average station’ (Phillips and Aki, 1986; Su et al., 1991, 1992; Su and Aki, 1995). Since the smoothed energy densities are used in this study, we apply a scaling factor of 0.5 to correct them to amplitude site amplification factors. Figure 5.5 a–d show the site amplification factors at different frequency bands. To validate the accuracy of our approach, we compare our results with another coda-based method to determine site amplification developed by Phillips and Aki (1986), which was used by later studies in southern California (i.e. Su et al., 1991, 1992; Su and Aki, 1995). Their method is also based on equation (5.3); given the frequency and lapse time, the logarithmic RMS coda energy can be written as

$$e_{ij}(t_k) = s_i + r_j + c_{ij}(t_k), \tag{5.17}$$

where $c_{ij}(t_k)$ is a constant among all the records given the lapse time t_k, which assumes a uniform spacial distribution of the coda attenuation Q_C. The uniform coda attenuation Q_C can explain most of the observations compared to the station and source side variant Q_C (see Table 1). This assumption differs from our MSMEM approach and may cause some differences in the results. We compute an average of e_{ij} over all the available stations for the i-th source and this average ($\bar{e}_{ij}^{jk}(t_k)$) is removed from the RMS energy e_{ij} with the fixed i-th source, that is

$$\frac{1}{2}\left[e_{ij}(t_k) - \bar{e}_{ij}^{jk}(t_k)\right] = r_j - \bar{r}, \tag{5.18}$$

where $\bar{r}$ is the average site amplification and the scaling factor $1/2$ is used to correct the results to amplitude site amplification. Equation (5.18) can be written in the form $\mathbf{d} = \mathbf{Gm}$. The $\mathbf{G}$ is a large, sparse matrix, so we apply the same least-squares method. The results at different frequency bands are shown in Figure 5.5 e–h. In general, the results from the two methods are quite similar, as shown in Figure 5.6. The ratio of differences between the methods are less than 0.3 in log-10 scale, scaling factor 2, 100%, 99%, 95% and 85% at 1–2, 2–4, 4–8, 8–16 Hz, respectively. These comparisons indicate our site amplification results are generally consistent with the method of Phillips and Aki (1986).

In Su et al. (1992); Su and Aki (1995), they pointed out the site amplification is related to the geology underlying the station. Our results are spatially consistent with their results. For instances, the stations on the Mesozoic granitic rocks or Pre-Cretaceous metamorphic rocks have low site amplification but gradually increase with frequency, which appears on the stations around the San Jacinto Fault Zone (-116.6°W, 33.5°N). At the centered frequency 1.5 Hz, the region around the northern end of the Chino Fault (-117.6°W, 34°N) and the southeastern region of the Salton Trough (-115.8– -115.2°W, 33°N), which consist mainly of Cenozoic sediments, show the highest amplification and gradually decrease with frequency. Also, along the San Andreas fault, the site amplifications do not show systematic changes, which was also pointed out by Su et al. (1992).

5.4.3 Coda Attenuation

Coda attenuation Q_C is another important parameter in our method. We separate coda attenuation into two parts, source-side attenuation (Q_C^S) and station-side attenuation (Q_C^R) (see equation (5.6)). Considering the trade-off between these two terms, to view the variation in source-side attenuation and station-side attenuation, we rewrite the attenuation terms in the new form,

$$Q^{S}_{Ci}{}^{-1} + Q^{R}_{Cj}{}^{-1} = \delta Q^{S}_{Ci}{}^{-1} + \delta Q^{R}_{Cj}{}^{-1} + \overline{Q_C^{-1}} \tag{5.19}$$

where $\bar{q}$ is the mean value of the total attenuation terms and δQ^{S-1}_{Ci} and δQ^{R-1}_{Cj} are perturbations to mean coda Q_C^{-1} on the source and station sides, respectively. The reciprocal of the summation of the station-side variation (δQ_C^{R-1}) and the mean value ($\overline{Q_C^{-1}}$), which is the station-side coda attenuation (Q_C^R) has the same physical and mathematical meaning as in the conventional method (SSMEM). Similarly, we can define a source-side attenuation term, Q_C^S, which is the reciprocal of the summation of the source-side variation (δQ_C^{S-1}) and the mean value ($\overline{Q_C^{-1}}$), likely describes differences in scattering from heterogeneity close to the source regions.

To validate our approach, we compare our results with those from SSMSM, which measures the attenuation at each station recording multiple events. The measured coda attenuations are averaged and plotted at each station. As shown in Figure 5.7, the spatial variations in Q_C are similar for the different methods. Previous studies (e.g. Aki, 1980; Jin and Aki, 2005; Carcolé and Sato, 2010) have indicated the coda attenuation follows a frequency-dependent power law, $Q(f) = Q_0 f^n$. The results from MSMEM indicate that Q_0 and n are within the ranges 107–288 and 0.42–1.14, respectively. The results from SSMEM are in reasonable agreement, with Q_0 and η within the range 111–264 and 0.45–0.99, respectively. The spatial variations of Q_0 and n are also correlated between the methods, as shown in Figure 5.8. Although there are some differences, overall the results from MSMEM are consistent with SSMEM. In general our values of Q_0 and n agree with previous studies, which indicate Q_0 is within 100–500 and n within 0.4–1.3 (e.g. Singh and Herrmann, 1983; Jin and Aki, 1988; Mayeda et al., 1991; Jin and Aki, 2005; Yun et al., 2007; Carcolé and Sato, 2010).

In Figure 5.9, we show the spatial distribution of the removed mean source-side attenuation terms $-2\pi f/Q_C^S$ at 1–2, 2–4, 4–8, 8–16 Hz, respectively. The spatial patterns between source-side attenuation and station-side attenuation at different frequency bands are similar but have some variation. As in the case of the site amplification results, the largest discrepancy appears for the frequency band 8–16 Hz, probably because of a low signal-to-noise ratio. On the other hand, the spatial variations of source-side attenuation are not exactly the same as the station-side variations, because the sources are located at different depths from 0–20 km. Figure 5.10 and Figure S5.1–S5.4 in the supporting information indicates that the source-side attenuation is not related to the source depth. However, the source-side attenuation shows positive correlation with the coda magnitudes (see Figure 5.11c). To examine this relationship, we compute the source-side attenuation using the coda wave in the first-half time window (i.e. 50–70 s) and the second-half time window (i.e. 70–90 s), compared to the results within the whole-time window 50–90 s. The comparison of the two half-time windows indicates that the positive correlation is an artifact from the low signal-to-noise ratio at longer times. This positive correlation is stronger in the second time window than in the first time window and this effect is stronger for small events than larger events. The strongest positive correlation appears in the second time window at the frequency range 8–16 Hz, together with the most scattered results. The misfit errors for the second half-time window are systematically larger than the misfit errors for the first half-time windows. Because of this time dependence, it is likely that signal-to-noise issues are causing the apparent positive relation between coda-Q and coda magnitude.

5.5 Discussion

Geometrical spreading of coda waves is accounted for by the α term. Here, we use $\alpha = 1.5$ for epicentral distances smaller than 100 km, assuming the 3D diffusion case in a whole space, as in previous studies (Margerin et al., 1998; Calvet and Margerin, 2013). If instead we use $\alpha = 2.0$, assuming the single scattering model, which is another widely applied value in coda attenuation studies (see Hiramatsu et al., 2000; Carcolé and Sato, 2010), there is little change in the relative values among the station, source, and attenuation terms, but there is a systematic shift in their absolute values. In this study, since we remove the mean value from the station amplitude terms and the source-side attenuation terms, the shift occurs in the other terms and is -0.699 for the source amplitude terms (s_i) and 7.27×10^{-3} for the station-side attenuation terms ($-2\pi f/Q_C^R$). It should be noted that we use a fixed time window to measure the coda waves. Calvet and Margerin (2013) found that Q_C estimated by using SSMEM and $\alpha = 2$ is typically about 10% higher than when using $\alpha = 1.5$. Considering they used a time window starting at twice the S travel time and a fixed lapse time, their results are consistent with ours. Overall, larger α values slightly increase the Q_C values, but since physically realistic α values are from 1–2, the variation of α does not affect the final results very much.

Previous studies (Calvet and Margerin, 2013) indicate that the choice of the time windows can affect the measurement of coda attenuation. To consider this issue, we test time windows of 30, 40 and 50 s. We find that compared to the 40s case, the relative differences are small, i.e., over 90% of the station and source amplitude terms have a difference smaller than 0.5 and source- and station-side Q_C^{-1} smaller than 0.001. This indicates that within the window length range of 30–50 s, the solutions are robust. Second, increasing the window length increases the measured Q_C, which was also reported by Calvet and Margerin (2013). To examine this effect, we keep the window length fixed at 40 s and change the starting lapse time to 60 and 70 s. We find the measured Q_C systematically increases with the starting lapse time, which was also reported by some other studies, (Rautian and Khalturin, 1978; Phillips and Aki, 1986; Hiramatsu et al., 2000; Yoshimoto and Jin, 2008; Carcolé and Sato, 2010).

The physical meaning of coda attenuation Q_C, including the relative importance of scattering versus intrinsic attenuation, has been debated for some time. In principle, contributions to the coda come from within an ellipsoidal-shaped volume defined by the source-to-scatterer-to-station travel time. Relating differences in observed coda Q_C to variations in properties within this volume is not straightforward, but some clues about the source of coda Q_C variations are provided by mapping them to the stations or the source-receiver midpoint (Roecker et al., 1982; Pulli, 1984; Steck et al., 1989; Aki, 1996). Here we examine coda Q_C variations across southern California, as assigned both to the stations (Fig. 5.7) and to the sources (Fig. 5.9). These maps exhibit spatial coherence, which provides some reassurance that the observed variations are not caused by purely random coda fluctuations, but they often exhibit changes over shorter length scales than the size of the scattering ellipsoid. This indicates that the entire scattering volume does not contribute equally to coda Q_C variations, that changes in properties in the shallow crust beneath the stations and within seismically active regions are particularly important. In general, both the source-side and station-side coda-Q results show common lower values around the Salton Sea, a geothermal region, consistent with previous coda at lower frequency (< 4 Hz) and direct wave attenuation studies (Aki, 1996; Hauksson and Shearer, 2006). A difference between direct and coda wave studies is seen in the region of the Chino Basin and San Gabriel Valley, where S-wave attenuation (Q_S) is low (Hauksson and Shearer, 2006), which is consistent with our source-side attenuation (see Figure 5.9), however, station coda-Q is high (Aki, 1996), also consistent with our results (see Figure 5.7).

In contrast to most previous studies, which focus on receiver-side Q_C variations, here we consider two attenuation terms, source-side attenuation (Q_C^S) and station-side attenuation (Q_C^R). Because any increase in the number of model parameters in an inversion should lead to a better fit, it is important to examine how misfit varies for different model parameter choices. Table 1 lists misfit errors for different coda-Q models, including purely source-side and receiver-side Q_C models. At lower frequencies (1–2 and 2–4 Hz), the station-side Q_C model fits better than the source-side Q_C model, even though it has fewer parameters (i.e., the number of stations is smaller than the number of events). In contrast, at high frequency (8–16 Hz), the source-side Q_C model fits better. However, even for the better-fitting models, the differences in the misfit errors are very small, and using source- or station-side Q_C terms yields only slightly better fits than those achieved with a uniform Q_C model. Despite these small changes in fit, it is clear that the Q_C terms are measuring a real property of the crust, given the spatial coherence seen in the maps of Figures 5.7 and 5.9. The small changes in misfit occur because of the large scatter in coda decay for individual records and the fact that the average coda decay is mostly accounted for with the geometrical spreading term, such that Q_C is relatively large (i.e., $2\pi f/Q_C$ is consistently small).

To illustrate the importance of each part of equation (5.6), we rewrite the misfit function as,

$$err = \frac{\sqrt{\sum_{i,j,k}(\hat{e}_{ij}(t_k) + \alpha \log t_k - \bar{c} - \delta s_i - \delta r_j + \bar{q} + \delta q_i^S + \delta q_j^R)^2}}{\sqrt{\sum_{i,j,k}\hat{b}_{ij}^2(t_k)}}. \tag{5.20}$$

where the $\bar{c}$ is the mean value of the total source (s) and station (r) amplitude terms, δs and δr are the removed mean source and station amplitude terms, similarly, $\bar{q}$ is the mean value of the total Q_C terms, and δq^S and δq^R are the removed mean source-side and station-side Q_C terms. We remove one term on the right-hand side from the equation (5.20) each time and compute the misfit errors, which are listed in Table 2. The geometric spreading term is the most important part of the inverse problem, and the source amplitude term, station amplitude term and the mean Q_C term are important in the inversion. Considering the number of events is much larger than than the number of stations, the residuals for the synthetics containing only the source amplitude terms are smaller than those containing only the station amplitude terms, as expected. For the Q_C terms, similar to Table 1, the uniform mean Q_C terms mostly explain the observations and including the source-side and/or station-side Q_C terms does not improve the fit very much. Also, comparing the misfit errors after removing different Q_C terms, it is difficult to tell whether the source- or station-side Q_C term dominates the inversion, so we prefer the both-side Q_C model in our MEMSM from both the physical and mathematical explanations.

When solving equation (5.6), we only keep the station-side attenuation terms. We find the attenuation Q_C is almost the same as the Q_C measured by SSMEM for each station with error less than 0.1%. However, our MEMSM approach provides an additional three useful parameters, the source and station amplitude terms together with source-side Q_C. To validate that MEMSM is a consistent and robust method, we compare the source amplitude terms and station amplitude terms between the both-side Q_C attenuation model, the source-side model, and the station-side model, as shown in Figure 5.12 and 5.13, respectively. Generally, the source and station amplitude terms are relatively consistent regardless of differing Q_C attenuation models, especially for the low-frequency bands ($<$ 8 Hz). For the high-frequency band (8–16 Hz), we find larger discrepancies between the both-side Q_C and station-side Q_C models for the source amplitude terms and between the both-side Q_C and source-side Q_C models for the station amplitude terms. This is caused by the weaker signal-to-noise ratio in this frequency band, especially for small earthquakes. Also, analysis of the source amplitude terms indicates that the source spectra calibrated from the source amplitude terms are consistent for the low frequency bands ($<$ 8 Hz) regardless of different Q_C attenuation models.

Jin and Aki (2005) point out the coincidence between low Q_C and high dilatational strain rate (< 4 Hz) assuming the brittle-ductile interaction hypothesis of earthquake loading by plate-driving force in Japan. Here, we examine this coincidence in southern California. The strain rate data are derived from the Community Geodetic Model (CGM) (Sandwell and Wessel, 2016). Similar to Jin and Aki (2005), we compute the dilatational strain rate ($e_{xx} + e_{yy}$) (see Figure 5.14 a,b). To better illustrate the comparison between Q_C and dilatational strain rate, we interpolate the dilatational strain rate based on the station locations (see Figure 5.14 c,d). From this comparison of Q_C and dilatational strain rate in Southern California, we do not find a clear correlation between Q_C and dilatational strain rate. In Japan, the Niigata-Kobe Tectonic Zone (NKTZ) is a high strain rate zone where the dilatational strain rate is an order of magnitude larger than the surrounding region and NKTZ is also a volcanic and geothermal region. However, in southern California, the background tectonics is strike-slip, compared to the convergence tectonics in Japan. The shear strain rate is much larger than dilatational strain rate and the dilatational strain rate is spatially smoother in southern California. These factors may result in no coincidence between low Q_C and dilatation strain rate in southern California.

5.6 Conclusion

In summary, based on a standard model for coda energy decay, we invert for separate source, station and coda attenuation terms in the logarithmic domain. We develop a method to use a representative expression of coda waves as the data vector to greatly reduce the size of the least-squares inverse problem. Applying our method to data from southern California in four different frequency bands, we obtain source amplitude terms related to coda magnitude and source spectra, station amplitude terms related to site effects, and coda Q terms related to lateral variations in scattering and attenuation. Our approach provides an efficient, robust, and self-consistent method to simultaneously determine coda-Q, earthquake magnitude, and site amplification.

Acknowledgments

We thank the personnel of the USGS/Caltech Southern California Seismic Network who pick and archive the seismograms and the Southern California Earthquake Center (SCEC) for distributing the data. This research was funded by USGS grant G15AP00094 and by SCEC. The refined catalog is available at http://scedc.caltech.edu/research-tools/downloads.html. The picked arrival times and seismograms are downloaded by using the Seismogram Transfer Program (STP), which is available at http://scedc.caltech.edu/research-tools/stp-index.html. We also express our gratitude to the two anonymous reviewers for their suggestions to improve this manuscript.

Chapter 5, in full, is a reprint of the material as it appears in Journal of Geophysical Research: Solid Earth: Wang W.and Shearer P., 2019, “An improved method to determine coda-*Q*, earthquake magnitude and site amplification: theory and application to southern California”,*Journal of Geophysical Research: Solid Earth*, 124(1), 578-598. The dissertation author is the primary investigator and author of this paper.

Appendix

The least-square solution for over-determined inverse problem $\mathbf{b} = \mathbf{Gm}$ is,

$$\mathbf{m} = (\mathbf{G^T G})^{-\mathbf{1}}(\mathbf{G^T b}). \tag{5.21}$$

For an arbitrary coda waveform, the equation (5.4) can be expressed as,

$$\begin{bmatrix} b(t_1) \\ b(t_2) \\ \vdots \\ b(t_k) \end{bmatrix} = \begin{bmatrix} a(t_1) \\ a(t_2) \\ \vdots \\ a(t_k) \end{bmatrix} + \begin{bmatrix} \log(t_1) \\ \log(t_2) \\ \vdots \\ \log(t_k) \end{bmatrix} \alpha = \begin{bmatrix} 1 \\ 1 \\ \vdots \\ 1 \end{bmatrix} C + \begin{bmatrix} t_1 \\ t_2 \\ \vdots \\ t_k \end{bmatrix} q = \begin{bmatrix} 1t_1 \\ 1t_2 \\ \vdots \\ 1t_k \end{bmatrix} \begin{bmatrix} C \\ q \end{bmatrix} \tag{5.22}$$

$$\mathbf{b} = \mathbf{Gm}. \tag{5.23}$$

And the corrected data vector is expressed as,

$$\hat{\mathbf{b}} = \mathbf{G}(\mathbf{G^T G})^{-\mathbf{1}}\mathbf{G^T b}. \tag{5.24}$$

The difference vector n between the data vector $\mathbf{b}$ and corrected data vector $\hat{\mathbf{b}}$ is defined as,

$$\mathbf{n} = \mathbf{b} - \hat{\mathbf{b}} = \mathbf{b} - \mathbf{G}(\mathbf{G^T G})^{-\mathbf{1}}\mathbf{G^T b}. \tag{5.25}$$

The difference vector $\mathbf{n}$ yields $\mathbf{G^T n} = \mathbf{0}$. Given $(\mathbf{G^T G})$ is invertable, which is valid in this study, the proof is as below,

$$\mathbf{G^T n}{=}\mathbf{G^T b} - \mathbf{G^T G}(\mathbf{G^T G})^{-\mathbf{1}}\mathbf{G^T b} = \mathbf{G^T b} - \mathbf{G^T b} = \mathbf{0} \tag{5.26}$$

$$= [\mathbf{g_1^T} \quad \mathbf{g_2^T}]\mathbf{n} = \begin{bmatrix} 0 \\ 0 \end{bmatrix}, \tag{5.27}$$

where, $\mathbf{g_1^T} = [1 \quad 1 \quad \cdots \quad 1]^T$ and $\mathbf{g_2^T} = [t_1 \quad t_2 \quad \cdots \quad t_k]^T$.

The solution for the inverse problem $\hat{\mathbf{b}} = \mathbf{G}\hat{\mathbf{m}}$ is,

$$\hat{\mathbf{m}}{=}(\mathbf{G^T G})^{-\mathbf{1}}(\mathbf{G^T}\hat{\mathbf{b}}) = (\mathbf{G^T G})^{-\mathbf{1}}\mathbf{G^T}(\mathbf{b} - \mathbf{n}) = (\mathbf{G^T G})^{-\mathbf{1}}\mathbf{G^T b} - (\mathbf{G^T G})^{-\mathbf{1}}\mathbf{G^T n} \tag{5.28}$$

$$= (\mathbf{G^T G})^{-\mathbf{1}}\mathbf{G^T b} = \mathbf{m}. \tag{5.29}$$

This solution indicates for any single coda wave, the solutions for both raw data vector and corrected data vector are the same. Furthermore, we prove this conclusion is still valid for multiple traces as the equation (5.6). The equation (5.6) can be rewritten as,

$$\begin{bmatrix} \mathbf{b_{11}} \\ \mathbf{b_{12}} \\ \vdots \\ \mathbf{b_{nm}} \end{bmatrix} = \left[\begin{array}{cccc|cccc|cccc} \mathbf{g_1} & 0 & \cdots & 0 & \mathbf{g_1} & 0 & \cdots & 0 & \mathbf{g_2} & 0 & \cdots & 0 \\ \mathbf{g_1} & 0 & \cdots & 0 & 0 & \mathbf{g_1} & \cdots & 0 & 0 & \mathbf{g_2} & \cdots & 0 \\ \vdots & \vdots & \vdots & \vdots & \vdots & \vdots & \vdots & \vdots & \vdots & \vdots & \vdots & \vdots \\ 0 & 0 & \cdots & \mathbf{g_1} & 0 & 0 & \cdots & \mathbf{g_1} & 0 & 0 & \cdots & \mathbf{g_2} \end{array}\right] \begin{bmatrix} \mathbf{s} \\ \mathbf{r} \\ \mathbf{q} \end{bmatrix} \tag{5.30}$$

$$\mathbf{b} = \widetilde{\mathbf{G}}\mathbf{m} \tag{5.31}$$

where $\widetilde{\mathbf{G}}$ is used to distinguish from $\mathbf{G}$ in equation (A5.3), the vector $\mathbf{g_1}$ and $\mathbf{g_2}$ are the same as those in equation (A5.7), $\mathbf{s}$, $\mathbf{r}$ and $\mathbf{q}$ are the source amplitude term, station amplitude term and attenuation term vectors. It is noted here we do not separate the attenuation terms into the source-and station-side attenuation terms, since the proof is quite similar and the results here are valid. For an arbitrary single coda waveform, we have proven the difference vector $\mathbf{n} = \mathbf{b} - \hat{\mathbf{b}}$ yields $\widetilde{\mathbf{G}}^{\mathbf{T}}\mathbf{n} = \mathbf{0}$. Here we will expand this result to multiple traces based on equation (5.6),

$$\widetilde{\mathbf{G}}^{\mathbf{T}}\mathbf{n}=\left[\begin{array}{c} \mathbf{g_1}\mathbf{g_1}\cdots 0 \\ 0\ 0\cdots 0 \\ \vdots\ \vdots\cdots\vdots \\ 0\ 0\cdots\mathbf{g_1} \\ \hline \\ \mathbf{g_1}\ 0\cdots 0 \\ 0\ \mathbf{g_1}\cdots 0 \\ \vdots\ \vdots\cdots\vdots \\ 0\ 0\cdots\mathbf{g_1} \\ \hline \\ \mathbf{g_2}\ 0\cdots 0 \\ 0\ \mathbf{g_2}\cdots 0 \\ \vdots\ \vdots\cdots\vdots \\ 0\ 0\cdots\mathbf{g_2} \end{array}\right] \left[\begin{array}{c} \mathbf{b_{11}} - \hat{\mathbf{b}}_{\mathbf{11}} \\ \mathbf{b_{12}} - \hat{\mathbf{b}}_{\mathbf{12}} \\ \vdots \\ \mathbf{b_{nm}} - \hat{\mathbf{b}}_{\mathbf{nm}} \end{array}\right] \tag{5.32}$$

(5.33)

$$\widetilde{\mathbf{G}}^{\mathbf{T}}\mathbf{n} = \begin{bmatrix} \mathbf{g_1}\mathbf{g_1}\cdots 0 \\ 0\ \ 0\cdots 0 \\ \vdots\ \ \vdots\cdots\vdots \\ 0\ \ 0\cdots\mathbf{g_1} \\ \hline \\ \mathbf{g_1}\ 0\cdots 0 \\ 0\ \mathbf{g_1}\cdots 0 \\ \vdots\ \ \vdots\cdots\vdots \\ 0\ \ 0\cdots\mathbf{g_1} \\ \hline \\ \mathbf{g_2}\ 0\cdots 0 \\ 0\ \mathbf{g_2}\cdots 0 \\ \vdots\ \ \vdots\cdots\vdots \\ 0\ \ 0\cdots\mathbf{g_2} \end{bmatrix} \begin{bmatrix} \mathbf{n_{11}} \\ \mathbf{n_{12}} \\ \vdots \\ \mathbf{n_{nm}} \end{bmatrix} = \begin{bmatrix} \sum_i \mathbf{g_1}\mathbf{n_{1i}} \\ \sum_i \mathbf{g_1}\mathbf{n_{2i}} \\ \vdots \\ \sum_i \mathbf{g_1}\mathbf{n_{ni}} \\ \hline \\ \sum_i \mathbf{g_1}\mathbf{n_{i1}} \\ \sum_i \mathbf{g_1}\mathbf{n_{i2}} \\ \vdots \\ \sum_i \mathbf{g_1}\mathbf{n_{im}} \\ \hline \\ \sum_i \mathbf{g_2}\mathbf{n_{i1}} \\ \sum_i \mathbf{g_2}\mathbf{n_{i2}} \\ \vdots \\ \sum_i \mathbf{g_2}\mathbf{n_{im}} \end{bmatrix} = 0 \tag{5.34}$$

$$\hat{\mathbf{m}} - \mathbf{m} = (\widetilde{\mathbf{G}}^{\mathbf{T}}\widetilde{\mathbf{G}})^{-\mathbf{1}}\widetilde{\mathbf{G}}^{\mathbf{T}}\hat{\mathbf{b}} - (\widetilde{\mathbf{G}}^{\mathbf{T}}\widetilde{\mathbf{G}})^{-\mathbf{1}}\widetilde{\mathbf{G}}^{\mathbf{T}}\mathbf{b} = (\widetilde{\mathbf{G}}^{\mathbf{T}}\widetilde{\mathbf{G}})^{-\mathbf{1}}\widetilde{\mathbf{G}}^{\mathbf{T}}(\hat{\mathbf{b}} - \mathbf{b}) \tag{5.35}$$

$$= (\widetilde{\mathbf{G}}^{\mathbf{T}}\widetilde{\mathbf{G}})^{-\mathbf{1}}\widetilde{\mathbf{G}}^{\mathbf{T}}\mathbf{n} = \mathbf{0} \tag{5.36}$$

Here, we have proven that when we used the corrected data vector $\hat{\mathbf{b}}$, we can get the same solution.

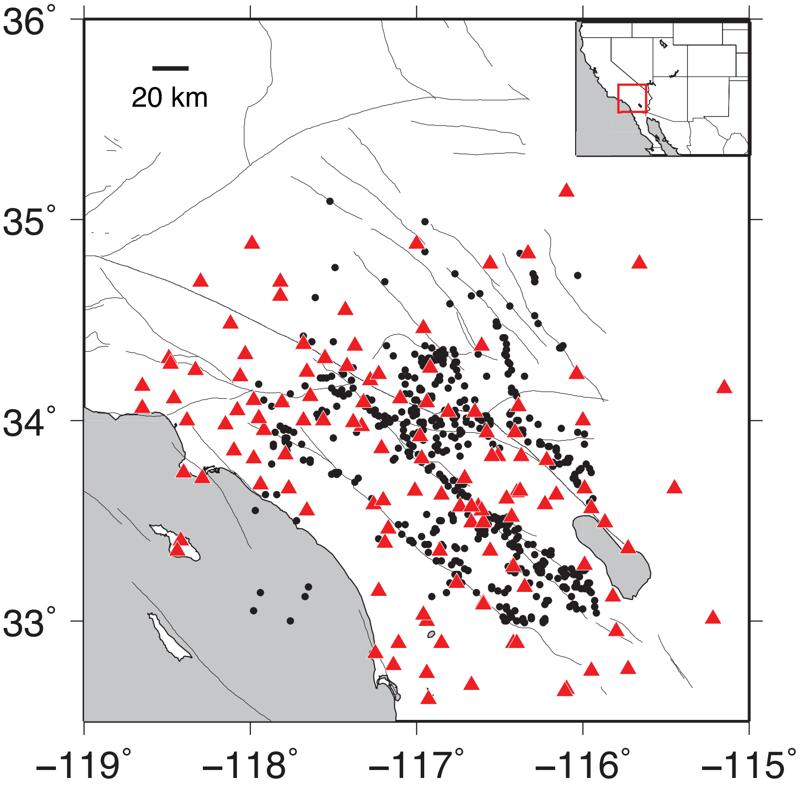

Figure 5.1: Locations of earthquakes and stations used in this study. The event epicenters are shown as black dots and the station locations are shown as red triangles. Quaternary faults are depicted as light black curves. The red box in the top right plot indicates our study region in the western U.S. map.

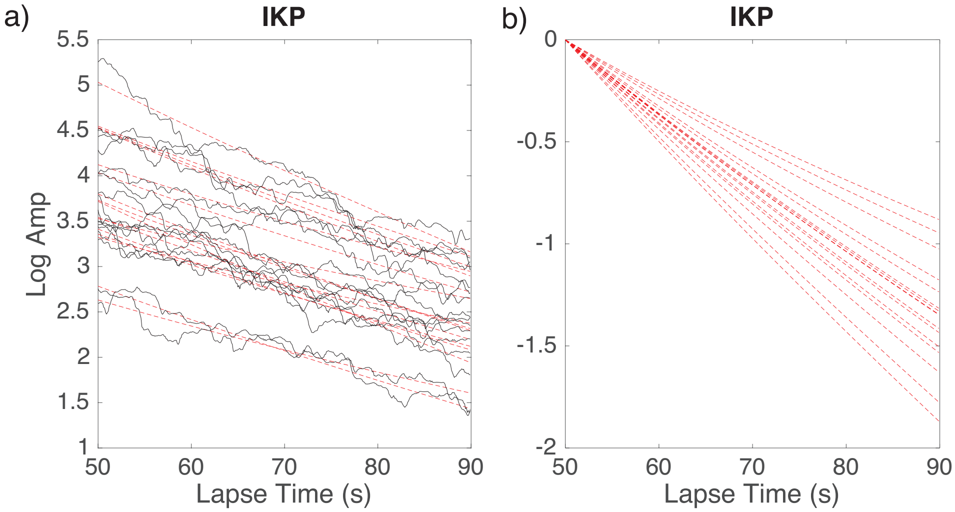

Figure 5.2: Observed coda energy decay curves at station IKP for different earthquakes at 2–4 Hz. (a) shows mean-squared coda amplitudes (black lines) and the best-fitting curves (red dashed lines) using equation (5.5). (b) shows the difference of the slopes of the best-fitting energy decay curves.

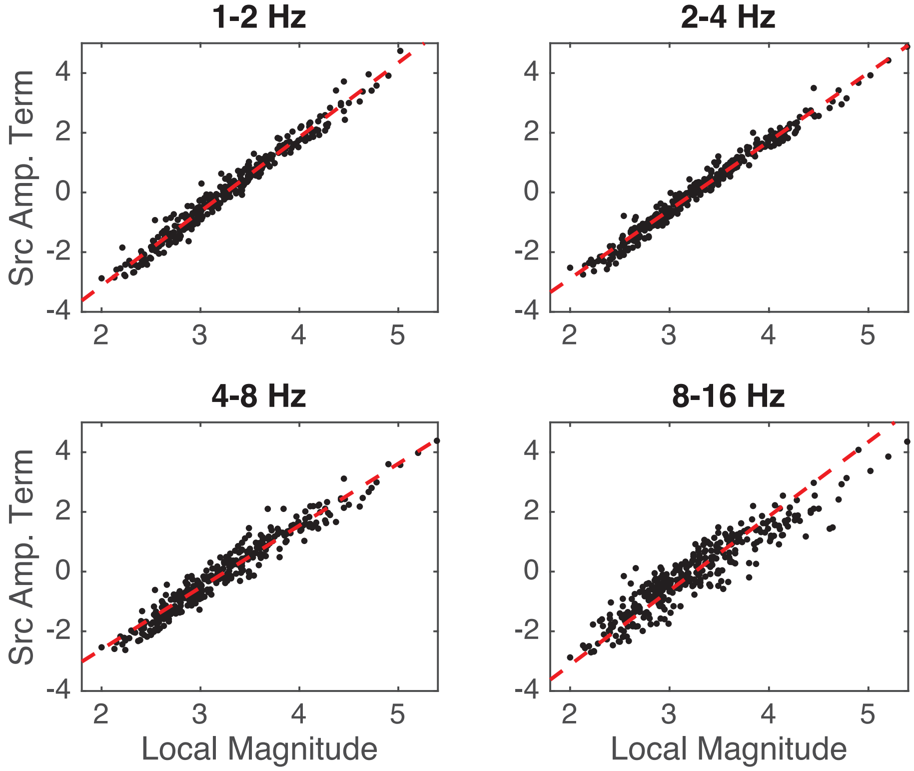

Figure 5.3: Uncorrected demeaned source amplitude terms versus catalog magnitudes at 1–2, 2–4, 4–8, and 8–16 Hz frequency bands. The red dashed lines show the best-fitting linear regression between source amplitude terms and local magnitudes.

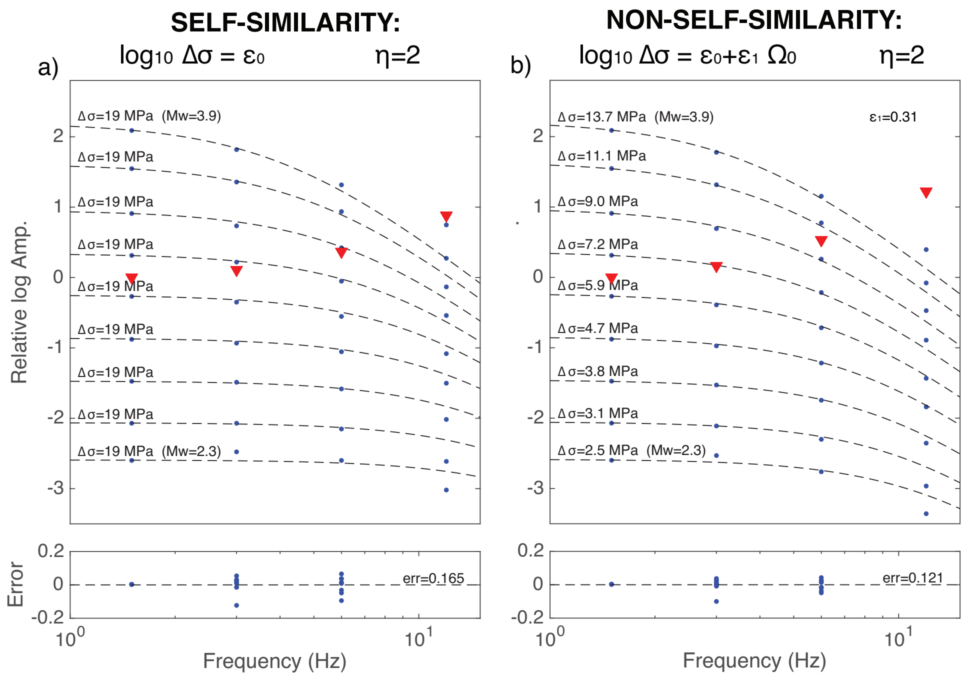

Figure 5.4: EGF-corrected, stacked source spectra from the source amplitude terms at 1–2, 2–4, and 4–8 Hz for (a) self-similar and (b) non-self-similar source models and their misfit with respect to a Brune-type source spectrum. The blue dots indicate the EGF-corrected source amplitude terms. Red triangles show the EGF. The black dashed lines indicate the theoretical source models.

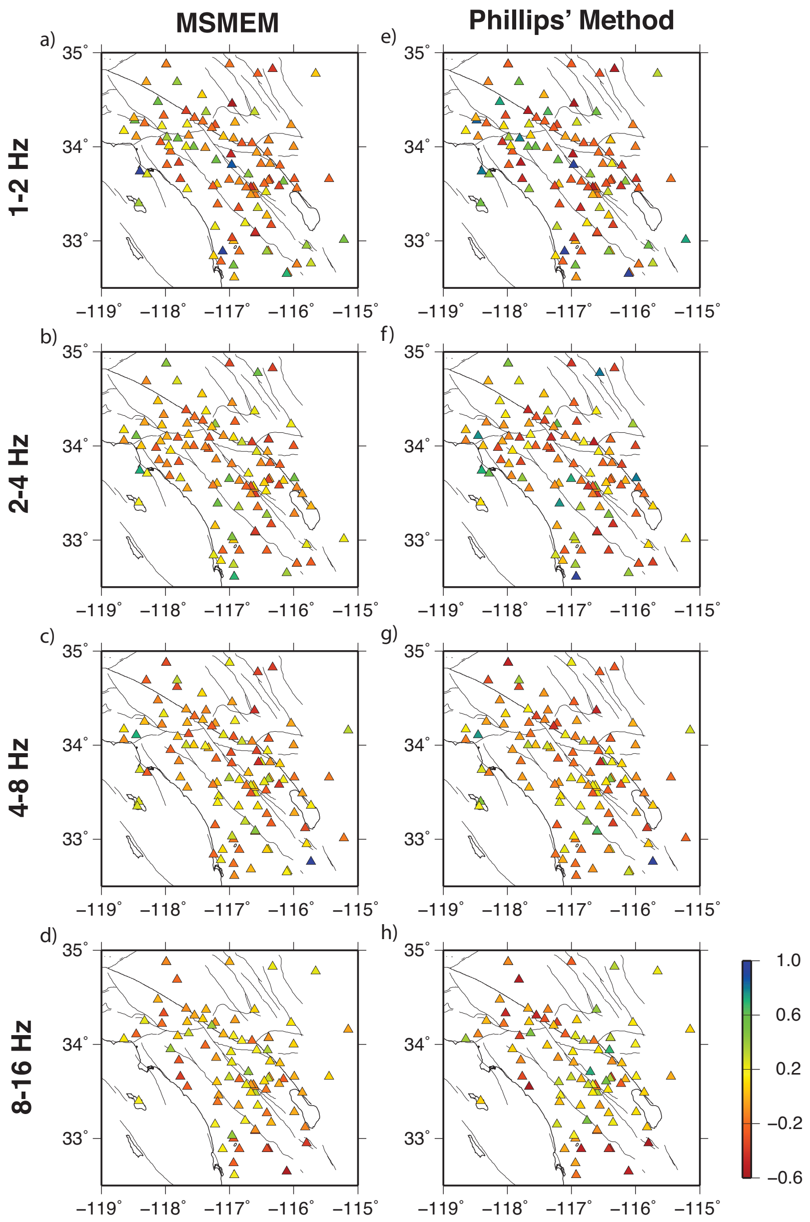

Figure 5.5: Comparisons of site amplification terms between our MSMEM and the method of Phillips and Aki (1986). The colors show the site amplification (log 10) relative to the 'average station,' with amplification factors ranging from 0.25 (dark red) to 10 (dark blue). (a)–(d) show the site amplification effect from MSMEM at 1–2, 2–4, 4–8 and 8–16 Hz; (e)–(h) show results from the method of Phillips and Aki (1986).

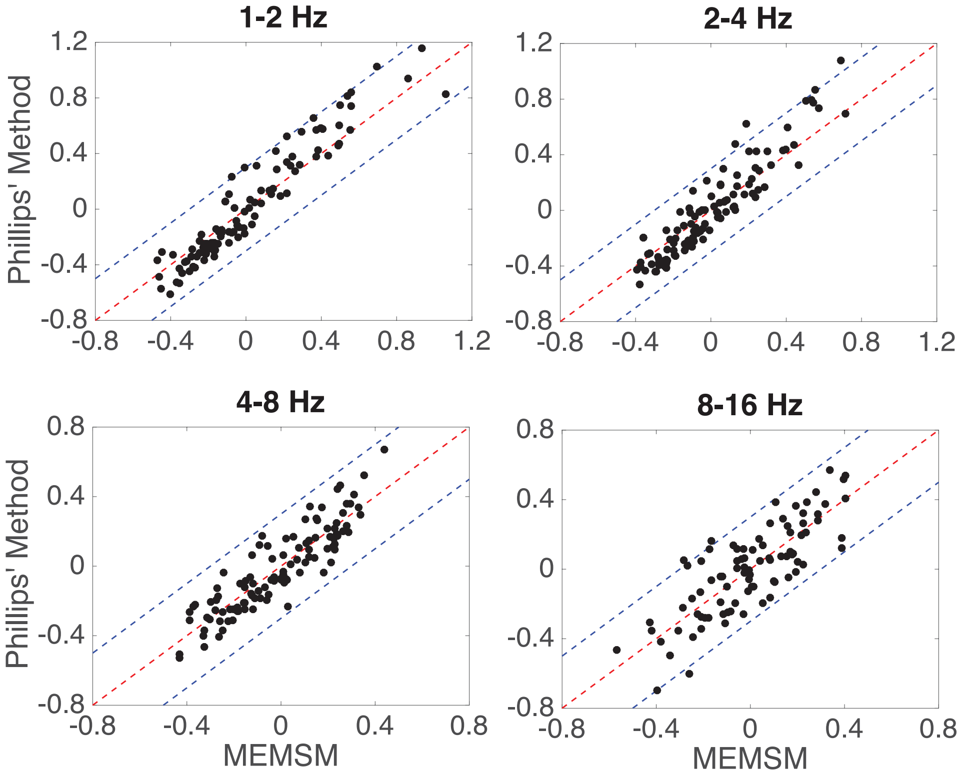

Figure 5.6: Comparisons of site amplification between our MSMEM and the method of Phillips and Aki (1986) at 1–2, 2–4, 4–8 and 8–16 Hz. The reference red and blue dashed lines show identical values and differences of ±0.3, respectively.

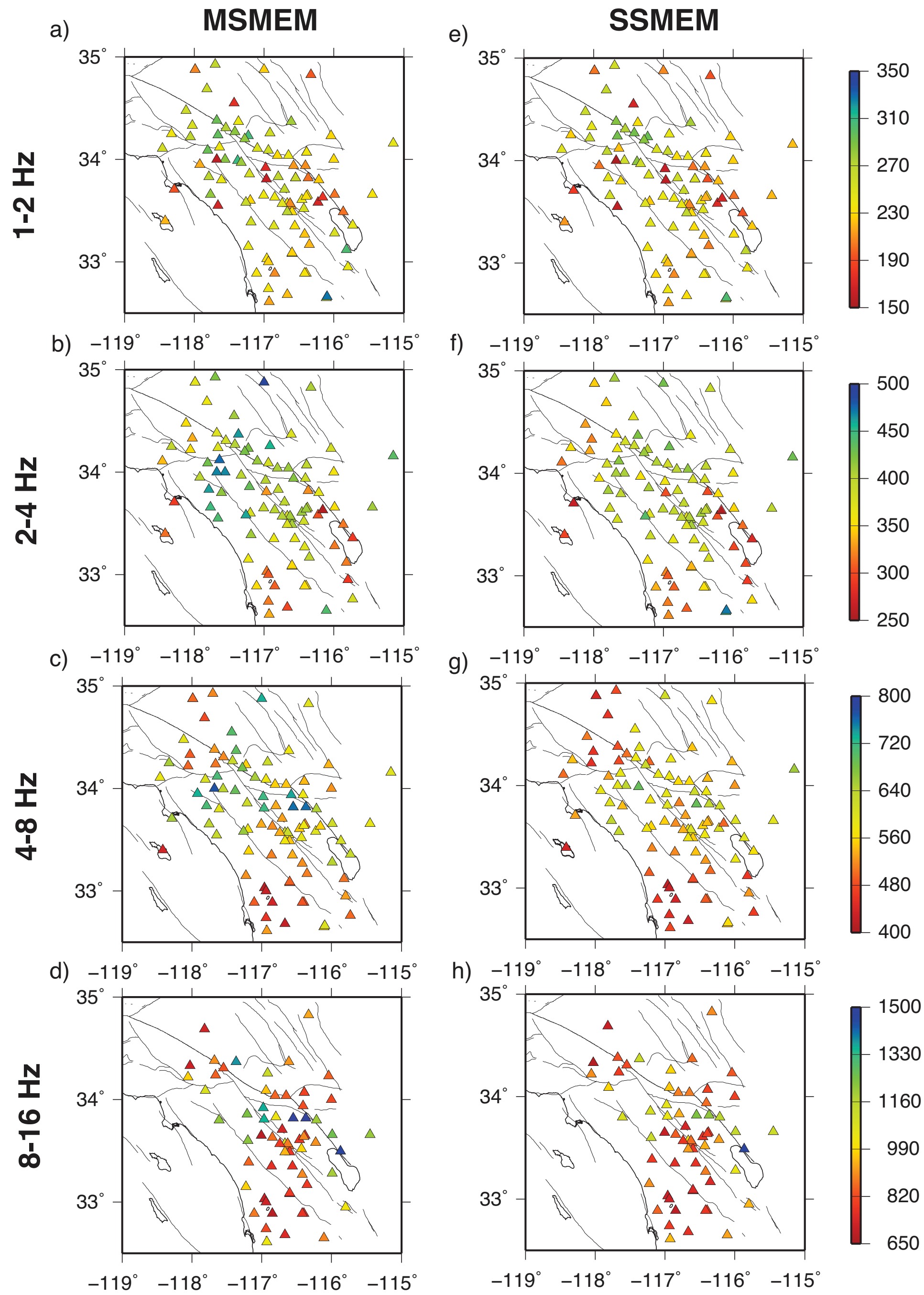

Figure 5.7: Spatial distribution of the station-side coda attenuation Q_C at 1–2, 2–4, 4–8 and 8–16 Hz. The scale of Q value is shown at the right-hand side of each row.

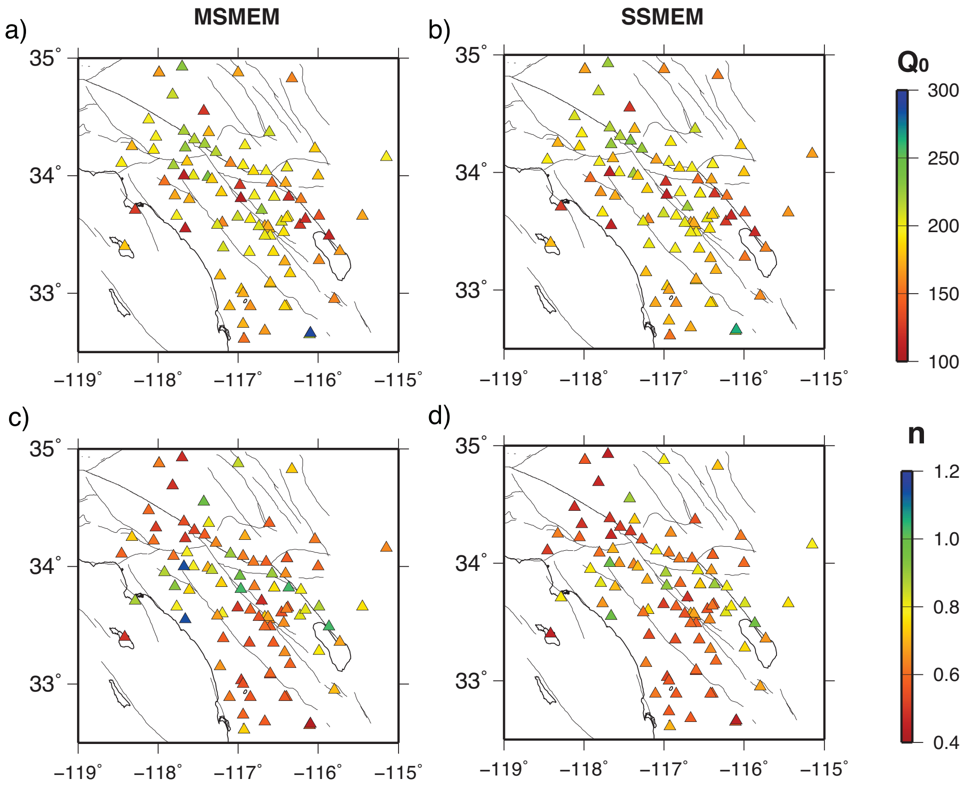

Figure 5.8: Spatial distribution of the station-side coda attenuation Q_C at 1 Hz and power n. The scale of Q value is shown at the right-hand side of each subplot.

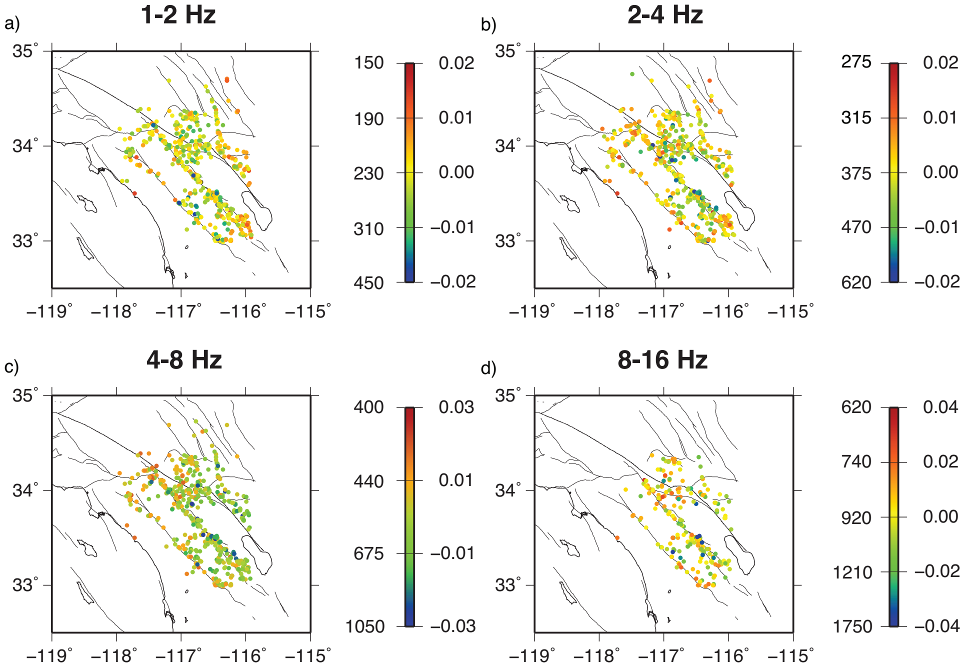

Figure 5.9: Spatial distribution of the source-side coda attenuation terms $-2\pi f/Q_C^S$ or Q_C^S at 1–2, 2–4, 4–8 and 8–16 Hz. The scale of the attenuation terms is shown at the right-hand side of each subplot. The color bar is linearized in $-2\pi f/Q_C^S$ and corresponding Q_C^S.

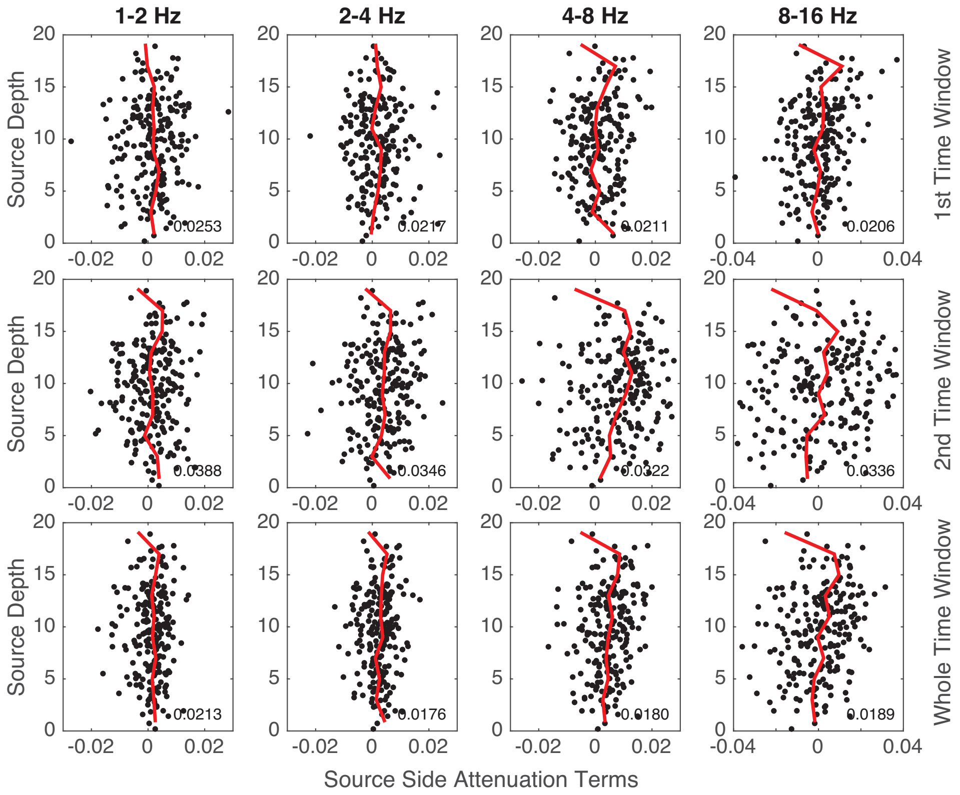

Figure 5.10: Relation between the source-side coda attenuation terms $-2\pi f/Q_C^S$ with the source depths at 1–2, 2–4, 4–8 and 8–16 Hz. The first row shows source-side coda attenuation terms for the time window 50–70 s, the second row shows the results for the time window 70–90 s and the third row shows the results for the time window 50-90 s. Each black dot represents an event and red lines indicate the median values of the source-side coda attenuation terms binned at 0.2 intervals in coda magnitude.

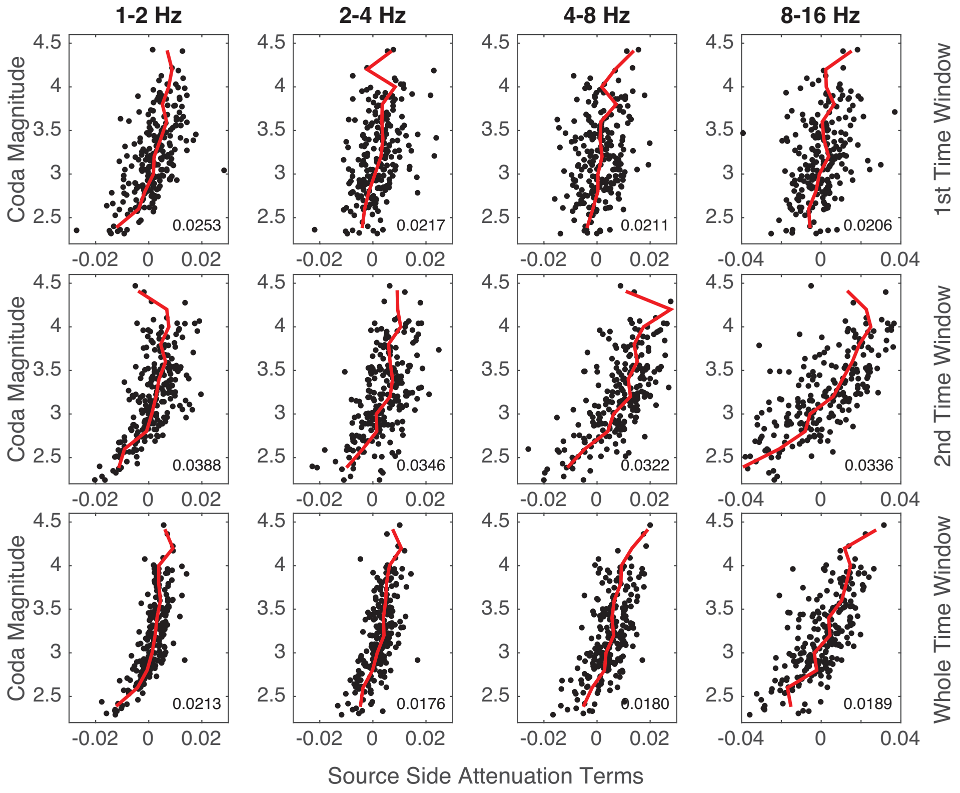

Figure 5.11: Relation between the source-side coda attenuation terms $-2\pi f/Q_C^S$ with the coda magnitudes at 1–2, 2–4, 4–8 and 8–16 Hz. The first row shows the results of source-side coda attenuation terms for the time window 50–70 s, the second row shows the results for the time window 70–90 s and the third row shows the results for the time window 50-90 s. Each black dot shows the result for each event and red lines indicate the median values of the source-side coda attenuation terms binned at 0.2 interval in coda magnitude.

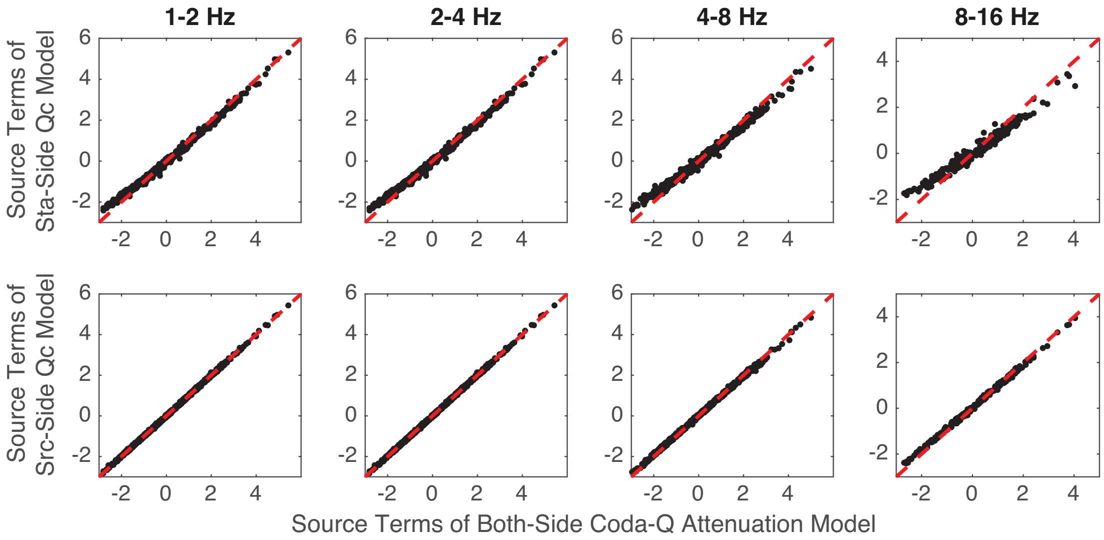

Figure 5.12: Comparisons of the source amplitude terms between both-side MSMEM and station-side MSMEM, source-side MSMEM at 1–2, 2–4, 4–8 and 8–16 Hz, respectively. The top four figures show comparisons of source amplitude terms between both-side MSMEM and station-side MSMEM; the bottom figures show comparisons of station amplitude terms between both-side MSMEM and source-side MSMEM. Each black dot represents an event and the red dashed lines indicate identical results.

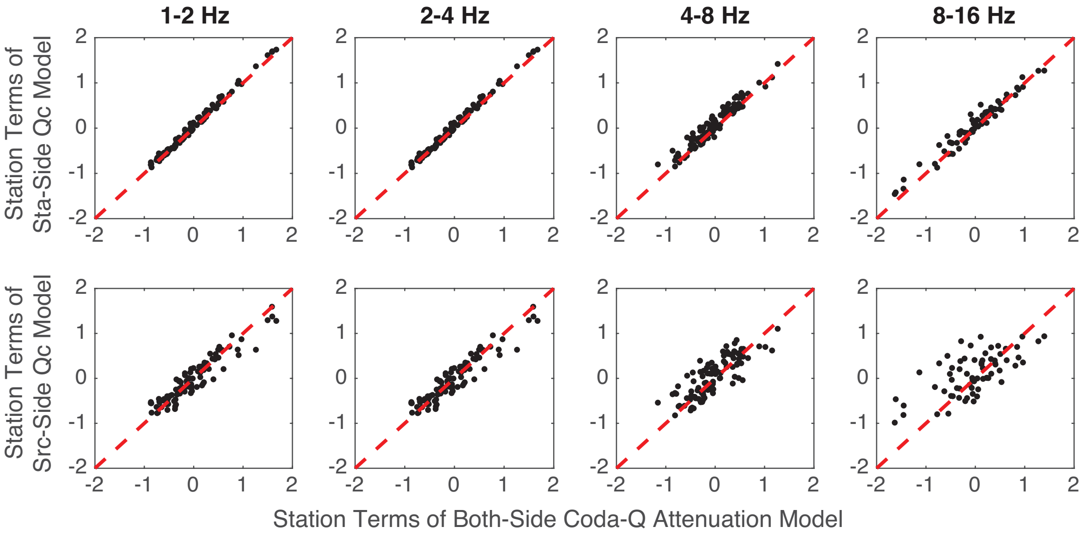

Figure 5.13: Comparisons of the station amplitude terms from both-side MSMEM and station-side MSMEM, source-side MSMEM, the same as Figure 12 .

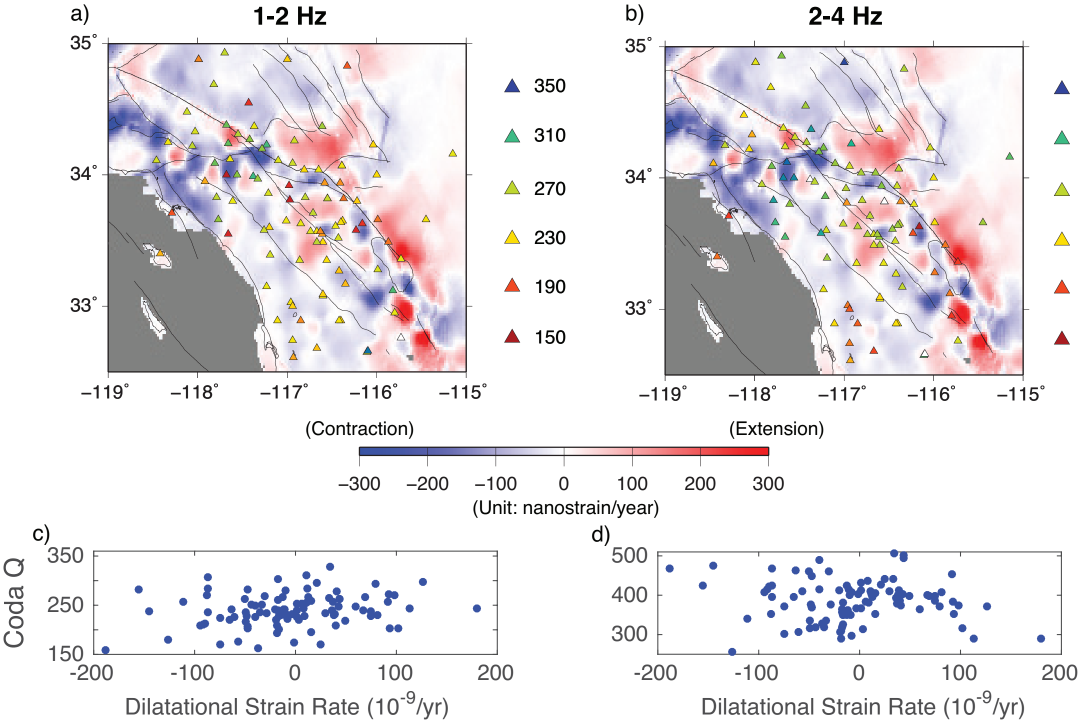

Figure 5.14: Comparisons of the coda attenuation Q_C with the dilatational strain rate in southern California at 1–2 and 2–4 Hz. (a) and (b) show the spatial distribution of the dilatational strain rate together with the spatial distribution of the Q_C at 1–2 and 2–4 Hz. (c) and (d) show the comparison of the Q_C and the interpolated dilatational strain rates at the same station locations.

Table 5.1: Misfit error table of the inversion problem for all the Q_C models

	1–2 Hz	2–4 Hz	4–8 Hz	8–16 Hz
No Q_C	0.0367	0.0391	0.0415	0.0639
Uniform Q_C	0.0248	0.0206	0.0191	0.0241
Source-side Q_C	0.0245	0.0203	0.0187	0.0229
Station-side Q_C	0.0244	0.0202	0.0186	0.0231
Both-side Q_C	0.0241	0.0199	0.0180	0.0214

Table 5.2: Misfit error table from removing each term on the right side of equation (5.20)

	1–2 Hz	2–4 Hz	4–8 Hz	8–16 Hz
All terms included	0.0241	0.0199	0.0204	0.0214
No geometric spreading	0.4000	0.4006	0.4050	0.4046
No $\bar{q}$, δq^S and δq^R	0.1696	0.2503	0.2869	0.3671
No $\bar{q}$	0.1625	0.2002	0.2667	0.3303
No δq^S and δq^R	0.0419	0.0376	0.0511	0.0772
No δq^S	0.0349	0.0311	0.0430	0.0570
No δq^R	0.0332	0.0303	0.0400	0.0647
No δs and δr	0.2607	0.2455	0.2355	0.2095
No δs	0.2271	0.2243	0.2247	0.1961
No δr	0.1128	0.0855	0.0755	0.0922

5.7 Supplementary Materials

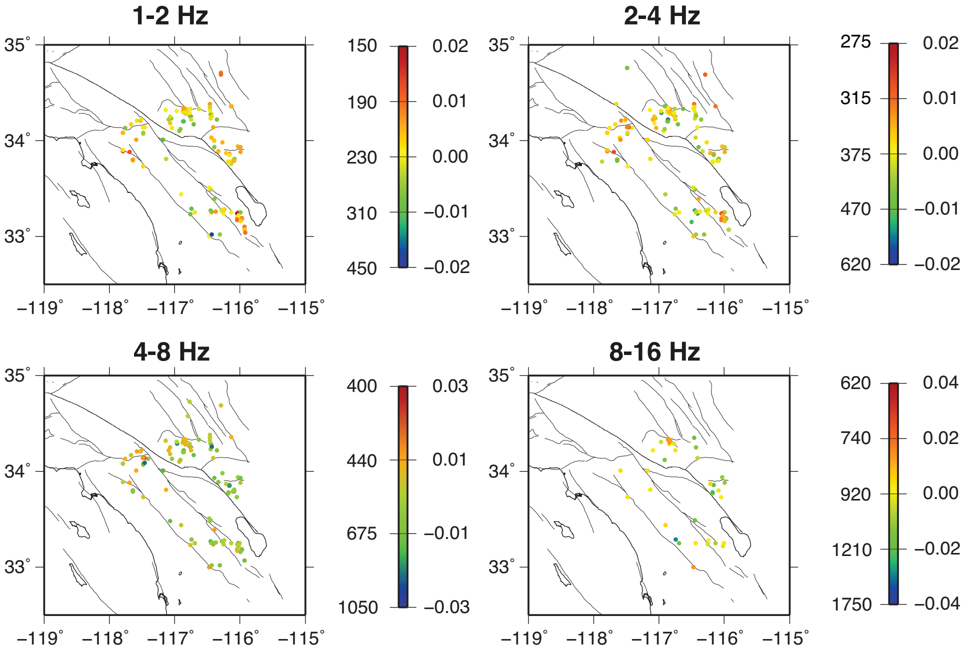

Figure S5.1: Spatial distribution of the source-side coda attenuation terms $-2\pi f/Q_C^S$ or Q_C^S at 1–2, 2–4, 4–8 and 8–16 Hz with source depth 0–5 km. The scale of the attenuation terms is shown at the right-hand side of each subplot. The color bar is linearized in $-2\pi f/Q_C^S$ and corresponding Q_C^S.

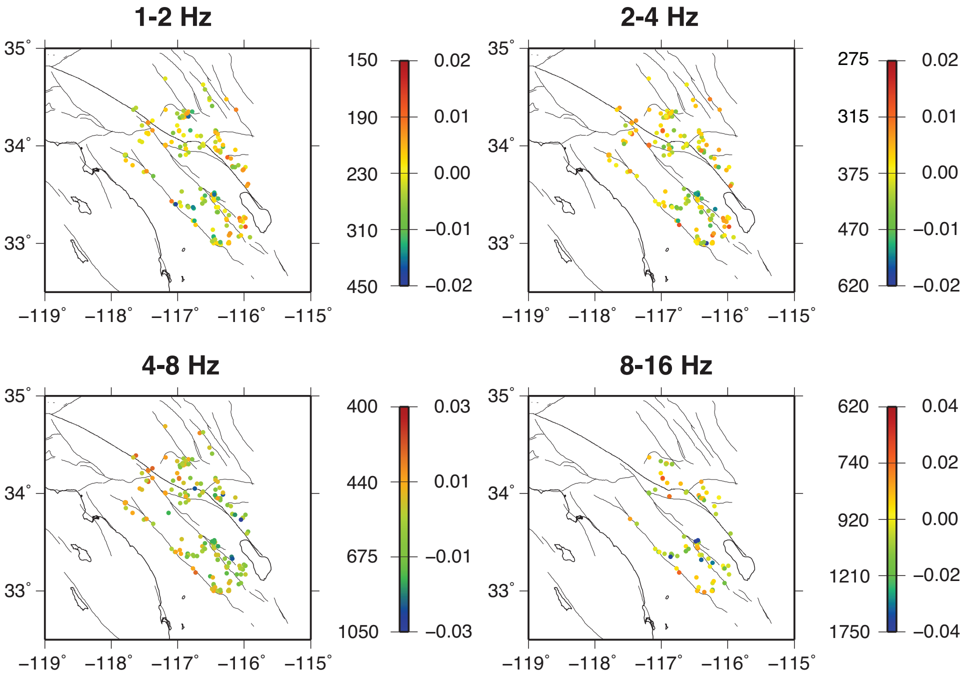

Figure S5.2: Spatial distribution of the source-side coda attenuation terms $-2\pi f/Q_C^S$ or Q_C^S at 1–2, 2–4, 4–8 and 8–16 Hz with source depth 5–10 km. The scale of the attenuation terms is shown at the right-hand side of each subplot. The color bar is linearized in $-2\pi f/Q_C^S$ and corresponding Q_C^S.

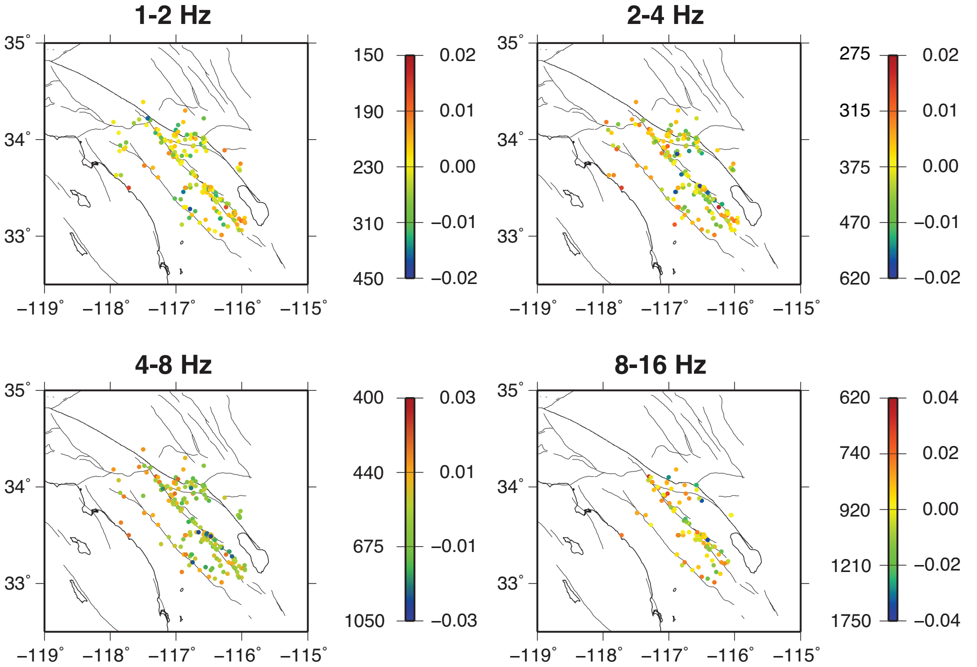

Figure S5.3: Spatial distribution of the source-side coda attenuation terms $-2\pi f/Q_C^S$ or Q_C^S at 1–2, 2–4, 4–8 and 8–16 Hz with source depth 10–15 km. The scale of the attenuation terms is shown at the right-hand side of each subplot. The color bar is linearized in $-2\pi f/Q_C^S$ and corresponding Q_C^S.

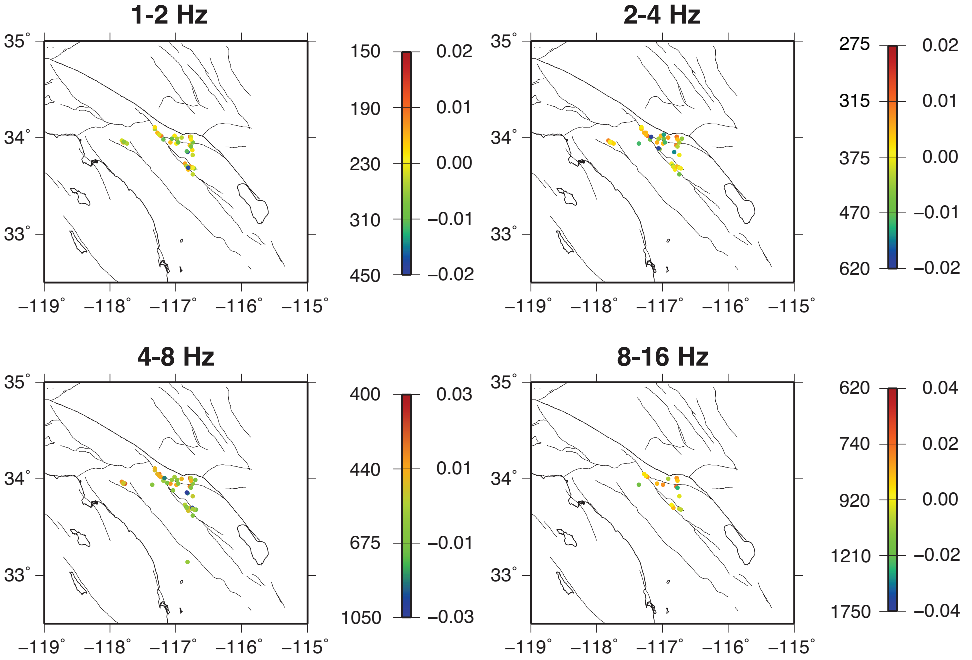

Figure S5.4: Spatial distribution of the source-side coda attenuation terms $-2\pi f/Q_C^S$ or Q_C^S at 1–2, 2–4, 4–8 and 8–16 Hz with source depth 15–20 km. The scale of the attenuation terms is shown at the right-hand side of each subplot. The color bar is linearized in $-2\pi f/Q_C^S$ and corresponding Q_C^S.

Chapter 6

Focal mechanism effects on S/P amplitude ratios in the San Bernardino region, southern California

Ground Motion Prediction Equations (GMPEs) for seismic hazard analysis have been developed for many regions, which account for earthquake magnitude, epicentral distance, and local site effects on peak ground motions. However, they typically do not include effects related to sampling different parts of the earthquake focal sphere, and the spatial distribution of observed peak amplitudes often fails to show a clear radiation pattern, especially at higher frequencies and longer ranges. Here, we investigate the effects of focal mechanisms on observed ground motions in the San Jacinto fault zone region of southern California. We identify clusters of earthquakes with similar strike-slip focal mechanisms and good azimuthal station coverage recorded by the combined Southern California Seismic Network and ANZA network and compute their S/P amplitude ratios. We examine how these S/P ratios, and their azimuthal patterns, vary with distance and frequency, finding that the radiation-pattern signature is clearest for measurements below 2 Hz. We model the observed peak absolute S/P amplitude ratios with a seismic phonon-based, Monte Carlo algorithm that includes intrinsic attenuation, P- and S-wave scattering based on random heterogeneity models, and multiple scattering. Using forward modeling, we achieve a reasonable fit to the observations using a model with von Karman type scattering (heterogeneity correlation length $a = 2$ km, fractional velocity heterogeneity $\varepsilon = 0.05$) and frequency-dependent ($Q = Q_0 f^{\eta}$) intrinsic attenuation ($Q_P = 250, Q_S = 312$ at 1.5 Hz and $\eta = 0.2$). Our preferred model has stronger P attenuation than S attenuation in both the scattering and intrinsic attenuation components.

6.1 Introduction

Ground motion prediction equations (GMPEs) have been developed and applied to many regions of the world (e.g. Boore and Joyner, 1982; Baltay and Beroza, 2013; Yabe and Ide, 2014). The equations account for the reduction in amplitude with distance by averaging the behavior of many different events to create empirical relations that can be used for strong ground motion prediction and earthquake early warning systems (Yabe et al., 2014; Bostock et al., 2015; Takemura et al., 2016, 2017). Currently, however, there is no consensus on the relative importance of factors such as geometrical spreading, intrinsic attenuation, and scattering, which is necessary for successfully developing 3-D physics-based GMPEs. The geometrical spreading term can be predicted fairly easily, at least for 1-D velocity models, but separating the effects of intrinsic and scattering attenuation is more challenging, and has involved application of multiple-lapse time window analysis (MLTWA) (Fehler et al., 1992; Jin et al., 1994; Padhy et al., 2007; Carcolé and Sato, 2010) and radiative transfer theory (RTT) (Przybilla et al., 2006, 2009; Eulenfeld and Wegler, 2016, 2017; Wang and Shearer, 2017; Zeng, 2017; Ogiso, 2018).

Most scattering studies have focused on the behavior of coda waves, but constraints on scattering can also be obtained from analysis of earthquake radiation patterns. Since Liu and Helmberger (1985) first noted the frequency-dependent apparent radiation pattern of S waves, a number of authors (Takemura et al., 2009, 2016, 2017; Yoshimoto et al., 2015) have analyzed the radiation patterns of P and/or S waves at high frequency (>1 Hz). These studies observe significant distortion of the radiation pattern, especially at higher frequencies (>4 Hz), where the amplitudes become more scattered with no clear azimuthal dependence. To model the observations, Takemura et al. (2009, 2017) applied 2D and 3D finite-difference methods to compute the effects of scattering within heterogeneous media on the radiation pattern. These studies found that a multiple scattering process caused by small-scale heterogeneity in the medium could account for the observed frequency- and distance-dependent changes in the radiation pattern.

Turning the problem around, a number of studies have used absolute P and S amplitudes (e.g. Ebel and Bonjer, 1990; Rögnvaldsson and Slunga, 1993; Schwartz, 1995; Nakamura et al., 1999) to help determine focal mechanisms. To better isolate radiation pattern effects from magnitude, geometrical spreading, attenuation, and especially the site effect, other studies have used S/P amplitude ratios (e.g. Kisslinger, 1980; Kisslinger et al., 1981; Julian and Foulger, 1996; Rau et al., 1996; Shen et al., 1997; Hardebeck and Shearer, 2003) to determine the focal mechanisms. The S/P amplitude ratios have also been used to discriminate between explosions and earthquakes (Kim et al., 1997; Houng and Hong, 2013; Houng, 2017; Pyle and Walter, 2019).

Here, we measure the peak absolute S/P amplitude ratios of a cluster of strike-slip earthquakes in the San Bernardino region of southern California over multiple frequency bands. The radiation pattern becomes more isotropic at higher frequencies and longer ranges, in agreement with previous work. We then apply a particle-based, Monte Carlo approach to forward model the energy flux at different distances from a double-couple source. This method has the advantage of including multiple non-isotropic scattering, conversions between P and S waves, and intrinsic attenuation. We obtain good fits to the peak absolute S/P amplitude ratio with von Karman type scattering and a frequency-dependent intrinsic attenuation model, and explore the implications of these results for P and S-wave attenuation mechanisms.

6.2 Dataset

We identify two clusters at the same location with different depths. The shallow cluster contains 33 earthquakes from 3 to 7 km depth and the deep cluster contains 40 earthquakes from 15 to 17 km depth with similar strike-slip focal mechanisms and good azimuthal station coverage (80 stations) recorded by the combined Southern California Seismic Network and ANZA network (Caltech and USGS, 1926; Vernon and Diego, 1982) (see Figure 6.1). The focal mechanisms are selected from a relocated catalog (Hauksson et al., 2012; Yang et al., 2012), and are determined using the HASH method developed by Hardebeck and Shearer (2002, 2003). This method searches for double-couple focal mechanism solutions to fit the polarities recorded by stations for each event and uses the S/P ratios as an additional constraint. We download three-component waveform data for stations within 100 km using the Seismogram Transfer Program (STP) available from the Southern California Earthquake Center (SCEC) and compute the squared root energy densities based on vector summation of the three components. The P and S amplitude levels are computed from the mean value within a 0.5 second time window centered at the maximum P or S wave amplitude, respectively. We filter the seismograms with a 4th-order zero-phase Butterworth filter for the following frequency bands: 1–2, 2–4, 4–8 and 8–12 Hz. The amplitudes decrease with hypocentral distance (see Figure 6.2). Figure 6.3 shows the amplitudes versus the differences between the strike directions of the fault planes and azimuths of the source-station pairs. The radiation pattern for the lower-frequency range (1–2 Hz) shows the expected four lobe pattern, but the observations are more scattered and the radiation pattern less clear at higher frequencies, particularly for the highest-frequency range (8–12 Hz) (see Figure S6.2 & S6.4). Since there is no difference in the S/P amplitude ratios for shallow and deep events (see Figure S6.1, S6.2 and S6.3), we use them together as our observations.

6.3 Monte Carlo Simulation

To investigate the radiation pattern behavior with distance and azimuth, we apply a particle-based, Monte Carlo method to synthesize the energy density. Monte Carlo simulation is a versatile and powerful approach for simulating scattering in complex models. Since Gusev and Abubakirov (1987) first introduced the Monte Carlo simulation in seismology to model S-wave scattering in a uniform whole space, many studies (Hoshiba, 1991, 1994, 1997; Margerin and Michel Capillo Van Tiggelen, 2000; Yoshimoto, 2000; Margerin and Nolet, 2003a,b) adopted this approach to model wave propagation in heterogeneous media. Here, we use the Monte Carlo scattering simulation described by Shearer and Earle (2004), adapted to include the source radiation pattern and a whole-space background model. The energy carried by each particle sprayed from the source is determined by wave type (P or S wave) and its corresponding radiation pattern for a double-couple source, following the equations in Aki and Richards (2002, p. 79, eq. 4.33). We assume that the total S-wave energy is 14 times the P-wave energy, following Wang and Shearer (2017).

In the Monte Carlo simulation, the scattering probabilities and scattering patterns depend on the random heterogeneity model. We adopt a stochastic random velocity model characterized by a von Karman-type power spectral density function (PSDF) in the wavenumber domain (Sato et al., 2012, p. 23),

$$P(m) = \frac{2\pi^{3/2}\Gamma(\kappa+3/2)\varepsilon^2 a^3}{\Gamma(\kappa)(1+a^2m^2)^{k+3/2}} \tag{6.1}$$

where m is the wavenumber, a is the correlation distance, describing the scale of the heterogeneity; ε is the root-mean-square (RMS) fractional velocity fluctuation; and κ is the Hurst parameter, which controls the relative proportion of large- and small-scale heterogeneity. We assume the Hurst number κ is equal to 0.3, following Wang and Shearer (2017) based on their analysis and modeling of coda waves in southern California. Note that this value is within the range 0.0–0.5 found in crustal studies (Frankel and Clayton, 1986; Przybilla et al., 2009; Bydlon and

Dunham, 2015; Savran and Olsen, 2016; Sato, 2019). The P-to-S velocity ratio is set to $\sqrt{3}$, i.e., a Poisson solid and the density/velocity perturbation scaling factor is 0.8 (Sato et al., 2012). In the simulation, the strength of the scattering can be described using the mean free path (Sato et al., 2012). In the computation, a scattering event occurs when the ray path length of the particle exceeds a random length set by randomly sampling an exponential distribution based on the mean free path. The scattering angle is randomly determined based on the physical scattering pattern. Since our energy flux is obtained from whole-space synthetics, we correct the synthetics to a half space assuming total reflection on the free surface, following Wegler (2004). The S/P amplitude ratios are computed from the energy flux and compared with the real data. Considering the bandpass frequency ranges are 1–2, 2–4, 4–8, and 8–12 Hz, we choose a centered frequency at each frequency range for the Monte Carlo simulations (i.e., 1.5, 3, 6, and 10 Hz).

6.4 Results

To model seismic wave propagation in a heterogeneous medium, we assume a uniform background P-wave velocity of 6.70 km/s and S-wave velocity of 3.87 km/s, values appropriate for the lower crust in southern California (below about 5 km depth). However, to obtain the most accurate possible take-off angles at the focal sphere for the radiation pattern, we compute ray paths based on a classic 1-D southern California velocity model (Hadley and Kanamori, 1977).

To select the best intrinsic and scattering models to model the S/P amplitude ratio (SPAR), we define a misfit measure err between the synthetics and observations as

$$err = \sum_{i,j,k,l} \left| \log_{10}\left(SPAR_{syn}(r_i, \phi_j, \theta_k, f_l)\right) - \log_{10}\left(SPAR_{obs}(r_i, \phi_j, \theta_k, f_l)\right) \right|, \tag{6.2}$$

where r, ϕ, θ, f are the distance, relative azimuth from the fault plan, takeoff angle, and frequency, respectively. In this study, we use the L1-norm misfit of the $\log_{10}(SPAR)$ to reduce the effect of outliers, since the observed S/P amplitude ratios are highly scattered. To fit the observations, we use frequency-dependent intrinsic attenuation parameters, i.e., $Q(f) = Q_0 \cdot f^{\eta}$, where Q_0 is the quality factor at 1 Hz and η is the frequency dependent exponent, based on previous studies, e.g., Carcolé and Sato (2010) and Lin and Jordan (2018). After extensive trial-and-error forward modeling, we show the predictions of our best-fitting model in Figures 6.4, 6.5, and 6.6, which is able to roughly fit the range dependence in the SPAR values over the different frequency bands. The intrinsic attenuation parameters are $Q_P = 250, Q_S = 312$ at 1.5 Hz, and $\eta = 0.2$. The scattering model is characterized by a von Karman ACF with correlation length $a = 2$ km and rms strength fluctuation $\varepsilon = 0.05$. This model is reasonably consistent with crustal results reported by previous studies, which are within the general range, $\varepsilon = 0.008 - 0.1$ and $a = 0.05 - 16$ km for the crust (Takemura et al., 2009, 2016, 2017; Bydlon and Dunham, 2015; Savran and Olsen, 2016; Wang and Shearer, 2017; Lin and Jordan, 2018; Sato, 2019).

6.5 Discussion and Conclusions

Overall, our model fits the S/P amplitude ratios reasonably well across the different frequency bands, although a few observations deviate from the synthetics. The focal mechanisms are obtained using the HASH method developed by Hardebeck and Shearer (2002, 2003). The focal mechanisms of the events are similar, but not identical, for our event clusters. This is why we plot the S/P amplitude observations versus station azimuth relative to the radiation pattern rather than versus absolute azimuth. However, if the scatter in the focal mechanisms were due to errors in the strike, dip and rake estimates, rather than true scatter in the mechanisms, this approach might be flawed. To test this possibility, we plotted the S/P ratio versus station azimuth (see Figure S6.3) and found much more scatter in the results. This suggests that it is indeed appropriate to correct for differences in the individual event focal mechanisms, as we have done here, but errors in the focal mechanisms or non-double-couple source components will add some uncertainty to interpretation of S/P amplitude ratio measurements. The computed takeoff angles are based on the choice of the seismic velocity model. In this study, we also tested a smoothed version of the standard Hadley-Kanamori model (Shearer, 1997). The difference in takeoff angles between these two models is not significant (Hardebeck and Shearer, 2002) and does not affect our final choice of attenuation model. We do not consider lateral or 3-D variations in the velocity and attenuation structure in southern California or any near-source structure, such as fractures or anisotropy (e.g. Hauksson and Shearer, 2006; Tape et al., 2010; Wang and Shearer, 2019).

Here we achieve a reasonable fit to the S/P ratios using a whole-space model. At the frequency range 1–2 Hz, we observe slightly smaller synthetic S/P ratios, but within one-standard deviation error (see Figure 6.5 & S6.4). We tested the effect of increasing our assumed source-radiated S-to-P energy ratio from 14 to 23.4, the value for identical P and S corner frequencies and a Poisson solid (Boatwright and Fletcher, 1984; Abercrombie, 1995), but found no significant difference (see Figure S6.6). Another reason for the S/P difference may be measurement error. Figure S6.5a and S6.7a illustrates that even if there is no attenuation, some individual measurements are much larger than the predictions. Considering these factors and our good fit at higher frequency ranges (>2 Hz), our model provides an acceptable overall fit to the observations (see Figure 6.5, 6.6 and S6.5).

Wang and Shearer (2017) found that a two-layer model was necessary to fit the distance-dependence of average coda-wave envelopes from local earthquakes in southern California, with stronger scattering and intrinsic attenuation in the upper 5.5 km than in the lower crust. In Figure 6.4b and 6.5b, we compare the observed S/P amplitude ratios to predictions (computed using the phonon code) for the two-layer model in Wang and Shearer (2017). The two-layer model generally under-predicts the observations, suggesting that in the San Bernardino region the overall attenuation is not as strong as the average across southern California. However, the distance dependence is similar to the observations, which is why a two-layer model is not required to explain our S/P results for this region. This is supported by the fact that no significant differences are seen in S/P amplitude ratios between shallow and deep events (see Figure S6.1, S6.2 & S6.3).

However, in the future, we hope to build on this work to explore the range of scattering and intrinsic attenuation models that can explain both S/P ratios and coda envelopes in different regions across southern California.

The dominant scattering direction is determined by the parameter ak, where a is the correlation distance, the same as equation (1), and k is the wave number. The scattering is primarily backward for $ak << 1$, and the scattering is forward for $ak >> 1$ (Sato et al., 2012, p. 146). In general, values of ak are proportional to frequency, suggesting that at low frequencies ak is reduced and scattering might tend to be backward. But, in this work, even at the lowest frequency of 1.5 Hz, we find ak is 2.8 and 4.9 for P and S waves, respectively, indicating forward scattering. The scattering attenuation for the forward scattering can be computed using $Q_{Sc} = v/\omega l_t$, where l_t is transport free mean path (Turner, 1998; Przybilla et al., 2009; Wang and Shearer, 2017). In this study, we find both the intrinsic and scattering attenuation of the P wave are smaller than that of the S wave (see Table 6.1). Some previous crustal studies have found that the total P attenuation is less than the S attenuation (e.g. Yoshimoto et al., 1993; Chung and Sato, 2001; Hauksson and Shearer, 2006; Lin and Jordan, 2018), while the Takemura et al. (2017) analysis of scattering in the Chugoku region of Japan suggested that intrinsic attenuation dominates over scattering attenuation and that the intrinsic P attenuation is greater than the intrinsic S attenuation. Proposed explanations for stronger P-wave attenuation than S-wave attenuation include scattering (Yoshimoto et al., 1993; Lin and Jordan, 2018) and partial fluid saturation of crustal rock, which cause increasing internal dissipation in compression (Ponko and Sanders, 1994; Hauksson and Shearer, 2006).

Acknowledgments

We would like to thank the personnel of the USGS/Caltech Southern California Seismic Network who pick and archive the seismograms and the Southern California Earthquake

Center (SCEC) for distributing the data. This research was funded by NEHRP/USGS grant G18AP00024 and by SCEC grants 17041 and 18086. SCEC is funded by NSF Cooperative Agreement EAR-1033462 and USGS Cooperative Agreement G12AC20038. The refined catalog is available at http://scedc.caltech.edu/research-tools/downloads.html. The picked arrival times and seismograms were downloaded by using the Seismogram Transfer Program (STP), which is available at http://scedc.caltech.edu/research-tools/stp-index.html.

Chapter 6, in full, is currently under revision for publication as Wang W.,Buehler J., Shearer P., Kilb D., and Vernon F., “Focal mechanism effects on S/P amplitude ratio in San Bernardino region, southern California”. The dissertation author was the primary investigator and author of the paper.

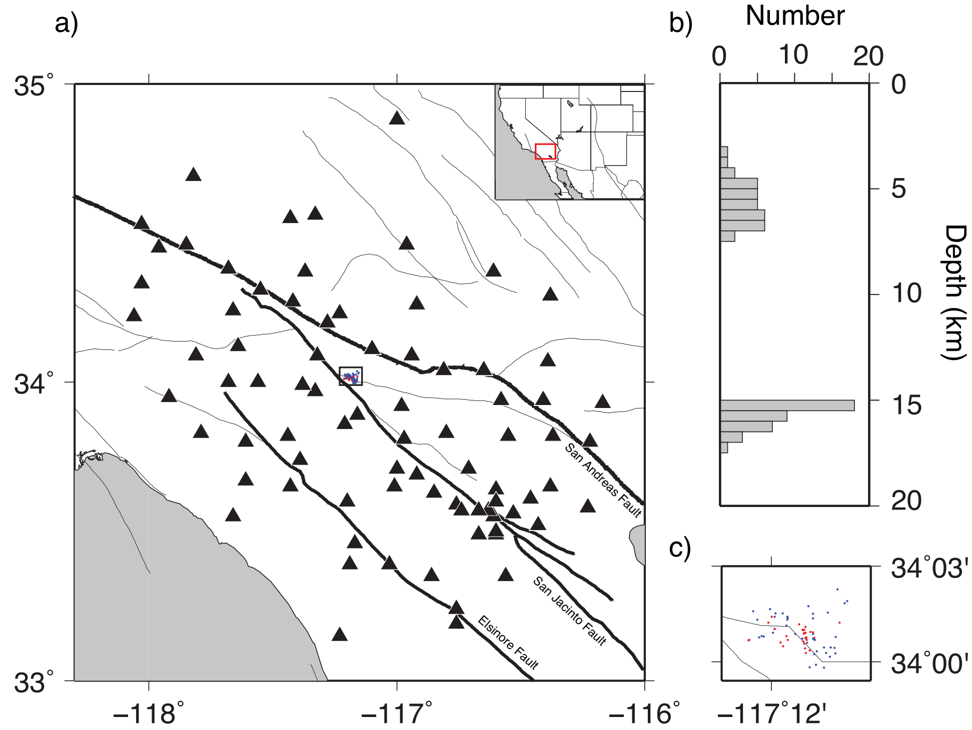

Figure 6.1: Locations and depths of earthquakes (33 shallow and 40 deep earthquakes) and 80 stations used in this study in San Bernardino region, southern California. (a) Stations are plotted as black triangles and earthquake epicenters are within the small rectangular box. Quaternary faults are depicted as light black curves and three major faults are illustrated as bold curves and labeled with their names. The red box in the top right plot indicates our study region in the western U.S. map. (b) Histogram of event depths. (c) A closeup of the epicentral region, with shallow and deep events shown as red and blue dots, respectively.

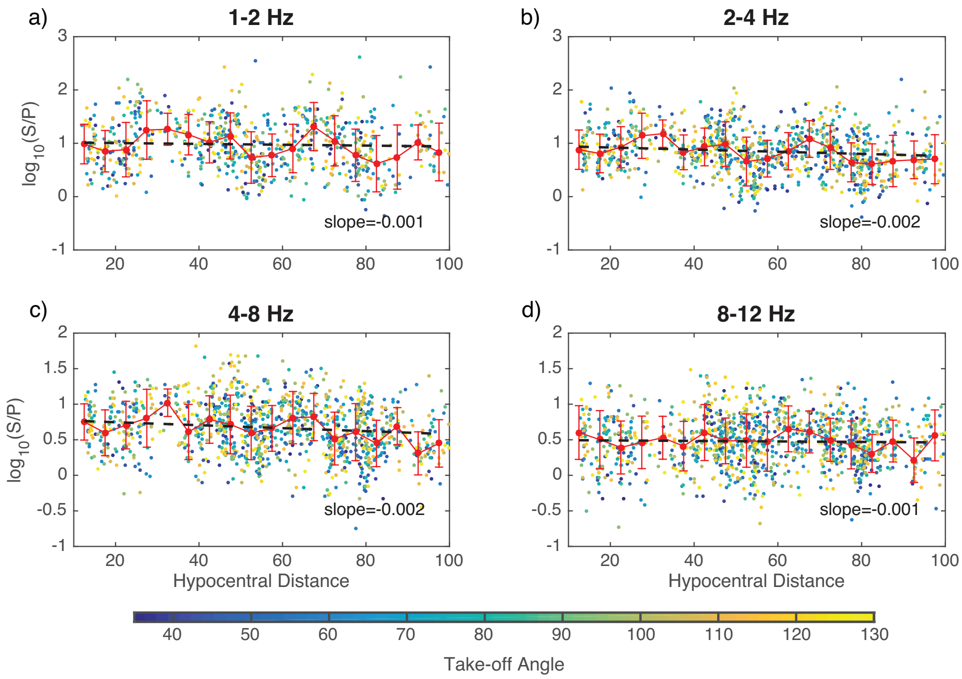

Figure 6.2: Observed peak absolute S/P amplitude ratios versus hypocentral distances at frequency 1–2, 2–4, 4–8, and 8–12 Hz, respectively. Black dashed line indicates the best linear fit of the data, where the slope is listed in each figure. We plot the median S/P amplitude ratios within the 5 km bins with one standard deviation error bars. The color bar shows the takeoff angle for each recording.

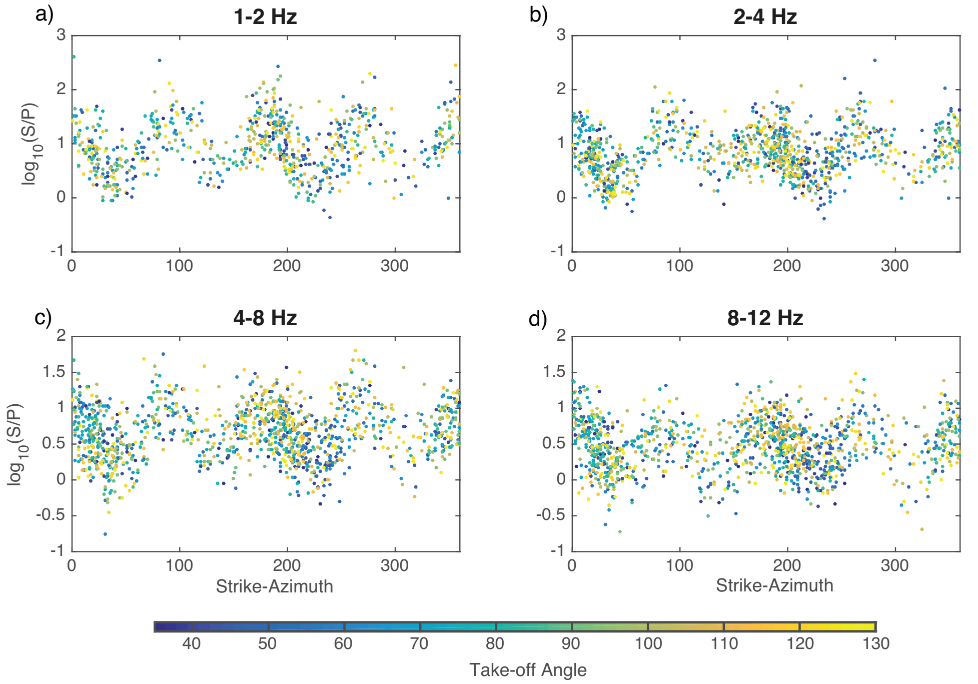

Figure 6.3: Observed peak absolute S/P amplitude ratios versus differences between strikes and azimuths at 1–2, 2–4, 4–8, and 8–12 Hz, respectively. The color bar shows the epicentral distance for each recording.

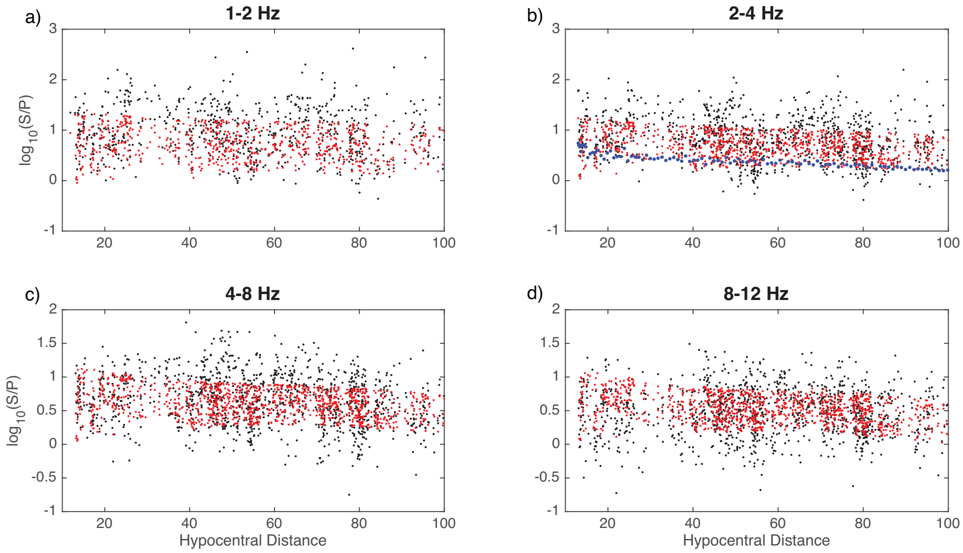

Figure 6.4: A synthetic example showing how the phase-bin declustering method works. (a) Event time versus phase for a given period. Red dots represent individual event location in time versus phase. Vertical dashed lines separate each cycle into eight equal increments. The sloping lines show increasing phase with respect to time in each cycle. Note that events within a tight temporal cluster (e.g., a swarm or aftershock sequence) will tend to occur at the same phase, possibly biasing tests of phase randomness. (b) The phase-bin declustered catalog, in which only the maximum magnitude event is retained for each phase bin at each cycle.

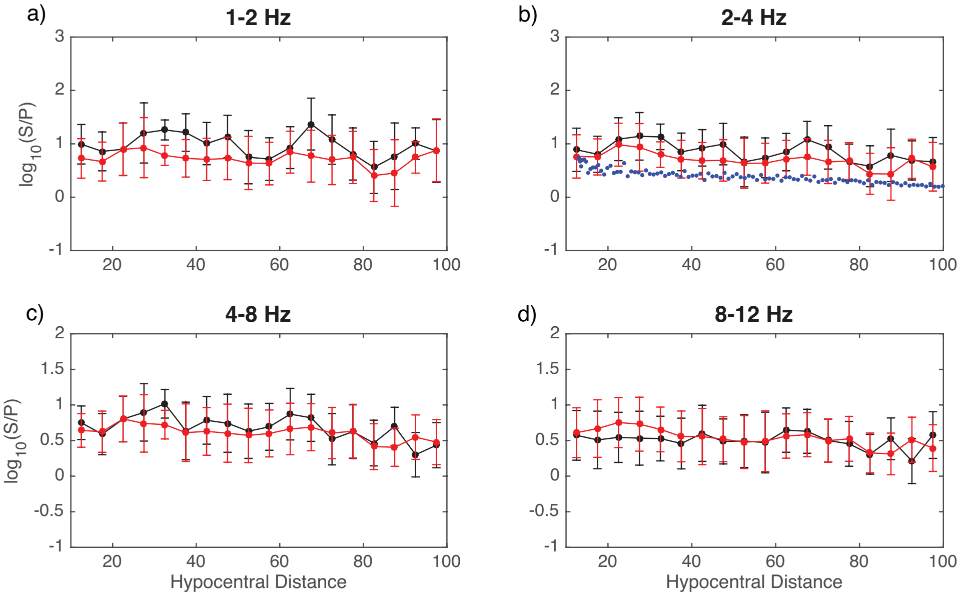

Figure 6.5: Comparison of the observed (black dots) and synthetic (red dots) peak absolute S/P amplitude ratios versus hypocentral distance, using the best-fitting intrinsic ($Q_P = 250, Q_S = 312$ at 1.5 Hz and $\eta = 0.2$) and Von Karman scattering model ($a = 2$ km, and $\kappa = 0.3$) at 1–2, 2–4, 4–8, and 8–12 Hz, respectively. The synthetic S/P amplitude ratios from the two-layer model in Wang and Shearer (2017) are shown in (b) as blue dots.

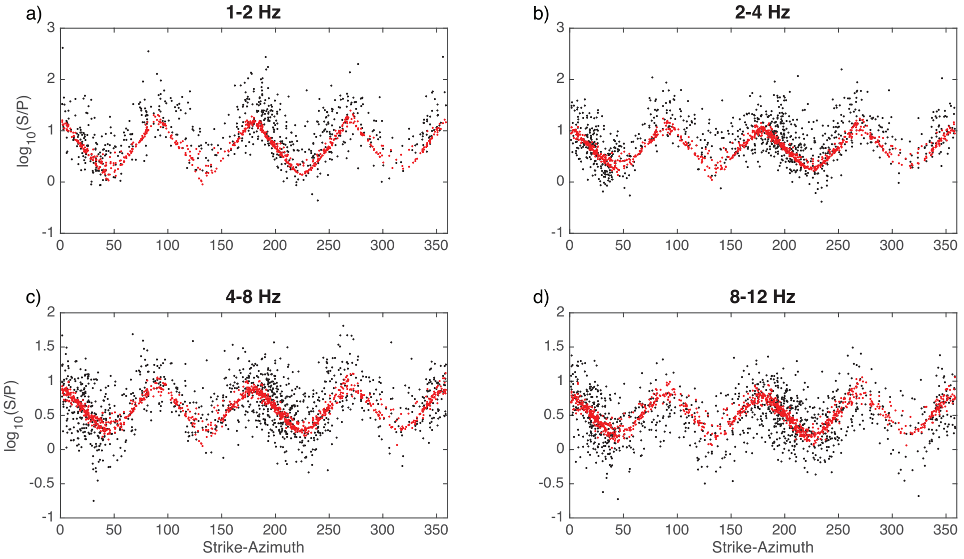

Figure 6.6: Comparison of the observed (black dots) and synthetic (red dots) peak absolute S/P amplitude ratios versus difference between strike and azimuth, using the best-fitting model as in Figure 4.

Table 6.1: Model parameters, including correlation length (*a*), rms perturbation (ε), intrinsic Q ($^{\alpha}Q_I$ and $^{\beta}Q_I$ for P and S waves, respectively), scattering Q ($^{\alpha}Q_{Sc}$ and $^{\beta}Q_{Sc}$), and total Q ($^{\alpha}Q_T$ and $^{\beta}Q_T$) for different frequencies.

Frequency	$^{\alpha}Q_I$	$^{\alpha}Q_{Sc}$	$^{\alpha}Q_T$	$^{\beta}Q_I$	$^{\beta}Q_{Sc}$	$^{\beta}Q_T$
1.5 Hz	250	470	163	312	759	221
3 Hz	287	569	190	358	931	258
6 Hz	330	732	227	412	1203	306
10 Hz	365	908	266	456	1502	350

6.6 Supplementary Materials

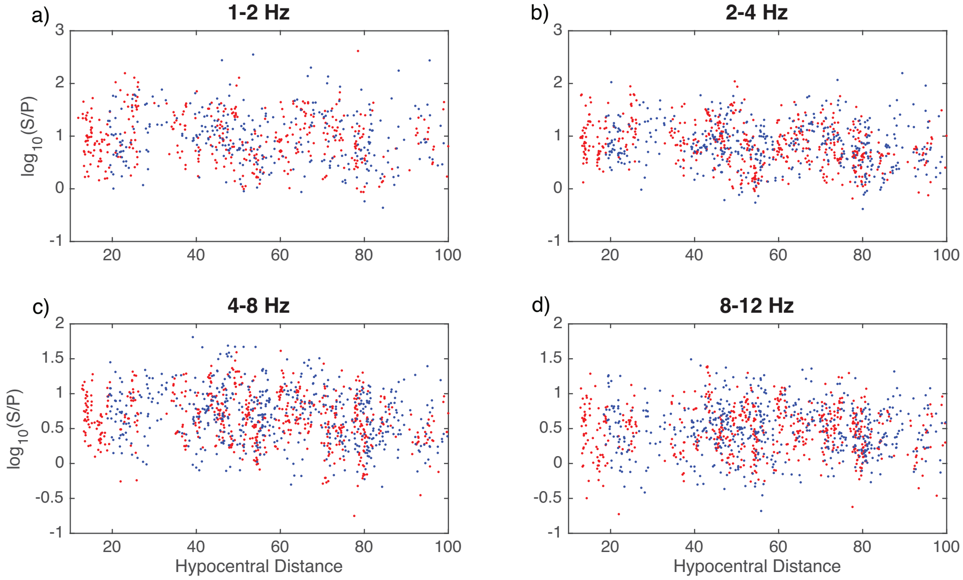

Figure S6.1: Observed peak absolute S/P amplitude ratios of shallow (red dots) and deep (blue dots) earthquakes versus hypocentral distances at frequency bands 1–2, 2–4, 4–8, and 8–12 Hz, respectively.

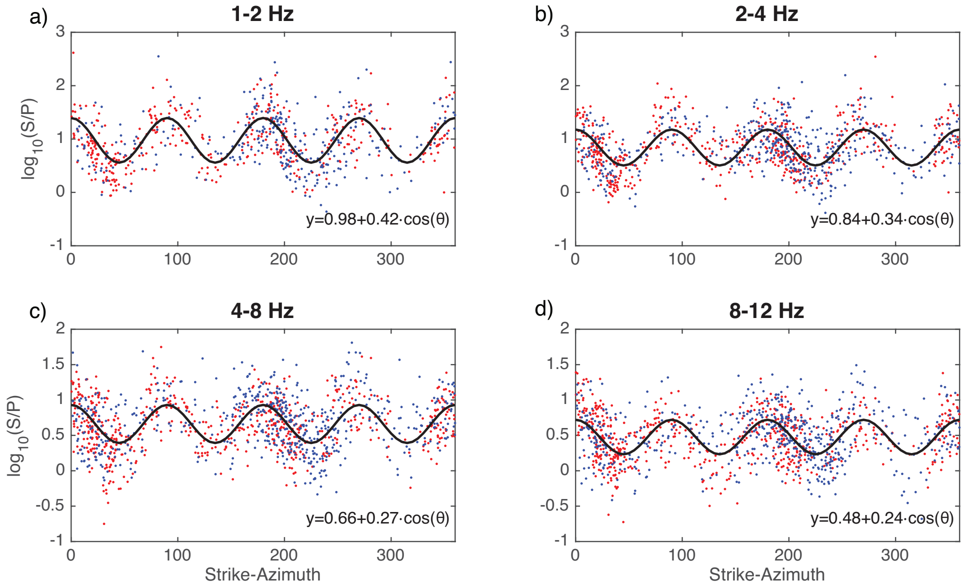

Figure S6.2: Observed peak absolute S/P amplitude ratios of shallow (red dots) and deep (blue dots) earthquakes versus difference between strikes and azimuths (DSA) at frequency bands 1–2, 2–4, 4–8, and 8–12 Hz, respectively. The black line is the best fitting sine function to the S/P amplitude ratios at each frequency range.

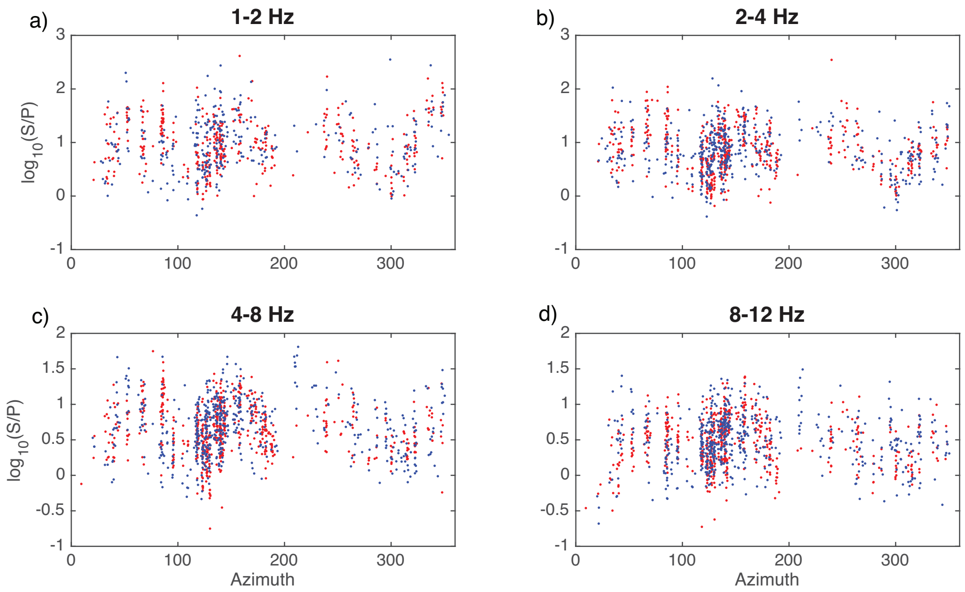

Figure S6.3: Observed peak absolute S/P amplitude ratios of shallow (red dots) and deep (blue dots) earthquakes versus azimuths at frequency bands 1–2, 2–4, 4–8, and 8–12 Hz, respectively.

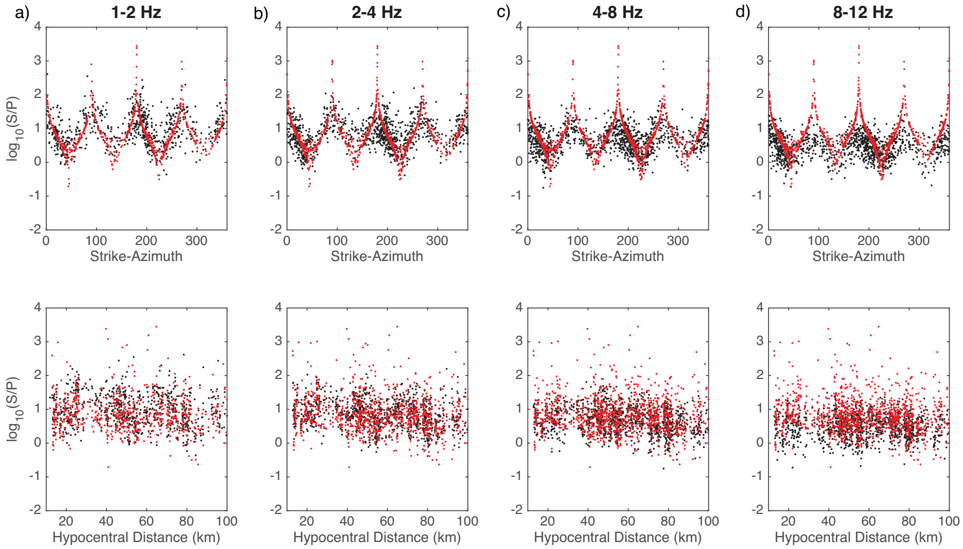

Figure S6.4: Comparison of observed (black dots) and synthetic (red dots) peak absolute S/P amplitude ratios at frequency bands 1–2, 2–4, 4–8, and 8–12 Hz, respectively. The synthetics are computed from the non-attenuated model.

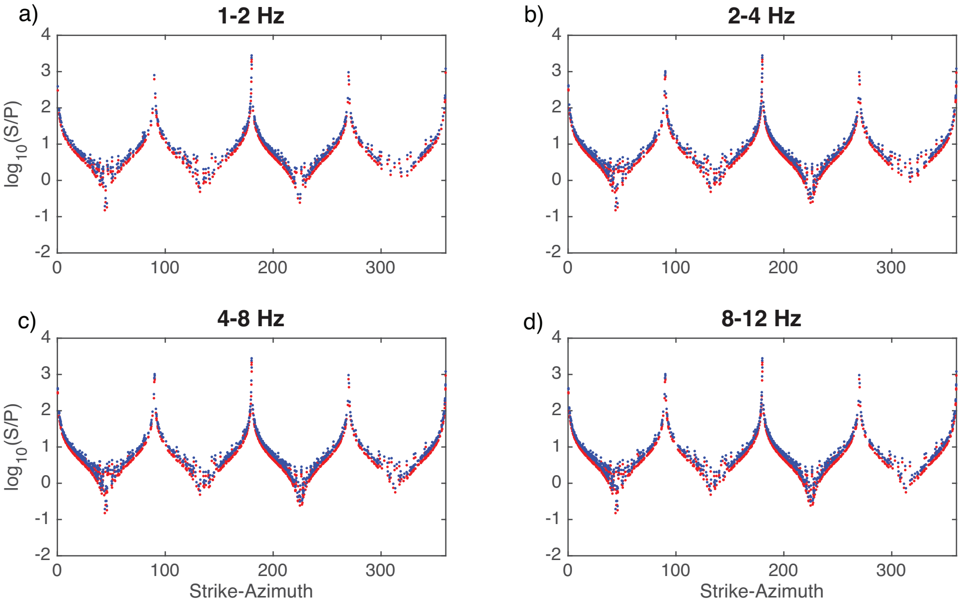

Figure S6.5: Comparison of synthetic synthetic peak absolute S/P amplitude ratios from the non-attenuated model using the source radiated S-wave energy to P-wave energy ratio 14 (red dots) and 23.4 (blue dots) at frequency bands 1–2, 2–4, 4–8, and 8–12 Hz, respectively.

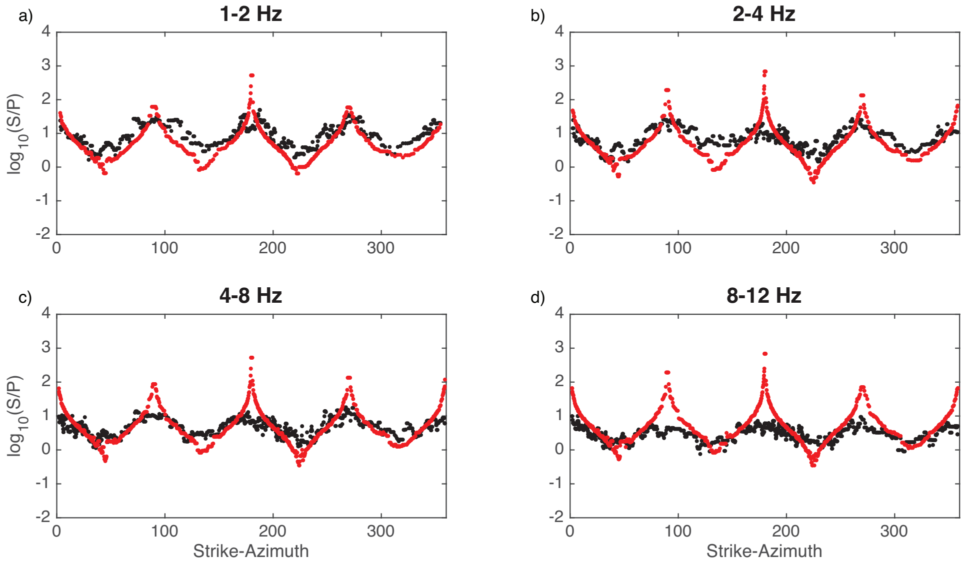

Figure S6.6: Comparison of the ‘stacked’ observed (black dots) and synthetic (red dots) peak absolute S/P amplitude ratios versus DSAs, using the non-attenuated model by applying the same moving median approach as in Figure S4, at frequency bands 1–2, 2–4, 4–8, and 8–12 Hz, respectively.

Bibliography

Abercrombie, R. E., 1995: Earthquake source scaling relationships from- 1 to 5 ml using seismograms recorded at 2.5-km depth. *Journal of Geophysical Research: Solid Earth*, **100 (B12)**, 24 015–24 036.

Abercrombie, R. E., 1996: The magnitude-frequency distribution of earthquakes recorded with deep seismometers at cajon pass, southern california. *Tectonophysics*, **261 (1-3)**, 1–7.

Agnew, D. C., 1997: Nloadf: A program for computing ocean-tide loading. *Journal of Geophysical Research: Solid Earth*, **102 (B3)**, 5109–5110.

Agnew, D. C., 2012: Spotl: Some programs for ocean-tide loading.

Aiken, C., and Z. Peng, 2014: Dynamic triggering of microearthquakes in three geothermal/volcanic regions of california. *Journal of Geophysical Research: Solid Earth*, **119 (9)**, 6992–7009.

Aki, K., 1969: Analysis of the seismic coda of local earthquakes as scattered waves. *Journal of Geophysical Research*, **74 (2)**, 615–631.

Aki, K., 1980: Scattering and attenuation of shear waves in the lithosphere. *Journal of Geophysical Research: Solid Earth*, **85 (B11)**, 6496–6504.

Aki, K., 1996: Scale dependence in earthquake phenomena and its relevance to earthquake prediction. *Proceedings of the National Academy of Sciences*, **93 (9)**, 3740–3747.

Aki, K., and B. Chouet, 1975: Origin of coda waves: source, attenuation, and scattering effects. *Journal of Geophysical Research*, **80 (23)**, 3322–3342.

Aki, K., and P. Richards, 1980: Quantitive seismology: Theory and methods. la. ed. *San Francisco (EEUU): Freeman and Company*, **1**, 557.

Aki, K., and P. G. Richards, 2002: *Quantitative seismology*.

Anderson, J. G., and S. E. Hough, 1984: A model for the shape of the fourier amplitude spectrum of acceleration at high frequencies. *Bulletin of the Seismological Society of America*, **74 (5)**, 1969–1993.

Archuleta, R. J., E. Cranswick, C. Mueller, and P. Spudich, 1982: Source parameters of the 1980 mammoth lakes, california, earthquake sequence. *Journal of Geophysical Research: Solid Earth*, **87 (B6)**, 4595–4607.

Aster, R. C., G. Slad, J. Henton, and M. Antolik, 1996: Differential analysis of coda q using similar microearthquakes in seismic gaps. part 1: Techniques and application to seismograms recorded in the anza seismic gap. *Bulletin of the Seismological Society of America*, **86 (3)**, 868–889.

Bakun, W. H., 1984: Seismic moments, local magnitudes, and coda-duration magnitudes for earthquakes in central california. *Bulletin of the Seismological Society of America*, **74 (2)**, 439–458.

Baltay, A., G. Prieto, and G. C. Beroza, 2010: Radiated seismic energy from coda measurements and no scaling in apparent stress with seismic moment. *Journal of Geophysical Research: Solid Earth*, **115 (B8)**.

Baltay, A. S., and G. C. Beroza, 2013: Ground-motion prediction from tremor. *Geophysical Research Letters*, **40 (24)**, 6340–6345.

Beeler, N., and D. Lockner, 2003: Why earthquakes correlate weakly with the solid earth tides: Effects of periodic stress on the rate and probability of earthquake occurrence. *Journal of Geophysical Research: Solid Earth*, **108 (B8)**.

Ben-Zion, Y., and L. Zhu, 2002: Potency-magnitude scaling relations for southern california earthquakes with 1.0¡ m_l¡ 7.0. *Geophysical Journal International*, **148 (3)**, F1–F5.

Beroza, G. C., A. T. Cole, and W. L. Ellsworth, 1995: Stability of coda wave attenuation during the loma prieta, california, earthquake sequence. *Journal of Geophysical Research: Solid Earth*, **100 (B3)**, 3977–3987.

Bianco, F., E. Del Pezzo, M. Castellano, J. Ibanez, and F. Di Luccio, 2002: Separation of intrinsic and scattering seismic attenuation in the southern apennine zone, italy. *Geophysical Journal International*, **150 (1)**, 10–22.

Boatwright, J., and J. B. Fletcher, 1984: The partition of radiated energy between p and s waves. *Bulletin of the Seismological Society of America*, **74 (2)**, 361–376.

Boatwright, J., J. B. Fletcher, and T. E. Fumal, 1991: A general inversion scheme for source, site, and propagation characteristics using multiply recorded sets of moderate-sized earthquakes. *Bulletin of the Seismological Society of America*, **81 (5)**, 1754–1782.

Boore, D. M., and W. B. Joyner, 1982: The empirical prediction of ground motion. *Bulletin of the Seismological Society of America*, **72 (6B)**, S43–S60.

Bostock, M. G., A. M. Thomas, G. Savard, L. Chuang, and A. M. Rubin, 2015: Magnitudes and moment-duration scaling of low-frequency earthquakes beneath southern vancouver island. *Journal of Geophysical Research: Solid Earth*, **120 (9)**, 6329–6350.

Brinkman, B. A., M. LeBlanc, Y. Ben-Zion, J. T. Uhl, and K. A. Dahmen, 2015: Probing failure susceptibilities of earthquake faults using small-quake tidal correlations. *Nature Communications*, **6**, 6157.

Brodsky, E. E., and S. G. Prejean, 2005: New constraints on mechanisms of remotely triggered seismicity at long valley caldera. *Journal of Geophysical Research: Solid Earth*, **110 (B4)**.

Brune, J. N., 1970: Tectonic stress and the spectra of seismic shear waves from earthquakes. *Journal of Geophysical Research*, **75 (26)**, 4997–5009.

Bydlon, S. A., and E. M. Dunham, 2015: Rupture dynamics and ground motions from earthquakes in 2-d heterogeneous media. *Geophysical Research Letters*, **42 (6)**, 1701–1709.

Caltech, and USGS, 1926: Southern california seismic network. international federation of digital seismograph networks. *Dataset/Seismic Network*, **10.7914/SN/CI**.

Calvet, M., and L. Margerin, 2013: Lapse-time dependence of coda q: Anisotropic multiple-scattering models and application to the pyrenees. *Bulletin of the Seismological Society of America*, **103 (3)**, 1993–2010.

Carcolé, E., and H. Sato, 2010: Spatial distribution of scattering loss and intrinsic absorption of short-period s waves in the lithosphere of japan on the basis of the multiple lapse time window analysis of hi-net data. *Geophysical Journal International*, **180 (1)**, 268–290.

Chandler, A., N. Lam, and H. Tsang, 2006: Near-surface attenuation modelling based on rock shear-wave velocity profile. *Soil Dynamics and Earthquake Engineering*, **26 (11)**, 1004–1014.

Chu, R., S. Wei, D. V. Helmberger, Z. Zhan, L. Zhu, and H. Kanamori, 2011: Initiation of the great mw 9.0 tohoku–oki earthquake. *Earth and Planetary Science Letters*, **308 (3)**, 277–283.

Chung, T.-W., and H. Sato, 2001: Attenuation of high-frequency p and s waves in the crust of southeastern south korea. *Bulletin of the Seismological Society of America*, **91 (6)**, 1867–1874.

Cochran, E. S., J. E. Vidale, and S. Tanaka, 2004: Earth tides can trigger shallow thrust fault earthquakes. *Science*, **306 (5699)**, 1164–1166.

Delorey, A. A., N. J. van der Elst, and P. A. Johnson, 2017: Tidal triggering of earthquakes suggests poroelastic behavior on the san andreas fault. *Earth and Planetary Science Letters*, **460**, 164–170.

Denieul, M., O. Sèbe, M. Cara, and Y. Cansi, 2015: M w estimation from crustal coda waves recorded on analog seismograms. *Bulletin of the Seismological Society of America*, **105 (2A)**, 831–849.

Dewberry, S. R., and R. S. Crosson, 1995: Source scaling and moment estimation for the pacific northwest seismograph network using s-coda amplitudes. *Bulletin of the Seismological Society of America*, **85 (5)**, 1309–1326.

Dziewonski, A., T.-A. Chou, and J. Woodhouse, 1981: Determination of earthquake source parameters from waveform data for studies of global and regional seismicity. *Journal of Geophysical Research: Solid Earth*, **86 (B4)**, 2825–2852.

Eaton, J. P., 1992: Determination of amplitude and duration magnitudes and site residuals from short-period seismographs in northern california. *Bulletin of the Seismological Society of America*, **82 (2)**, 533–579.

Ebel, J., and K.-P. Bonjer, 1990: Moment tensor inversion of small earthquakes in southwestern germany for the fault plane solution. *Geophysical Journal International*, **101 (1)**, 133–146.

Efron, B., and R. J. Tibshirani, 1994: *An introduction to the bootstrap*. CRC press.

Ekström, G., M. Nettles, and A. Dziewoński, 2012: The global cmt project 2004–2010: Centroid-moment tensors for 13,017 earthquakes. *Physics of the Earth and Planetary Interiors*, **200**, 1–9.

Eulenfeld, T., and U. Wegler, 2016: Measurement of intrinsic and scattering attenuation of shear waves in two sedimentary basins and comparison to crystalline sites in germany. *Geophysical Journal International*, **205 (2)**, 744–757.

Eulenfeld, T., and U. Wegler, 2017: Crustal intrinsic and scattering attenuation of high-frequency shear waves in the contiguous united states. *Journal of Geophysical Research: Solid Earth*, **122 (6)**, 4676–4690.

Fehler, M., M. Hoshiba, H. Sato, and K. Obara, 1992: Separation of scattering and intrinsic attenuation for the kanto-tokai region, japan, using measurements of s-wave energy versus hypocentral distance. *Geophysical Journal International*, **108 (3)**, 787–800.

Fialko, Y., and M. Simons, 2000: Deformation and seismicity in the coso geothermal area, inyo county, california: Observations and modeling using satellite radar interferometry. *Journal of Geophysical Research: Solid Earth*, **105 (B9)**, 21 781–21 793.

Frankel, A., and R. W. Clayton, 1986: Finite difference simulations of seismic scattering: Implications for the propagation of short-period seismic waves in the crust and models of crustal heterogeneity. *Journal of Geophysical Research: Solid Earth*, **91 (B6)**, 6465–6489.

Frankel, A., A. McGarr, J. Bicknell, J. Mori, L. Seeber, and E. Cranswick, 1990: Attenuation of high-frequency shear waves in the crust: Measurements from new york state, south africa, and southern california. *Journal of Geophysical Research: Solid Earth*, **95 (B11)**, 17 441–17 457.

Frankel, A., and L. Wennerberg, 1987: Energy-flux model of seismic coda: Separation of scattering and intrinsic attenuation. *Bulletin of the Seismological Society of America*, **77 (4)**, 1223–1251.

Gomberg, J., M. L. Blanpied, and N. Beeler, 1997: Transient triggering of near and distant earthquakes. *Bulletin of the Seismological Society of America*, **87 (2)**, 294–309.

Gomberg, J., and S. Davis, 1996: Stress/strain changes and triggered seismicity at the geysers, california. *Journal of Geophysical Research: Solid Earth*, **101 (B1)**, 733–749.

Gusev, A., and I. Abubakirov, 1987: Monte-carlo simulation of record envelope of a near earthquake. *Physics of the Earth and Planetary Interiors*, **49 (1)**, 30–36.

Hadley, D., and H. Kanamori, 1977: Seismic structure of the transverse ranges, california. *Geological Society of America Bulletin*, **88 (10)**, 1469–1478.

Hardebeck, J. L., 2006: Homogeneity of small-scale earthquake faulting, stress, and fault strength. *Bulletin of the Seismological Society of America*, **96 (5)**, 1675–1688.

Hardebeck, J. L., and P. M. Shearer, 2002: A new method for determining first-motion focal mechanisms. *Bulletin of the Seismological Society of America*, **92 (6)**, 2264–2276.

Hardebeck, J. L., and P. M. Shearer, 2003: Using s/p amplitude ratios to constrain the focal mechanisms of small earthquakes. *Bulletin of the Seismological Society of America*, **93 (6)**, 2434–2444.

Harrington, R. M., and E. E. Brodsky, 2006: The absence of remotely triggered seismicity in japan. *Bulletin of the Seismological Society of America*, **96 (3)**, 871–878.

Hartzell, S., and T. Heaton, 1989: The fortnightly tide and the tidal triggering of earthquakes. *Bulletin of the Seismological Society of America*, **79 (4)**, 1282–1286.

Hauksson, E., and P. M. Shearer, 2006: Attenuation models (q_p and q_s) in three dimensions of the southern california crust: Inferred fluid saturation at seismogenic depths. *Journal of Geophysical Research: Solid Earth*, **111 (B5)**.

Hauksson, E., W. Yang, and P. M. Shearer, 2012: Waveform relocated earthquake catalog for southern california (1981 to june 2011). *Bulletin of the Seismological Society of America*, **102 (5)**, 2239–2244.

Hawthorne, J. C., J.-P. Ampuero, and M. Simons, 2017: A method for calibration of the local magnitude scale based on relative spectral amplitudes, and application to the san juan bautista, california, area. *Bulletin of the Seismological Society of America*, **107 (1)**, 85–96.

Heaton, T. H., 1982: Tidal triggering of earthquakes. *Bulletin of the Seismological Society of America*, **72 (6A)**, 2181–2200.

Hedlin, M. A., P. M. Shearer, P. S. Earle, and Coauthors, 1997: Seismic evidence for small-scale heterogeneity throughout the earth's mantle. *Nature*, **387 (6629)**, 145–150.

Hellweg, M., P. Spudich, J. Fletcher, and L. Baker, 1995: Stability of coda q in the region of parkfield, california: View from the us geological survey parkfield dense seismograph array. *Journal of Geophysical Research: Solid Earth*, **100 (B2)**, 2089–2102.

Herrmann, R. B., 1975: The use of duration as a measure of seismic moment and magnitude. *Bulletin of the Seismological Society of America*, **65 (4)**, 899–913.

Hill, D., and S. Prejean, 2007: Dynamic triggering in treatise of geophysics, vol. 4. *ed. Kanamori, H., Elsevier Science*, 257–291.

Hill, D. P., J. O. Langbein, and S. Prejean, 2003: Relations between seismicity and deformation during unrest in long valley caldera, california, from 1995 through 1999. *Journal of Volcanology and Geothermal Research*, **127 (3-4)**, 175–193.

Hill, D. P., and Coauthors, 1993: Seismicity remotely triggered by the magnitude 7.3 landers, california, earthquake. *Science*, **260 (5114)**, 1617–1623.

Hiramatsu, Y., N. Hayashi, and M. Furumoto, 2000: Temporal changes in coda q^{-1} and b value due to the static stress change associated with the 1995 hyogo-ken nanbu earthquake. *Journal of Geophysical Research: Solid Earth*, **105 (3)**, 6141–6151.

Hoshiba, M., 1991: Simulation of multiple-scattered coda wave excitation based on the energy conservation law. *Physics of the Earth and Planetary Interiors*, **67 (1)**, 123–136.

Hoshiba, M., 1993: Separation of scattering attenuation and intrinsic absorption in japan using the multiple lapse time window analysis of full seismogram envelope. *Journal of Geophysical Research: Solid Earth*, **98 (B9)**, 15 809–15 824.

Hoshiba, M., 1994: Simulation of coda wave envelope in depth dependent scattering and absorption structure. *Geophysical Research Letters*, **21 (25)**, 2853–2856.

Hoshiba, M., 1997: Seismic coda wave envelope in depth-dependent s wave velocity structure. *Physics of the Earth and Planetary Interiors*, **104 (1)**, 15–22.

Houng, S. E., 2017: Discrimination between natural earthquakes and explosions based on the azimuthal distribution of s/p amplitude ratios. *Bulletin of the Seismological Society of America*, **108 (1)**, 218–229.

Houng, S. E., and T.-K. Hong, 2013: Probabilistic analysis of the korean historical earthquake records. *Bulletin of the Seismological Society of America*, **103 (5)**, 2782–2796.

Huang, Z.-X., and C. Kisslinger, 1992: Coda-q before and after the 1986 andreanof islands earthquake. *Pure and Applied Geophysics*, **138 (1)**, 1–16.

Huang, Z.-X., and M. Wyss, 1988: Coda q before the 1983 hawaii (m_s = 6.6) earthquake. *Bulletin of the Seismological Society of America*, **78 (3)**, 1279–1296.

Hutton, K., J. Woessner, and E. Hauksson, 2010: Earthquake monitoring in southern california for seventy-seven years (1932–2008). *Bulletin of the Seismological Society of America*, **100 (2)**, 423–446.

Ibanez, J., E. Del Pezzo, F. De Miguel, M. Herraiz, G. Alguacil, and J. Morales, 1990: Depth-dependent seismic attenuation in the granada zone (southern spain). *Bulletin of the Seismological Society of America*, **80 (5)**, 1232–1244.

Ide, S., S. Yabe, and Y. Tanaka, 2016: Earthquake potential revealed by tidal influence on earthquake size–frequency statistics. *Nature Geoscience*, **9 (11)**, 834.

Jin, A., and K. Aki, 1988: Spatial and temporal correlation between coda *q* and seismicity in china. *Bulletin of the Seismological Society of America*, **78 (2)**, 741–769.

Jin, A., and K. Aki, 2005: High-resolution maps of coda *q* in japan and their interpretation by the brittle-ductile interaction hypothesis. *Earth, Planets and Space*, **57 (5)**, 403–409.

Jin, A., K. Mayeda, D. Adams, and K. Aki, 1994: Separation of intrinsic and scattering attenuation in southern california using terrascope data. *Journal of Geophysical Research: Solid Earth*, **99 (B9)**, 17 835–17 848.

Johnson, C. E., 1979: I. cedar–an approach to the computer automation of short-period local seismic networks. ii. seismotectonics of the imperial valley of southern california. Ph.D. thesis, California Institute of Technology.

Julian, B. R., and G. Foulger, 1996: Earthquake mechanisms from linear-programming inversion of seismic-wave amplitude ratios. *Bulletin of the Seismological Society of America*, **86 (4)**, 972–980.

Kanamori, H., 1977: The energy release in great earthquakes. *Journal of Geophysical Research*, **82 (20)**, 2981–2987.

Kato, A., K. Obara, T. Igarashi, H. Tsuruoka, S. Nakagawa, and N. Hirata, 2012: Propagation of slow slip leading up to the 2011 mw 9.0 tohoku-oki earthquake. *Science*, **335 (6069)**, 705–708.

Kato, K., K. Aki, and M. Takemura, 1995: Site amplification from coda waves: validation and application to s-wave site response. *Bulletin of the Seismological Society of America*, **85 (2)**, 467–477.

Kilb, D., J. Gomberg, and P. Bodin, 2000: Triggering of earthquake aftershocks by dynamic stresses. *Nature*, **408 (6812)**, 570.

Kilb, D., J. Gomberg, and P. Bodin, 2002: Aftershock triggering by complete coulomb stress changes. *Journal of Geophysical Research: Solid Earth*, **107 (B4)**, ESE–2.

Kim, W.-Y., V. Aharonian, A. Lerner-Lam, and P. Richards, 1997: Discrimination of earthquakes and explosions in southern russia using regional high-frequency three-component data from the iris/jsp caucasus network. *Bulletin of the Seismological Society of America*, **87 (3)**, 569–588.

King, G. C., R. S. Stein, and J. Lin, 1994: Static stress changes and the triggering of earthquakes. *Bulletin of the Seismological Society of America*, **84 (3)**, 935–953.

Kisslinger, C., 1980: Evaluation of s to p amplitude rations for determining focal mechanisms from regional network observations. *Bulletin of the Seismological Society of America*, **70 (4)**, 999–1014.

Kisslinger, C., J. R. Bowman, and K. Koch, 1981: Procedures for computing focal mechanisms from local (sv/p) z data. *Bulletin of the Seismological Society of America*, **71 (6)**, 1719–1729.

Knopoff, L., 1971: Attenuation, in *Mantle and Core in Plantery Physics*. Elsevier, New York, 146–156 pp.

Koyanagi, S., K. Mayeda, and K. Aki, 1992: Frequency-dependent site amplification factors using the s-wave coda for the island of hawaii. *Bulletin of the Seismological Society of America*, **82 (3)**, 1151–1185.

Lay, T., and T. C. Wallace, 1995: *Modern global seismology*, Vol. 58. Elsevier.

Lee, W. H. K., R. Bennett, and K. Meagher, 1972: *A method of estimating magnitude of local earthquakes from signal duration*. US Department of the Interior, Geological Survey.

Lee, W. S., S. Yun, and J.-Y. Do, 2010: Scattering and intrinsic attenuation of short-period s waves in the gyeongsang basin, south korea, revealed from s-wave seismogram envelopes based on the radiative transfer theory. *Bulletin of the Seismological Society of America*, **100 (2)**, 833–840.

Lin, Y.-P., and T. H. Jordan, 2018: Frequency-dependent attenuation of p and s waves in southern california. *Journal of Geophysical Research: Solid Earth*.

Liu, H.-L., and D. V. Helmberger, 1985: The 23: 19 aftershock of the 15 october 1979 imperial valley earthquake: more evidence for an asperity. *Bulletin of the Seismological Society of America*, **75 (3)**, 689–708.

Madariaga, R., 1976: Dynamics of an expanding circular fault. *Bulletin of the Seismological Society of America*, **66 (3)**, 639–666.

Madariaga, R., 2007: Seismic source theory-4.02.

Mancinelli, N., P. Shearer, and Q. Liu, 2016: Constraints on the heterogeneity spectrum of earth's upper mantle. *Journal of Geophysical Research: Solid Earth*.

Mancinelli, N. J., and P. M. Shearer, 2013: Reconciling discrepancies among estimates of small-scale mantle heterogeneity from pkp precursors. *Geophysical Journal International*, **195 (3)**, 1721–1729.

Margerin, L., M. Campillo, N. Shapiro, and B. van Tiggelen, 1999: Residence time of diffuse waves in the crust as a physical interpretation of coda *q*: application to seismograms recorded in mexico. *Geophysical Journal International*, **138 (2)**, 343–352.

Margerin, L., M. Campillo, and B. Tiggelen, 1998: Radiative transfer and diffusion of waves in a layered medium: new insight into coda q. *Geophysical Journal International*, **134 (2)**, 596–612.

Margerin, L., and B. Michel Capillo Van Tiggelen, 2000: Monte carlo simulation of multiple scattering. *Journal of Geophysical Research*, **105 (B4)**, 7873–7892.

Margerin, L., and G. Nolet, 2003a: Multiple scattering of high-frequency seismic waves in the deep earth: Modeling and numerical examples. *Journal of Geophysical Research: Solid Earth*, **108 (B5)**.

Margerin, L., and G. Nolet, 2003b: Multiple scattering of high-frequency seismic waves in the deep earth: Pkp precursor analysis and inversion for mantle granularity. *Journal of Geophysical Research: Solid Earth*, **108 (B11)**.

Martínez-Garzón, P., M. Bohnhoff, G. Kwiatek, and G. Dresen, 2013: Stress tensor changes related to fluid injection at the geysers geothermal field, california. *Geophysical Research Letters*, **40 (11)**, 2596–2601.

Matthews, M. V., and P. A. Reasenberg, 1988: Statistical methods for investigating quiescence and other temporal seismicity patterns. *Pure and Applied Geophysics*, **126 (2-4)**, 357–372.

Mayeda, K., A. Hofstetter, J. L. O'Boyle, and W. R. Walter, 2003: Stable and transportable regional magnitudes based on coda-derived moment-rate spectra. *Bulletin of the Seismological Society of America*, **93 (1)**, 224–239.

Mayeda, K., S. Koyanagi, and K. Aki, 1991: Site amplification from s-wave coda in the long valley caldera region, california. *Bulletin of the Seismological Society of America*, **81 (6)**, 2194–2213.

Mayeda, K., and W. R. Walter, 1996: Moment, energy, stress drop, and source spectra of western united states earthquakes from regional coda envelopes. *Journal of Geophysical Research: Solid Earth*, **101 (B5)**, 11 195–11 208.

Meng, X., and Z. Peng, 2014: Seismicity rate changes in the salton sea geothermal field and the san jacinto fault zone after the 2010 mw 7.2 el mayor-cucapah earthquake. *Geophysical Journal International*, **197 (3)**, 1750–1762.

Menke, W., 2012: *Geophysical data analysis: discrete inverse theory: MATLAB edition*, Vol. 45. Academic press.

Métivier, L., O. de Viron, C. P. Conrad, S. Renault, M. Diament, and G. Patau, 2009: Evidence of earthquake triggering by the solid earth tides. *Earth and Planetary Science Letters*, **278 (3)**, 370–375.

Mitchell, B. J., Y. Pan, J. Xie, and L. Cong, 1997: Lg coda q variation across eurasia and its relation to crustal evolution. *Journal of Geophysical Research: Solid Earth*, **102 (B10)**, 22 767–22 779.

Monastero, F. C., 2002: An overview of industry-military cooperation in the development of power operations at the coso geothermal field in southern california. *Geothermal Resoures Council Bulletin*, **31**, 188–195.

Mukhopadhyay, S., and C. Tyagi, 2008: Variation of intrinsic and scattering attenuation with depth in nw himalayas. *Geophysical Journal International*, **172 (3)**, 1055–1065.

Nakamura, A., S. Horiuchi, and A. Hasegawa, 1999: Joint focal mechanism determination with source-region station corrections using short-period body-wave amplitude data. *Bulletin of the Seismological Society of America*, **89 (2)**, 373–383.

Ogiso, M., 2018: A method for mapping intrinsic attenuation factors and scattering coefficients of s waves in 3-d space and its application in southwestern japan. *Geophysical Journal International*, **216 (2)**, 948–957.

Oth, A., D. Bindi, S. Parolai, and D. Di Giacomo, 2011: Spectral analysis of k-net and kik-net data in japan, part ii: On attenuation characteristics, source spectra, and site response of borehole and surface stations. *Bulletin of the Seismological Society of America*, **101 (2)**, 667–687.

Paasschens, J., 1997: Solution of the time-dependent boltzmann equation. *Physical Review E*, **56 (1)**, 1135.

Padhy, S., U. Wegler, and M. Korn, 2007: Seismogram envelope inversion using a multiple isotropic scattering model: Application to aftershocks of the 2001 bhuj earthquake. *Bulletin of the Seismological Society of America*, **97 (1B)**, 222–233.

Peng, J., and Coauthors, 1987: Temporal change in coda associated with the round valley, california, earthquake of november 23, 1984. *Journal of Geophysical Research: Solid Earth*, **92 (B5)**, 3507–3526.

Peng, Z., D. P. Hill, D. R. Shelly, and C. Aiken, 2010: Remotely triggered microearthquakes and tremor in central california following the 2010 mw 8.8 chile earthquake. *Geophysical Research Letters*, **37 (24)**.

Phillips, W. S., and K. Aki, 1986: Site amplification of coda waves from local earthquakes in central california. *Bulletin of the Seismological Society of America*, **76 (3)**, 627–648.

Ponko, S. C., and C. O. Sanders, 1994: Inversion for p and s wave attenuation structure, long valley caldera, california. *Journal of Geophysical Research: Solid Earth*, **99 (B2)**, 2619–2635.

Prejean, S., and Coauthors, 2004: Remotely triggered seismicity on the united states west coast following the mw 7.9 denali fault earthquake. *Bulletin of the Seismological Society of America*, **94 (6B)**, S348–S359.

Prieto, G. A., P. M. Shearer, F. L. Vernon, and D. Kilb, 2004: Earthquake source scaling and self-similarity estimation from stacking p and s spectra. *Journal of Geophysical Research: Solid Earth*, **109 (B8)**.

Przybilla, J., M. Korn, and U. Wegler, 2006: Radiative transfer of elastic waves versus finite difference simulations in two-dimensional random media. *Journal of Geophysical Research: Solid Earth*, **111 (B4)**.

Przybilla, J., U. Wegler, and M. Korn, 2009: Estimation of crustal scattering parameters with elastic radiative transfer theory. *Geophysical Journal International*, **178 (2)**, 1105–1111.

Pulli, J. J., 1984: Attenuation of coda waves in new england. *Bulletin of the Seismological Society of America*, **74 (4)**, 1149–1166.

Pyle, M. L., and W. R. Walter, 2019: Investigating the effectiveness of p/s amplitude ratios for local distance event discrimination. *Bulletin of the Seismological Society of America*, **109 (3)**, 1071–1081.

Raoof, M., R. Herrmann, and L. Malagnini, 1999: Attenuation and excitation of three-component ground motion in southern california. *Bulletin of the Seismological Society of America*, **89 (4)**, 888–902.

Rau, R.-J., F. T. Wu, and T.-C. Shin, 1996: Regional network focal mechanism determination using 3d velocity model and sh/p amplitude ratio. *Bulletin of the Seismological Society of America*, **86 (5)**, 1270–1283.

Rautian, T., and V. Khalturin, 1978: The use of the coda for determination of the earthquake source spectrum. *Bulletin of the Seismological Society of America*, **68 (4)**, 923–948.

Ray, R. D., 1999: A global ocean tide model from topex/poseidon altimetry: Got99. 2.

Reasenberg, P., 1985: Second-order moment of central california seismicity, 1969–1982. *Journal of Geophysical Research: Solid Earth (1978–2012)*, **90 (B7)**, 5479–5495.

Reasenberg, P., W. Ellsworth, and A. Walter, 1980: Teleseismic evidence for a low-velocity body under the coso geothermal area. *Journal of Geophysical Research: Solid Earth*, **85 (B5)**, 2471–2483.

Reasenberg, P. A., and R. W. Simpson, 1992: Response of regional seismicity to the static stress change produced by the loma prieta earthquake. *Science*, **255 (5052)**, 1687–1690.

Roecker, S., B. Tucker, J. King, and D. Hatzfeld, 1982: Estimates of q in central asia as a function of frequency and depth using the coda of locally recorded earthquakes. *Bulletin of the Seismological Society of America*, **72 (1)**, 129–149.

Rögnvaldsson, S. T., and R. Slunga, 1993: Routine fault plane solutions for local networks: a test with synthetic data. *Bulletin of the Seismological Society of America*, **83 (4)**, 1232–1247.

Ross, Z. E., Y. Ben-Zion, M. C. White, and F. L. Vernon, 2016: Analysis of earthquake body wave spectra for potency and magnitude values: Implications for magnitude scaling relations. *Geophysical Supplements to the Monthly Notices of the Royal Astronomical Society*, **207 (2)**, 1158–1164.

Ross, Z. E., D. T. Trugman, E. Hauksson, and P. M. Shearer, 2019: Searching for hidden earthquakes in southern california. *Science*, **364 (6442)**, 767–771.

Sandwell, D. T., and P. Wessel, 2016: Interpolation of 2-d vector data using constraints from elasticity. *Geophysical Research Letters*, **43 (20)**, 10–703.

Sato, H., 1982: Amplitude attenuation of impulsive waves in random media based on travel time corrected mean wave formalism. *The Journal of the Acoustical Society of America*, **71 (3)**, 559–564.

Sato, H., 2019: Power spectra of random heterogeneities in the solid earth. *Solid Earth*, **10 (1)**, 275–292.

Sato, H., and M. C. Fehler, 2016: Synthesis of wavelet envelope in 2-d random media having power-law spectra: comparison with fd simulations. *Geophysical Journal International*, **207 (1)**, 333–342.

Sato, H., M. C. Fehler, and T. Maeda, 2012: *Seismic wave propagation and scattering in the heterogeneous earth*, Vol. 496. Springer.

Savran, W., and K. Olsen, 2016: Model for small-scale crustal heterogeneity in los angeles basin based on inversion of sonic log data. *Geophysical Journal International*, **205 (2)**, 856–863.

Scholz, C. H., Y. J. Tan, and F. Albino, 2019: The mechanism of tidal triggering of earthquakes at mid-ocean ridges. *Nature Communications*, **10 (1)**, 2526.

Schuster, A., 1897: On lunar and solar periodicities of earthquakes. *Proceedings of the Royal Society of London*, **61 (369-377)**, 455–465.

Schwartz, S. Y., 1995: Source parameters of aftershocks of the 1991 costa rica and 1992 cape mendocino, california, earthquakes from inversion of local amplitude ratios and broadband waveforms. *Bulletin of the Seismological Society of America*, **85 (6)**, 1560–1575.

Sens-Schönfelder, C., and U. Wegler, 2006: Radiative transfer theory for estimation of the seismic moment. *Geophysical Journal International*, **167 (3)**, 1363–1372.

Shapiro, N., M. Campillo, L. Margerin, S. Singh, V. Kostoglodov, and J. Pacheco, 2000: The energy partitioning and the diffusive character of the seismic coda. *Bulletin of the Seismological Society of America*, **90 (3)**, 655–665.

Shearer, P. M., 1997: Improving local earthquake locations using the l1 norm and waveform cross correlation: Application to the whittier narrows, california, aftershock sequence. *Journal of Geophysical Research: Solid Earth*, **102 (B4)**, 8269–8283.

Shearer, P. M., 2009: *Introduction to seismology*. Cambridge University Press.

Shearer, P. M., and P. S. Earle, 2004: The global short-period wavefield modelled with a monte carlo seismic phonon method. *Geophysical Journal International*, **158 (3)**, 1103–1117.

Shearer, P. M., and P. S. Earle, 2008: Observing and modeling elastic scattering in the deep earth. *Advances in Geophysics*, **50**, 167–193.

Shearer, P. M., M. A. Hedlin, and P. S. Earle, 1998: Pkp and pkkp precursor observations: Implications for the small-scale structure of the deep mantle and core. *The Core-Mantle Boundary Region*, 37–55.

Shearer, P. M., G. A. Prieto, and E. Hauksson, 2006: Comprehensive analysis of earthquake source spectra in southern california. *Journal of Geophysical Research: Solid Earth*, **111 (B6)**.

Shen, Y., D. W. Forsyth, J. Conder, and L. M. Dorman, 1997: Investigation of microearthquake activity following an intraplate teleseismic swarm on the west flank of the southern east pacific rise. *Journal of Geophysical Research: Solid Earth*, **102 (B1)**, 459–475.

Shudde, R., and D. Barr, 1977: An analysis of earthquake frequency data. *Bulletin of the Seismological Society of America*, **67 (5)**, 1379–1386.

Singh, S., and R. B. Herrmann, 1983: Regionalization of crustal coda q in the continental united states. *Journal of Geophysical Research: Solid Earth*, **88 (B1)**, 527–538.

Steck, L. K., W. A. Prothero, and J. Scheimer, 1989: Site-dependent coda q at mono craters, california. *Bulletin of the Seismological Society of America*, **79 (5)**, 1559–1574.

Stein, R. S., 1999: The role of stress transfer in earthquake occurrence. *Nature*, **402 (6762)**, 605.

Su, F., and K. Aki, 1990: Temporal and spatial variation on coda q^{-1} associated with the north palm springs earthquake of july 8, 1986. *Pure and Applied Geophysics*, **133 (1)**, 23–52.

Su, F., and K. Aki, 1995: Site amplification factors in central and southern california determined from coda waves. *Bulletin of the Seismological Society of America*, **85 (2)**, 452–466.

Su, F., K. Aki, and N. Biswas, 1991: Discriminating quarry blasts from earthquakes using coda waves. *Bulletin of the Seismological Society of America*, **81 (1)**, 162–178.

Su, F., K. Aki, T. Teng, Y. Zeng, S. Koyanagi, and K. Mayeda, 1992: The relation between site amplification factor and surficial geology in central california. *Bulletin of the Seismological Society of America*, **82 (2)**, 580–602.

Sumiejski, L. E., and P. M. Shearer, 2012: Temporal stability of coda q^{-1} in southern california. *Bulletin of the Seismological Society of America*, **102 (2)**, 873–877.

Suteau, A. M., and J. H. Whitcomb, 1979: A local earthquake coda magnitude and its relation to duration, moment m_o, and local richter magnitude m_l. *Bulletin of the Seismological Society of America*, **69 (2)**, 353–368.

Takemura, S., T. Furumura, and T. Saito, 2009: Distortion of the apparent s-wave radiation pattern in the high-frequency wavefield: Tottori-ken seibu, japan, earthquake of 2000. *Geophysical Journal International*, **178 (2)**, 950–961.

Takemura, S., M. Kobayashi, and K. Yoshimoto, 2016: Prediction of maximum p-and s-wave amplitude distributions incorporating frequency-and distance-dependent characteristics of the observed apparent radiation patterns. *Earth, Planets and Space*, **68 (1)**, 166.

Takemura, S., M. Kobayashi, and K. Yoshimoto, 2017: High-frequency seismic wave propagation within the heterogeneous crust: effects of seismic scattering and intrinsic attenuation on ground motion modelling. *Geophysical Journal International*, **210 (3)**, 1806–1822.

Tanaka, S., 2010: Tidal triggering of earthquakes precursory to the recent sumatra megathrust earthquakes of 26 december 2004 (mw 9.0), 28 march 2005 (mw 8.6), and 12 september 2007 (mw 8.5). *Geophysical Research Letters*, **37 (2)**.

Tanaka, S., 2012: Tidal triggering of earthquakes prior to the 2011 tohoku-oki earthquake (mw 9.1). *Geophysical Research Letters*, **39 (7)**.

Tanaka, S., M. Ohtake, and H. Sato, 2002a: Evidence for tidal triggering of earthquakes as revealed from statistical analysis of global data. *Journal of Geophysical Research: Solid Earth (1978–2012)*, **107 (B10)**, ESE–1.

Tanaka, S., M. Ohtake, and H. Sato, 2002b: Spatio-temporal variation of the tidal triggering effect on earthquake occurrence associated with the 1982 south tonga earthquake of mw 7.5. *Geophysical Research Letters*, **29 (16)**, 3–1.

Tanaka, S., M. Ohtake, and H. Sato, 2004: Tidal triggering of earthquakes in japan related to the regional tectonic stress. *Earth Planets and Space*, **56 (5)**, 511–516.

Tanaka, S., H. Sato, S. Matsumura, and M. Ohtake, 2006: Tidal triggering of earthquakes in the subducting philippine sea plate beneath the locked zone of the plate interface in the tokai region, japan. *Tectonophysics*, **417 (1)**, 69–80.

Tape, C., Q. Liu, A. Maggi, and J. Tromp, 2010: Seismic tomography of the southern california crust based on spectral-element and adjoint methods. *Geophysical Journal International*, **180 (1)**, 433–462.

Thatcher, W., and T. C. Hanks, 1973: Source parameters of southern california earthquakes. *Journal of Geophysical Research*, **78 (35)**, 8547–8576.

Trugman, D. T., and P. M. Shearer, 2017: Application of an improved spectral decomposition method to examine earthquake source scaling in southern california. *Journal of Geophysical Research: Solid Earth*, **122 (4)**, 2890–2910.

Trugman, D. T., P. M. Shearer, A. A. Borsa, and Y. Fialko, 2016: A comparison of long-term changes in seismicity at the geysers, salton sea, and coso geothermal fields. *Journal of Geophysical Research: Solid Earth*, **121 (1)**, 225–247.

Tselentis, G.-A., 1997: Evidence for stability in coda q associated with the egion (central greece) earthquake of 15 june 1995. *Bulletin of the Seismological Society of America*, **87 (6)**, 1679–1684.

Tsujiura, M., 1978: Spectral analysis of the coda waves from local earthquakes. *Bulletin of the Earthquake Research Institute, University of Tokyo*, **53**, 1–48.

Tsukuda, T., 1988: Coda-q before and after the 1983 misasa earthquake of m 6.2, tottori prefecture, japan. *Pure and Applied Geophysics*, **128 (1)**, 261–279.

Tsuruoka, H., M. Ohtake, and H. Sato, 1995: Statistical test of the tidal triggering of earthquakes: contribution of the ocean tide loading effect. *Geophysical Journal International*, **122 (1)**, 183–194.

Tucker, B., J. King, D. Hatzfeld, and I. Nersesov, 1984: Observations of hard-rock site effects. *Bulletin of the Seismological Society of America*, **74 (1)**, 121–136.

Turner, J. A., 1998: Scattering and diffusion of seismic waves. *Bulletin of the Seismological Society of America*, **88 (1)**, 276–283.

Vernon, F., and U. S. Diego, 1982: Anza regional network. *Dataset/Seismic Network*, **10.7914/SN/AZ**.

Vidale, J. E., D. C. Agnew, M. J. Johnston, and D. H. Oppenheimer, 1998: Absence of earthquake correlation with earth tides: An indication of high preseismic fault stress rate. *Journal of Geophysical Research: Solid Earth (1978–2012)*, **103 (B10)**, 24 567–24 572.

Walter, A. W., and C. S. Weaver, 1980: Seismicity of the coso range, california. *Journal of Geophysical Research: Solid Earth*, **85 (B5)**, 2441–2458.

Wang, J., T. Teng, and K. Ma, 1989: Temporal variation of coda-q during hualien earthquake of 1986 in eastern taiwan. *Pure and Applied Geophysics*, **130 (4)**, 617–634.

Wang, W., and P. Shearer, 2015: No clear evidence for localized tidal periodicities in earthquakes in the central japan region. *Journal of Geophysical Research: Solid Earth*, **120 (9)**, 6317–6328.

Wang, W., and P. Shearer, 2017: Using direct and coda wave envelopes to resolve the scattering and intrinsic attenuation structure of southern california. *Journal of Geophysical Research: Solid Earth*, **122 (9)**, 7236–7251.

Wang, W., and P. Shearer, 2019: An improved method to determine coda-q, earthquake magnitude, and site amplification: Theory and application to southern california. *Journal of Geophysical Research: Solid Earth*, **124 (1)**, 578–598.

Wegler, U., 2004: Diffusion of seismic waves in a thick layer: Theory and application to vesuvius volcano. *Journal of Geophysical Research: Solid Earth*, **109 (B7)**.

Wennerberg, L., 1993: Multiple-scattering interpretations of coda-*q* measurements. *Bulletin of the Seismological Society of America*, **83 (1)**, 279–290.

Wilcock, W. S., 2009: Tidal triggering of earthquakes in the northeast pacific ocean. *Geophysical Journal International*, **179 (2)**, 1055–1070.

Woodgold, C., 1994: Coda q in the charlevoix, quebec, region: Lapse-time dependence and spatial and temporal comparisons. *Bulletin of the Seismological Society of America*, **84 (4)**, 1123–1131.

Wu, R.-S., 1985: Multiple scattering and energy transfer of seismic waves–separation of scattering effect from intrinsic attenuation i. theoretical modelling. *Geophysical Journal International*, **82 (1)**, 57–80.

Wu, R.-S., and K. Aki, 1988: Multiple scattering and energy transfer of seismic waves–separation of scattering effect from intrinsic attenuation ii. application of the theory to hindu kush region. *Pure and Applied Geophysics*, **128 (1-2)**, 49–80.

Yabe, S., A. S. Baltay, S. Ide, and G. C. Beroza, 2014: Seismic-wave attenuation determined from tectonic tremor in multiple subduction zones. *Bulletin of the Seismological Society of America*, **104 (4)**, 2043–2059.

Yabe, S., and S. Ide, 2014: Spatial distribution of seismic energy rate of tectonic tremors in subduction zones. *Journal of Geophysical Research: Solid Earth*, **119 (11)**, 8171–8185.

Yamamoto, M., and H. Sato, 2010: Multiple scattering and mode conversion revealed by an active seismic experiment at asama volcano, japan. *Journal of Geophysical Research: Solid Earth*, **115 (B7)**.

Yang, W., and Y. Ben-Zion, 2010: An algorithm for detecting clipped waveforms and suggested correction procedures. *Seismological Research Letters*, **81 (1)**, 53–62.

Yang, W., E. Hauksson, and P. M. Shearer, 2012: Computing a large refined catalog of focal mechanisms for southern california (1981–2010): Temporal stability of the style of faulting. *Bulletin of the Seismological Society of America*, **102 (3)**, 1179–1194.

Yomogida, K., K. Aki, and R. Benites, 1997: Coda q in two-layer random media. *Geophysical Journal International*, **128 (2)**, 425–433.

Yoshimoto, K., 2000: Monte carlo simulation of seismogram envelopes in scattering media. *Journal of Geophysical Research: Solid Earth*, **105 (B3)**, 6153–6161.

Yoshimoto, K., and A. Jin, 2008: Coda energy distribution and attenuation. *Advances in Geophysics*, **50**, 265–299.

Yoshimoto, K., H. Sato, and M. Ohtake, 1993: Frequency-dependent attenuation of p and s waves in the kanto area, japan, based on the coda-normalization method. *Geophysical Journal International*, **114 (1)**, 165–174.

Yoshimoto, K., S. Takemura, and M. Kobayashi, 2015: Application of scattering theory to p-wave amplitude fluctuations in the crust. *Earth, Planets and Space*, **67 (1)**, 199.

Yu, C., V. Vavryčuk, P. Adamová, and M. Bohnhoff, 2018: Moment tensors of induced microearthquakes in the geysers geothermal reservoir from broadband seismic recordings: Implications for faulting regime, stress tensor, and fluid pressure. *Journal of Geophysical Research: Solid Earth*, **123 (10)**, 8748–8766.

Yun, S., W. S. Lee, K. Lee, and M. H. Noh, 2007: Spatial distribution of coda q in south korea. *Bulletin of the Seismological Society of America*, **97 (3)**, 1012–1018.

Zeng, Y., 2017: Modeling of high-frequency seismic-wave scattering and propagation using radiative transfer theorymodeling of high-frequency seismic-wave scattering and propagation using radiative transfer theory. *Bulletin of the Seismological Society of America*, **107 (6)**, 2948–2962.

Zhang, Q., G. Lin, Z. Zhan, X. Chen, Y. Qin, and S. Wdowinski, 2017: Absence of remote earthquake triggering within the coso and salton sea geothermal production fields. *Geophysical Research Letters*, **44 (2)**, 726–733.

Zoback, M. D., and M. L. Zoback, 2002: State of stress in the earth's lithosphere. *International Handbook of Earthquake and Engineering Seismology, Part A*, 559–568.